UNIVERSITY OF CALIFORNIA

Los Angeles

Phi Meson Production in Au+Au Collisions at the Relativistic Heavy Ion Collider

A dissertation submitted in partial satisfaction

of the requirements for the degree

Doctor of Philosophy in Physics

by

Eugene Toyonari Yamamoto

2001

The dissertation of Eugene Toyonari Yamamoto is approved.

Nu Xu

An Yin

Huan Z. Huang, Committee Co-chair

Charles A. Whitten Jr., Committee Co-chair

University of California, Los Angeles

2001

To my family. . .

who—along with the love and support they provided—

made sure I finished what I started.

TABLE OF CONTENTS

LIST OF FIGURES

LIST OF TABLES

VITA

24 July, 1975	Born, Honolulu, Hawaii, USA.
1997	B.S. Applied Physics Columbia University New York, NY
1997 – 1998	Teaching Assistant Department of Physics University of California - Los Angeles
1998	M.S. Physics University of California - Los Angeles Los Angeles, CA
1998 – 2001	Graduate Research Assistant Intermediate Energy Group University of California - Los Angeles

PUBLICATIONS AND PRESENTATIONS

K.H. Ackermann *et al.*
Hardware Controls for the STAR Experiment at RHIC.
IEEE Trans. Nucl. Sci. **47**:210, 2000.

K.H. Ackermann *et al.*
The STAR Time Projection Chamber.
Nucl. Phys. **A661**:681, 2000.

K.H. Ackermann *et al.*
Elliptic Flow in Au+Au Collisions at $\sqrt{s_{NN}} = 130$ GeV.
Phys. Rev. Lett., **86**:402, 2001.

C. Adler *et al.*
Multiplicity distribution of negatively charged hadrons in Au+Au collisions at $\sqrt{s_{NN}} =$ 130 GeV .
Accepted by *Phys. Rev. Lett.* 16 July, 2001.

C. Adler *et al.*
Pion Interferometry of $\sqrt{s_{NN}} = 130$ GeV Au+Au Collisions at RHIC.
Accepted by *Phys. Rev. Lett.* 11 July, 2001.

C. Adler *et al.*
Midrapidity Antiproton-to-Proton Ratio in Au+Au Collisions at $\sqrt{s_{NN}} = 130$ GeV.
Phys. Rev. Lett. **86**:4778, 2001.

E. Yamamoto
Measuring Strangeness Production in Heavy Ion Collisions using the STAR TPC.
Proceedings of the Lake Louise Winter Institute, 2000.

E. Yamamoto
Performance of the STAR TPC using Au+Au Collisions at RHIC.
Proceedings of the American Physical Society, 2000.

ABSTRACT OF THE DISSERTATION

Phi Meson Production in Au+Au Collisions at the Relativistic Heavy Ion Collider

by

Eugene Toyonari Yamamoto

Doctor of Philosophy in Physics

University of California, Los Angeles, 2001

Professor Charles A. Whitten Jr., Co-chair

Professor Huan Z. Huang, Co-chair

Results from the first measurement of mid-rapidity ϕ vector meson production in $Au+Au$ collisions at RHIC ($\sqrt{s_{NN}} = 130$ GeV) are described. Using the STAR detector, ϕ mesons were measured from the $\phi \rightarrow K^+K^-$ decay channel. For the 11% most central collisions, the slope parameter from an exponential fit to the transverse mass distribution is $T = 379 \pm 51$ (stat) $\pm$ 45 (syst) MeV, the yield $dN/dy = 5.73 \pm 0.37$ (stat) $\pm$ 0.57 (syst) per event and the ratios N_ϕ/N_{h^-} and N_ϕ/N_{K^-} are found to be 0.021 $\pm$ 0.001 (stat) $\pm$ 0.004 (syst) and 0.14 $\pm$ 0.01 (stat) $\pm$ 0.03 (syst). Within the statistics available, the mid-rapidity ratios, N_ϕ/N_{h^-} and N_ϕ/N_{K^-}, and the slope parameter for the ϕ meson do not change for the selected centrality bins. The slope parameter increases in heavy ion collisions as a function of $\sqrt{s_{NN}}$ from the BNL AGS to CERN SPS to RHIC. Comparisons of the ϕ meson slope parameter to the slope parameters for the π, K, and $\bar{p}$ measured at STAR indicate that the ϕ meson deviates from a systematic trend of a mass dependence of the slope parameter, suggesting that the ϕ meson may not interact as strongly as anti-protons during a collective expansion of the collision system. The production of ϕ mesons relative to negatively charged hadrons (N_ϕ/N_{h^-})

in nucleus-nucleus collisions indicates an overall increase in strange and anti-strange quark production from $\sqrt{s_{NN}} = 4.9$ GeV to $\sqrt{s_{NN}} = 130$ GeV. When comparing the N_ϕ/N_{K^-} ratio in $p+p$, $p+\bar{p}$, $Pb+Pb$ and $Au+Au$ collisions, we find that the ratio is independent of both system size and energy from the AGS to the Tevatron. This result suggests some universal relationship between the mechanisms responsible for ϕ and K^- meson production.

CHAPTER 1

Introduction

The motivation for studying relativistic heavy ion collisions is to understand the *Equation of State* of nuclear matter. The goal of relativistic heavy ion physics is to understand Quantum Chromodynamics (QCD) at extreme temperatures and energy over large volumes and to create a Quark-Gluon Plasma (QGP) [BGS98, Wil00a, Wil00b] (Figure 1.1). Under such extraordinary conditions, it is believed that the symmetries of QCD will reveal themselves: color will be deconfined and chiral symmetry will be restored. The environment created by heavy ion collisions is currently the only means in the laboratory to study QCD in the macroscopic limit and to observe a possible phase transition.

As with all non-Abelian gauge theories [PS95], QCD exhibits asymptotic freedom: the strong coupling constant, α_s, becomes small at large momentum transfers and short distances. According to Lattice QCD, when the vacuum temperature exceeds $\sim$150 MeV, the structured QCD vacuum melts, hadrons dissociate and fuse, and a macroscopic space-time region is formed, filled with quarks and gluons which cannot be associated with individual hadrons. This region of dissociated quarks and gluons is commonly referred to as the Quark-Gluon Plasma. A QGP is believed to have existed in the early universe about one micro-second after the Big Bang. After that, the couplings between quarks and gluons favored the formation of color neutral bound states, and the universe transitioned to hadronic matter.

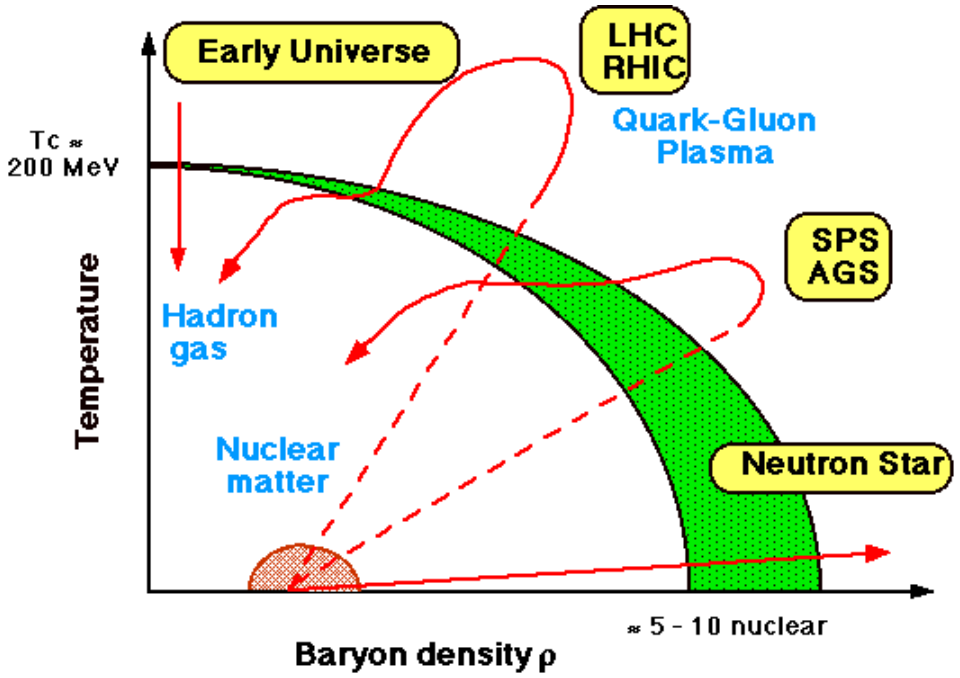

Figure 1.1: QCD phase diagram. The major features of the QCD phases possibly accessible in nature and heavy ion collisions are shown.

Since the mid 1980's, scientists have studied heavy ion collisions with the hope of observing deconfinement and chiral symmetry restoration. Results from the Alternating Gradient Synchrotron (AGS) at Brookhaven and the CERN SPS proved that a direct observation of the predicted QCD transition through the haze created by hadronic interactions is difficult. The final products at AGS energies proved to be dominated by final state hadronic interactions, with similar dynamics at the SPS.

Scientists working at Brookhaven National Laboratories are currently studying heavy ion collisions using the Relativistic Heavy Ion Collider (RHIC). With center of mass collision energies that are 10 times greater than the previous energies studied in heavy ion collisions, we may finally observe the predicted QCD phase transition. RHIC, and its associated experiments, including the Solenoidal Tracker at RHIC (STAR), offer the opportunity to study QCD in a controlled environment. With RHIC we can systematically measure the macroscopic properties of strongly interacting mat-

ter and the predicted transition back to normal matter. RHIC, with its nucleus-nucleus collisions at unprecedented high energy density and temperature, will provide a unique opportunity to better understand non-perturbative QCD and the conditions prevalent in the early universe.

CHAPTER 2

Physics

2.1 QCD

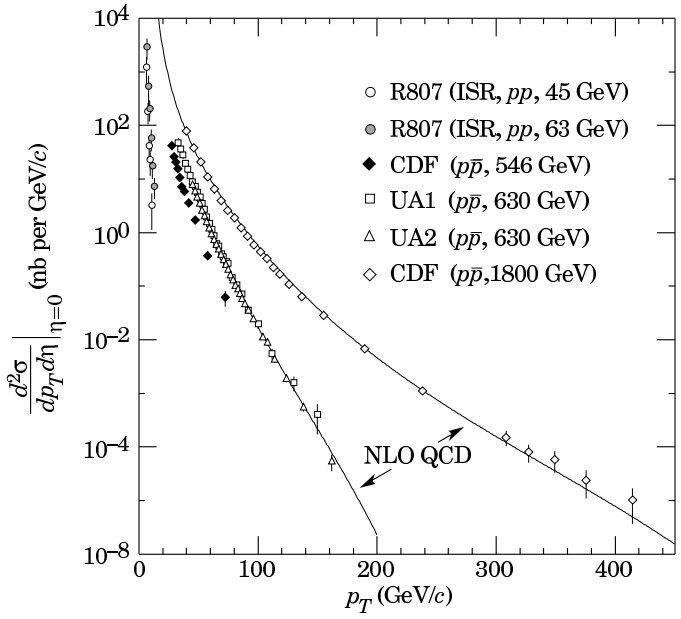

Figure 2.1: Differential cross sections for the observation of a single jet of pseudo-rapidity $\eta = 0$ as a function of the transverse momentum of the jet. The lines through the data are next-to-leading order (NLO) QCD curves for 630 GeV and 1800 GeV $p + \bar{p}$ collisions. Figure taken from the Particle Data Book [GG00].

In some ways, QCD is a mature, well established subject. Its principles are precisely defined and have been extensively confirmed by experiment (Figure 2.1). QCD specifies unambiguous algorithms that supply answers to any physically meaningful question within its realm, namely the strong interaction. The foundations of QCD are

rooted in concepts of symmetry and local quantum field theory, which lead uniquely to its equations. One cannot revise the equations without undermining these concepts.

QCD is enigmatic: while the equations of QCD are relatively simple and mathematically sound, they seem at first to have nothing to do with reality. QCD refers exclusively to particles (quarks and gluons) that are not directly observed. More profoundly, the equations of QCD exhibit a host of symmetries that are not apparent in our world. It has been found that these various symmetries are hidden: color is confined, scale invariance and axial baryon number are anomalous, and chiral symmetry is broken. It is bewitching how a theory that superficially appears too good for this world actually describes it accurately. *Vis-a-vis*, it is aesthetically pleasing to realize that the world is simpler and more beautiful than it first appears.

To say that QCD describes reality well is a gross understatement. QCD describes processes extremely well, so much so that people have calculated QCD corrections to other processes. Mature, however, does not necessarily mean dead. The peculiarities of QCD, namely that its fundamental entities and symmetries are well hidden in ordinary matter, lends itself to the discussion of its behavior in extreme conditions. Quarks, gluons, and the various symmetries of QCD will, in the right circumstances, reveal themselves.

The behavior of QCD at high temperatures is intrinsically interesting. The fundamental theoretical result of the asymptotically high temperature QCD phase is that it becomes quasi-free: one can now describe the major features of this phase by modeling it as a plasma of weakly interacting quarks and gluons. By answering the question, “What happens to empty space if we add more and more heat?”, we will have an understanding of the earliest moments after the Big Bang, when the matter content of the universe was most likely dominated by a quark-gluon plasma.

2.2 Strangeness Production

The production of strange (s) and anti-strange ($\bar{s}$) quarks was proposed by Rafelski [Raf82] as a probe to study the QCD phase transition.

$$\pi + N \rightarrow \Lambda + K \qquad E_{threshold} \simeq 530 \text{ MeV} \tag{2.1}$$

Hadronic scenarios for strangeness production involve relatively high energy thresholds (Equation 2.1). A significant enhancement of strangeness production is predicted if a phase transition to a QGP occurs. Since the temperature at which the QCD transition occurs is very close to the strange quark current mass of 150 MeV, $s\bar{s}$ pairs could form copiously through gluon fusion (Equation 2.2) [BGS98] in a gluon rich QGP state.

$$g + g \rightarrow s + \bar{s} \qquad E_{threshold} \simeq 2m_s \simeq 300 \text{ MeV} \tag{2.2}$$

If we compare the threshold energy for strangeness production in a QGP via gluon fusion (Equation 2.2) to the threshold energy in a hadronic scenario (Equation 2.1), we would expect to see more $s\bar{s}$ pairs produced in a QGP. Quantitative theoretical calculations by Koch, Müller and Rafelski [Raf82, KMR86] support the conclusion of strangeness enhancement in a QGP when compared to a hadronic scenario.

Experimental evidence from both the BNL AGS and CERN SPS accelerators have reported large increases in relative strange particle yields when compared to non-strange hadrons in central light (*Si*, *S*) [Abb90, Ahl99, Alb94, Ant99], and heavy ion (*Au*, *Pb*) [Ahl98, Ahm96, And99, Bor97, Mar99] collisions when compared to $p+p$ collisions. We nevertheless cannot claim a true understanding of the physics of strangeness enhancement due to the complexity of hadronic interactions in $A+A$ collisions. The difficulty of interpreting the enhancement in $A+A$ data has prompted

the use of $p+A$ collisions to study this problem further.

The simpler final state in $p+A$ collisions allows the production rate for strange particles to be directly connected with the scattering dynamics of the incoming proton. Recent results from $p+A$ collisions at the AGS have shown that strange baryon production is enhanced when compared to $p+p$ collisions. The E910 experiment [Che00] has studied strangeness enhancement in $p+A$ collisions as a function of centrality, where centrality in $p+A$ collisions is correlated to the number of "grey" tracks from a collision. Their results suggest that an increase in strangeness production is present over a simple number of participants (N_{part}) scaling of $p+p$ data. The qualitative implications for using a simple N_{part} scaling are clear: to establish an anomalous strangeness enhancement in $A+A$ collisions that may be attributed to the formation of a deconfined state of quarks and gluons, one must include the effects of multiple collisions of the projectile traversing the target nucleus. Furthermore, a simple N_{part} scaling to the $A+A$ data is insufficient to firmly establish the formation of a new state of matter. A detailed study of both $p+p$ and $p+A$ collisions at RHIC energies will be necessary.

2.3 The ϕ Meson

The ϕ meson is the lightest vector meson with hidden strangeness ($s\bar{s}$). The major properties of the ϕ meson are listed in Table 2.1. In e^+e^- and nucleon-nucleon collisions, ϕ meson production is believed to proceed mainly via a color singlet gluon configuration. The production of ϕ mesons through light quark pair annihilation is suppressed by the OZI rule [Oku63, Iiz66]. The origin of the suppression is believed to lie in the non-abelian nature of QCD. Since the ϕ is produced by gluons, the gluons must carry enough energy to create the ϕ resonance state. The gluons therefore have

higher momenta and the coupling constant, α_s, is smaller.

ϕ Meson	
Mass	1019.417 MeV/c^2
Γ (FWHM)	4.458 MeV/c^2
Branching Ratios	
K^+K^-	49.1%
e^+e^-	0.0291%
$\mu^+\mu^-$	0.037%

Table 2.1: Properties of the ϕ vector meson.

2.3.1 ϕ Meson Production in Heavy Ion Collisions

It has been postulated that in heavy ion collisions, several mechanisms for ϕ meson production are available. The canonical ϕ meson production mechanisms are $ggg \rightarrow \phi$ and $q\bar{q} \rightarrow \phi$. There is also the possibility of producing ϕ mesons via the reverse reaction of the phi decay, namely $K + \bar{K} \rightarrow \phi$.

Baltz and Dover [BD96] proposed that in heavy ion collisions where the final state phase space density of K and $\bar{K}$ is much higher than in simple colliding systems ($p+p$ and $p+\bar{p}$), ϕ meson production may proceed by the coalescence of hadronic state kaons (Equation 2.3) to form an $s\bar{s}$ bound state. Although their analysis of ϕ meson production was specific to $Si+Au$ collisions at the AGS (E802 and E859), the concepts are based on general phase space density arguments and are applicable to all heavy ion systems. This mechanism seems viable because it proceeds by the exchange of soft gluons.

$$K + \bar{K} \rightarrow \phi \tag{2.3}$$

If, however, one considers that kaons are spin zero particles while the ϕ has spin one, it now becomes apparent that the kaon coalescence model, although favorable when considering the magnitude of α_s, suffers a penalty due to the constraints imposed by

the spin quantum number.

There is also the tantalizing mechanism mentioned in Section 2.2, namely $gg \rightarrow s\bar{s}$. Shor [Sho85] and Sorge [BSG94] proposed an enhancement of ϕ meson production as a direct measurement of QGP formation. Their proposals make two assumptions: the production of ϕ mesons from a hadronic gas is OZI suppressed, whereas the sheer abundance of $s\bar{s}$ pairs in a QGP will enhance the ϕ yield during the hadronization of a QGP. In his paper, Shor claims the variation of the ratio $\phi/(\rho+\omega)$ with baryon density or energy density as a measurement of QGP formation that is experimentally feasible. Unfortunately, the measurements of the ρ and ω are extremely difficult and will not be available from the year one data.

Extracted slope parameters (T) from an exponential fit to the invariant multiplicity distribution may yield information on the dynamical evolution of the heavy ion collision. A deviation of T from the mass systematics attributed to radial flow could elucidate the production mechanism for the ϕ meson as well as the dynamical properties of the ϕ meson's interaction with other particles.

Sorge, *et al.* made a striking prediction using RQMD [Sor92, BSG94]. By implementing a string fusion mechanism, they predicted that the production of ϕ's would be enhanced while the kaon production would remain unaffected.

While the K/π ratio gives an overall indication of the strangeness content in the final state of the collision, the ϕ/π ratio, because of the $s\bar{s}$ content of the ϕ meson, may provide a more sensitive measure of the strangeness production in heavy ion collisions. One would naïvely expect that while kaon production is proportional to the phase space density of strange quarks, γ_s, the dependence of the ϕ meson should scale with γ_s^2. There is currently no clear description of s and $\bar{s}$ hadronization.

Experimentally, the ϕ to K^- ratio is the most promising: K^-'s are produced only via pair production, very few resonances decay into kaons when compared to pions,

and the analysis is possible with the data in hand. A comparison of the ϕ/K^- ratio as a function of $\sqrt{s_{NN}}$ and collision system ($p+p$, $p+\bar{p}$, $A+A$) could provide an insight to the production mechanisms for the ϕ meson in heavy ion collisions. If the ϕ/K^- ratio differs as a function of $\sqrt{s_{NN}}$ and/or system size, this may indicate that dynamical processes such as kaon coalescence play a significant role in ϕ meson production. On the other hand, if the ratio is independent of both collision energy and system size, this will put a severe constraint on the production mechanisms responsible for ϕ meson production. At the very least, a similar ϕ/K^- ratio for all energies and system sizes would indicate that the probability for strange quark hadronization into a ϕ meson or K^- meson is a universal property. One may then study the possible production mechanisms for the ϕ meson in simpler systems and possibly make a statement on the actual production process: whether this be $ggg \rightarrow \phi$, $s+\bar{s} \rightarrow \phi$ or $K+\bar{K} \rightarrow \phi$.

2.3.2 Understanding the Production Properties of the ϕ Meson

Recent results from STAR [Adl01a] show that unlike the AGS and SPS where the stopping of projectile nucleons contributed significantly to the initial conditions of the heavy ion collision, anti-baryon and baryon pair production becomes more important. Results of the mid-rapidity anti-baryon to baryon ($\bar{B}/B$) ratio show that as a function of $\sqrt{s_{NN}}$ (Figure 2.2), this ratio is approaching unity in the central rapidity region for the most central heavy ion collisions through the year 2000 RHIC energy ($\sqrt{s_{NN}} = 130$ GeV).

The production properties of the ϕ meson in this environment, when compared to different colliding systems and system energies from $Au+Au$ collisions at the AGS to $p+\bar{p}$ collisions at the Tevatron will be addressed. Of interest is the central rapidity region at RHIC which is most likely dominated by the dynamics of gluons. A comparison of the production properties of the ϕ meson in different collision environments

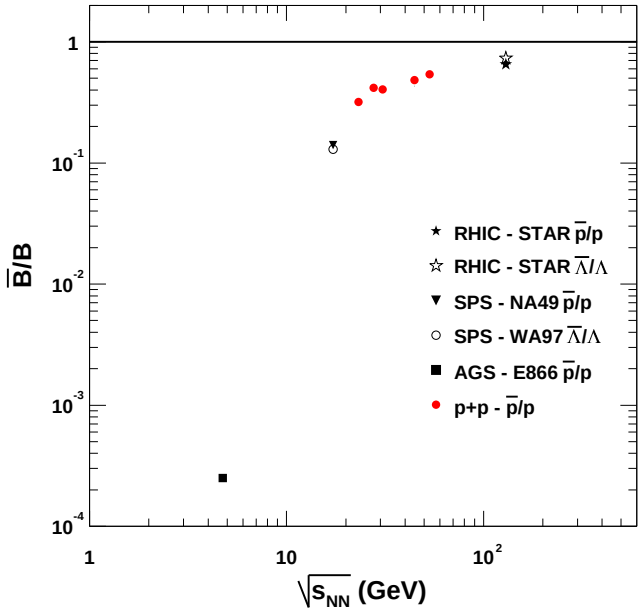

Figure 2.2: Anti-baryon to baryon ratio vs. $\sqrt{s_{NN}}$. Heavy ion data for $\bar{\Lambda}/\Lambda$ and $\bar{p}/p$ are shown as well as the $\bar{p}/p$ ratio from $p+p$ collisions. There is considerable stopping in heavy ion collisions at the AGS and SPS ($\sqrt{s_{NN}} = 4.9$ and 17.2 GeV, respectively). Year 2000 RHIC data at $\sqrt{s_{NN}} = 130$ GeV indicates that $B-\bar{B}$ pair production accounts for over half of the baryon number in the central rapidity region.

may elucidate the dominant production mechanism for the ϕ meson and its interaction with other particles. In particular, if one observes significant differences in the particle ratio ϕ/K^- between the AGS where the net baryon number is high and RHIC where the net baryon number is low and pair production is the dominant mechanism (at least for baryons and anti-baryons, presumably for quarks and anti-quarks), one may deduce from this difference that mesons carrying strange quarks are sensitive to the initial conditions of the colliding system. Comparisons of the heavy ion data to $p+p$ collisions will also shed light on this matter. On the other hand, the lack of a significant dependence of the ϕ/K^- ratio on collision energy and system size would indicate that the probability of anti-strange quark hadronization into either a ϕ or K^- meson is universal.

2.3.3 Dynamical Properties of the ϕ Meson

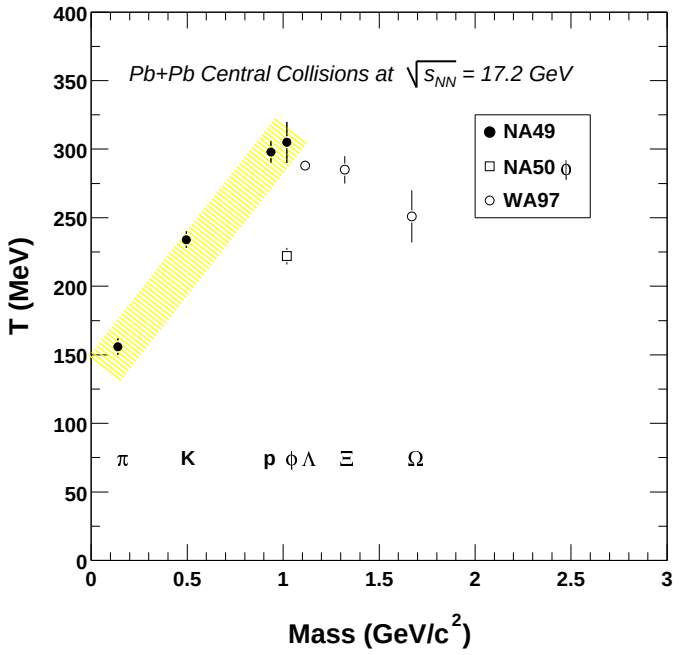

Figure 2.3: Slope parameters from an exponential fit to the transverse mass distribution vs. the mass of the particle from the most central $Pb+Pb$ collisions at the CERN SPS. Pions, kaons and protons seem to follow an increasing linear trend with their mass. For baryons with strange quarks, there is a deviation from this straight line. Note that there are two measurements for the ϕ meson ($\phi \rightarrow K^+K^-$ from NA49 and $\phi \rightarrow \mu^+\mu^-$ from NA50). Error bars shown are statistical errors only.

Equation 2.4 shows the expected relation between the measured slope parameter from an exponential fit to the invariant transverse mass (m_t) distribution, T, the thermal freeze out temperature, T_0, and the common expansion velocity, β [Bea97]. This equation is approximately valid under the assumption that all particles approach the hydrodynamical limit because of large cross-sections. Section 8.2 contains a brief discussion on the origins of Equation 2.4. Any deviation from this linear trend with mass may be indicative of a quantitative difference in the dynamical evolution of these particles.

$$\langle T \rangle = T_0 + m\beta^2 \tag{2.4}$$

In central $Pb+Pb$ collisions at the SPS (nucleon-nucleon center of mass energy $\sqrt{s_{NN}} = 17.2$ GeV), the slope parameter (T) in an exponential fit to the transverse mass (m_t) distribution at mid-rapidity ($\propto e^{-m_t/T}$) follows a systematic trend as a function of hadron mass for pions, kaons and protons [Bea97] (Figure 2.3). This observation is interpreted as resulting from a common expansion velocity developed in the final state for pions, kaons, and protons [Hei96]. The slope parameters measured for the multi-strange hyperons Ξ and Ω [Lie99], however, show deviations from a linear mass dependence, suggesting that these particles do not interact as strongly in the final state at SPS energies [HSX98]. Measurements of ϕ meson production at the SPS were inconclusive [Afa00, Wil99].

NA49 measurements of the ϕ meson slope parameter from the K^+K^- decay channel seemed to indicate that in central $Pb+Pb$ collisions, the ϕ meson fits into the model of collective radial expansion of the system. However, NA50 results from the $\mu^+\mu^-$ decay channel showed the ϕ meson slope parameter is significantly lower, a result which in the radial expansion model suggests the ϕ meson does not interact strongly in the final state radial expansion. The difference between the NA49 and NA50 measurements disappears for peripheral collisions. It has been hypothesized that in central heavy ion collisions, rescatterings of the kaons from ϕ decays in the fireball may change the measured ϕ slope parameter [JJD01, Sof01]. This effect, however, can only account for 10 to 20% of the difference in the two measurements. If there is a significant modification of the spectral shape due to radial expansion, there will be a strong p_t dependence of the measured slope parameter (see Section 8.2).

CHAPTER 3

Facilities

3.1 RHIC Accelerator Complex

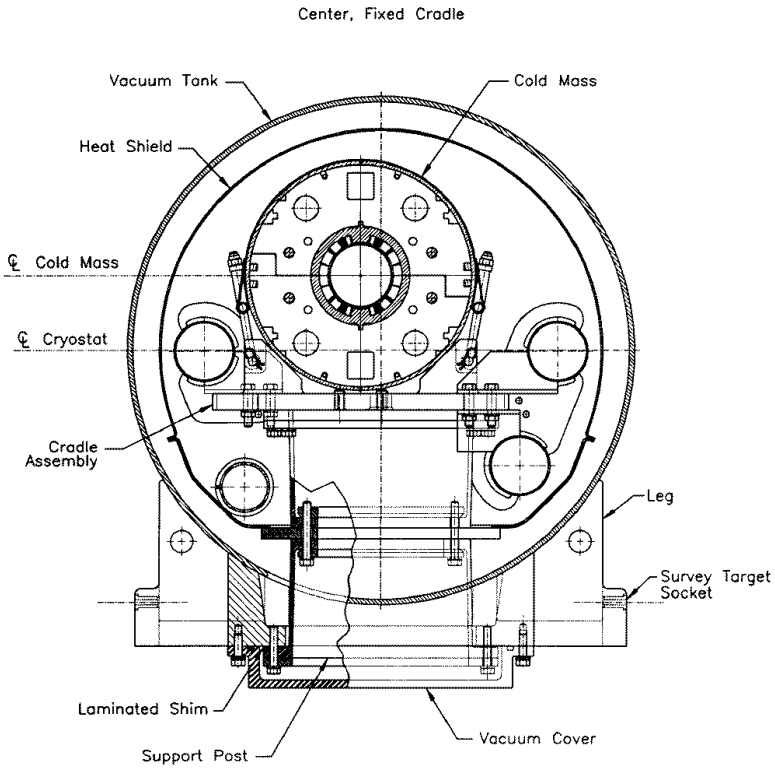

Figure 3.1: Cross section of an arc dipole. The outer diameter of the vacuum vessel is 610 millimeters.

The RHIC facility consists of two rings of superconducting magnets, each with a circumference of 2.4 miles. The main components of the magnet system are 288 arc dipoles (Figure 3.1), 108 insertion dipoles, and 276 arc and 216 insertion quadrupoles.

In addition to the dipoles and quadrupoles, an inventory of 72 trim quadrupoles, 288 sextupoles, and 492 corrector magnets exists. The arc dipoles have a physical length of 9.728 m (9.45 m effective), are bent with a 4.85 cm sagitta and have a coil aperture of 8 cm in order to accommodate intra-beam scattering. The beam tubes in the magnets are at liquid helium temperatures, with the beams in the arcs separated by 90 cm. The magnets are cooled to a temperature of < 4.6 K by circulating super-critical helium supplied by 24.8 kW refrigerators. Extremely good vacuums of $< 10^{-11}$ mbar in the cold bore and $\sim 7 \times 10^{-10}$ mbar in the warm beam tube sections is achieved at RHIC to minimize beam losses and radiation background.

Physical Parameters		
No. Intersection Regions	6	
No. Bunches/ring	60	
Bunch Spacing (nsec)	213	
Collision Angle	0	
Free Space at Crossing Point (m)	± 9	
Performance Specifications	*Au*	*p*
No. Particles/Bunch	1×10^9	1×10^{11}
Top Energy (Gev/u)	100	250
Luminosity, average ($cm^{-2}sec^{-1}$)	$\sim 2 \times 10^{26}$	$\sim 1 \times 10^{31}$

Table 3.1: Physical parameters and performance specifications for the Relativistic Heavy Ion Collider (RHIC).

RHIC is the first collider to accelerate heavy ion beams and is capable of accelerating any combination of species from $p+p$ @ $\sqrt{s} = 500$ GeV up to $Au+Au$ @ $\sqrt{s} = 40$ TeV. This unprecedented flexibility allows the study of colliding systems as a function of both energy and system size, a capability unique to this facility. RHIC is designed for a $Au+Au$ luminosity of about $2 \times 10^{26} cm^{-2} sec^{-1}$ at top energy, while maintaining the potential for future upgrades by an order of magnitude. The luminosity for lighter ions will be higher, with $p+p$ collisions at $\mathcal{L} = 1 \times 10^{31} cm^{-2} sec^{-1}$. Table 3.1 lists the performance specifications for RHIC.

The collider's performance is achieved in different ways. An important choice in the RHIC design was the utilization of short bunches colliding head-on to enhance the luminosity while keeping the average current and stored beam energy low. Formation of the bunches occurs prior to injection, using the previously existing accelerator complex at BNL.

The complex required to produce, accelerate and store the heavy ion beam consists of the Tandem Van de Graaff accelerators, the Booster Synchrotron and the Alternating Gradient Synchrotron (AGS), which combine to serve as the injector for RHIC (Figure 3.2). Gold (*Au*) atoms with a charge -1 are generated in the Pulsed Sputter Ion Source in the Tandem Van de Graaff facility, accelerated and passed through two *Au* foils, leaving the *Au* atoms with a net +32 charge. The 1 MeV/nucleon *Au* beam is transferred to the booster where it is accelerated to 95 MeV/nucleon and then stripped further to a net +77 charge. In the AGS, the *Au* beam is bunched and further accelerated to 10.8 GeV/nucleon and is extracted using fast extraction. Fast Extracted Beam (FEB) attempts to extract a significant portion of many AGS *Au* bunches into one RHIC bunch. The FEB bunches are then delivered to RHIC through the AGS To RHIC (ATR) transfer line. In this final stage before injection into the RHIC ring, the *Au* nuclei are completely stripped of orbital electrons and have a charge of +79. Once injected into RHIC, the bunches are accelerated to collision energy and stored for data taking.

To accelerate, capture and store the beam, RHIC employs a radio frequency (*rf*) system [Pro94]. The varying requirements imposed on the *rf* are satisfied by three systems.

- An acceleration system (26 MHz) for capture of the injected beam, acceleration to top energy, and bunch shortening at top energy.
- A storage system (196 MHz) for sufficient longitudinal focusing to keep bunches

short during the 10 hour storage time.

- A longitudinal kicker to damp longitudinal injection errors of individual bunches and for damping longitudinally coupled bunch instabilities.

Table 3.2 lists the major characteristics of these systems.

Systems	Accelerating	Storage	Kicker
Harmonic	342	2508	
Radio frequency (MHz)	26.743	196.12	wide band
Stations	4	10	2
Stations/ring	2	$3+4$	1
Voltage/station (kV)	300	1000	1
Voltage/ring (kV)	2×300	7×1000	1×1

Table 3.2: RHIC *rf* cavity systems and longitudinal kicker.

3.1.1 RHIC 2000 Commissioning

RHIC has six interaction regions, with 4 regions currently occupied. Two small experiments, BRAHMS and PHOBOS, and two large experimental programs, PHENIX and STAR, have successfully taken data during the summer 2000 RHIC run.

Progress at RHIC was made in fits and starts, with RHIC operations beginning slowly. The operators were just beginning to understand the characteristics of the accelerator and very little progress was initially made. But on the night of 11 June 2000, STAR recorded the first beam-beam collision at the injection energy of $\sqrt{s_{NN}} =$ 20 GeV. At 9 PM on 12 June 2000, STAR recorded the first ever beam-beam collision event at RHIC at a collision energy of $\sqrt{s_{NN}} = 60$ GeV (Figure 3.3). The collisions at $\sqrt{s_{NN}} = 60$ GeV were a major milestone for RHIC because they proved that RHIC could accelerate and collide beams of heavy ions. Just a few short weeks after that, collisions at $\sqrt{s_{NN}} = 130$ GeV (Figure 3.4), our nominal beam energy for the summer, were recorded by STAR.

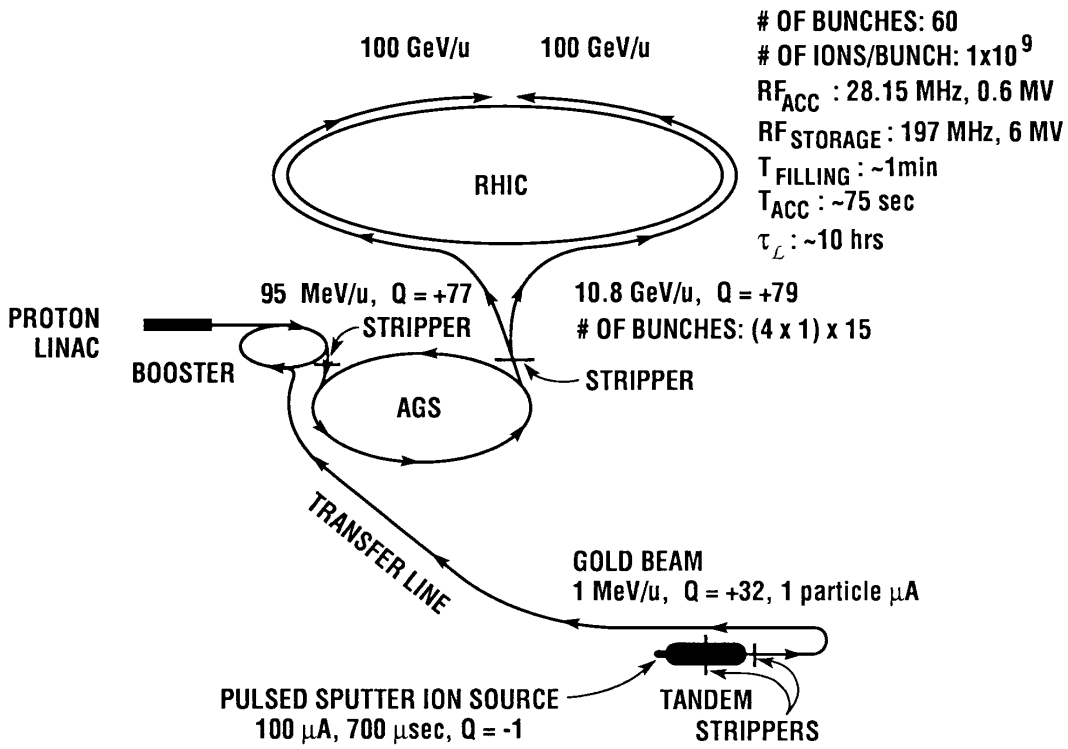

Figure 3.2: Diagram of the AGS - RHIC facility. The heavy ion beam is produced at the Pulsed Sputter Ion Source, accelerated through the Tandem Van de Graaff, booster and AGS, fast extracted at 10.8 GeV/nucleon and injected into RHIC where the beam is accelerated to a top energy of 100 GeV/nucleon and stored. Protons do not proceed through the Tandem Van de Graaff but are accelerated through the LINAC and then to the booster, AGS, and injected into RHIC.

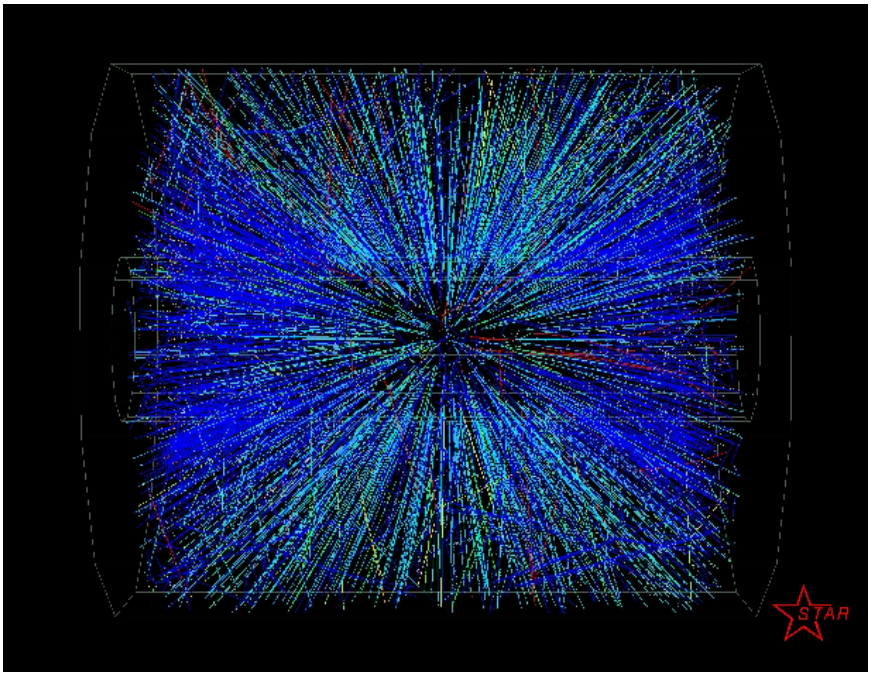

Figure 3.3: First collision at $\sqrt{s_{NN}} = 60$ GeV.

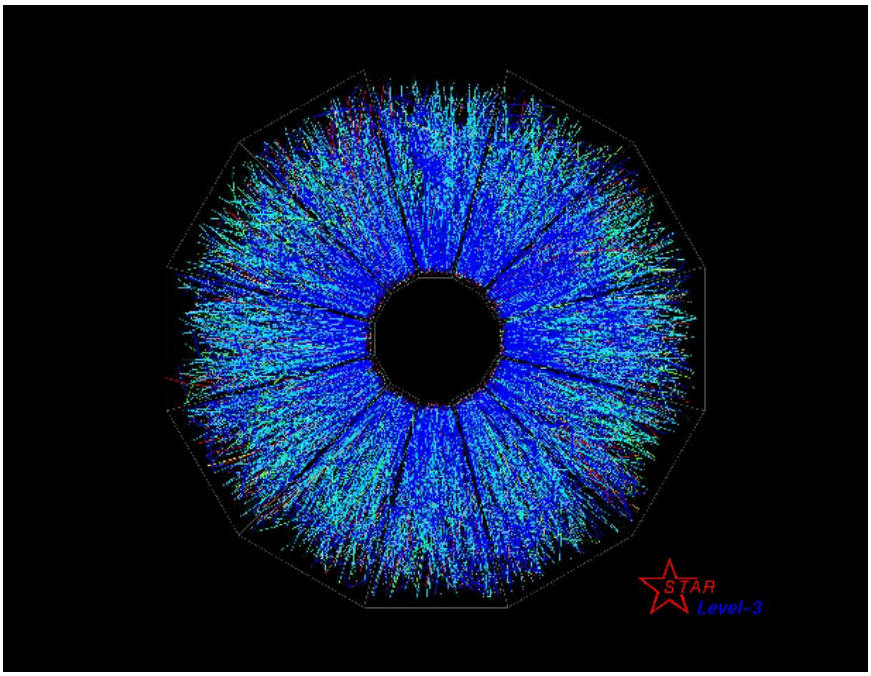

Figure 3.4: First collision at $\sqrt{s_{NN}} = 130$ GeV.

3.1.2 Summer 2000 Operations

Overall, RHIC performed well during the first year of running. Sufficient luminosity was delivered in the last month of operations, with the luminosity achieved being about 10% of the design luminosity. The first year's dataset showed that there are issues remaining that need to be addressed.

Since the storage *rf* cavities were not in use, the bunches in the ring were relatively long, resulting in a wide distribution for the primary vertex position along the beam axis. The design goal is for an interaction region with a width of 20 cm. During the summer run, we measured a gaussian sigma for the primary vertex position in Z between 70 and 100 cm. This is cause for some concern since our detector acceptance depends on the location of the collision. Another complication is with the material in the beam pipe. There is a 150 cm section of beryllium (*Be*) beam pipe centered about the midpoint of each interaction region. *Be* is used instead of steel or aluminum because the radiation length is an order of magnitude less then these more commonly used pipe materials, resulting in fewer multiple scatterings and secondary particle production at the beam pipe. Unfortunately, with a sigma of 70 cm for the primary vertex position, at least 30 percent of our events will have particles traversing the high interaction length material. The storage *rf* system will also help with beam losses into adjacent *rf* buckets. This type of loss not only reduces our luminosity, but also increases the rate of beam-gas interactions.

STAR measured significant background rates from beam interactions with residual gas molecules within the beam pipe. As previously mentioned in Section 3.1, there is an order of magnitude difference in vacuum pressure between the cold bore sections of the beam pipe and the warm beam pipe sections. Near each interaction region in RHIC, there are straight sections of beam pipe which are not actively cooled. Within these warm bore sections, beam gas events are more likely to occur than in the cold

bore sections. Since these straight sections are in the line of sight of the detector, we tend to see a high rate of these background events. Compounding this situation was the decision by RHIC operators to forego baking of the straight sections of the beam line, which resulted in out-gassing of the beam pipe over the course of the RHIC run. This is expected to be resolved for the year 2001 running when the full RHIC design luminosity will be achieved.

3.2 The STAR Detector

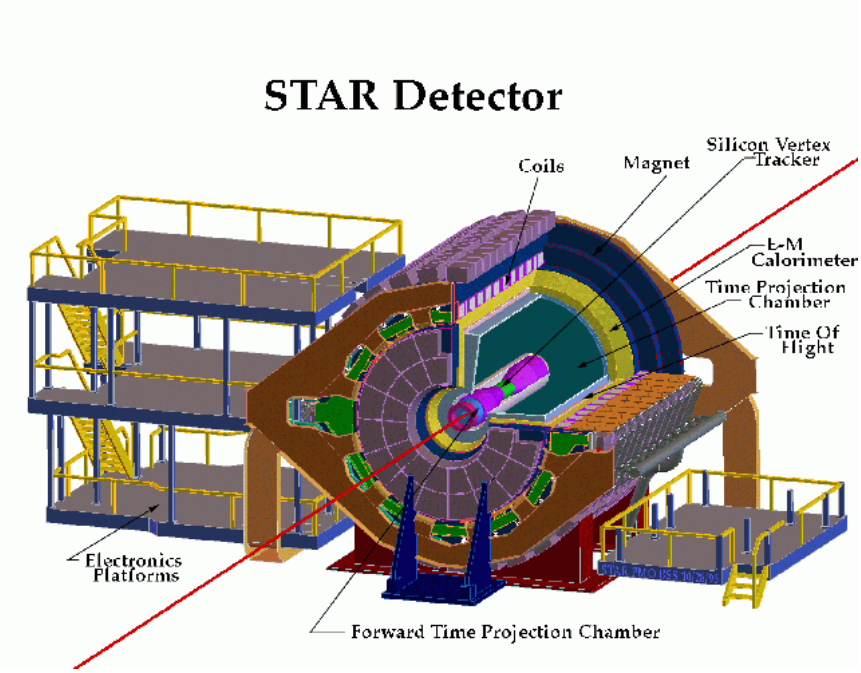

Figure 3.5: The STAR experiment.

STAR (Figure 3.5) is a large acceptance cylindrical geometry detector system with complete azimuthal coverage over the central rapidity region. The entire detector system is located within a 0.5 Tesla solenoidal analyzing magnet. STAR consists of several detectors centered around the main tracking chamber, the Time Projection Cham-

ber (TPC) [Ack99], which covers the pseudo-rapidity (η) region -2 $< \eta <$ 2. The TPC allows both momentum and particle identification information to be gathered, the latter accomplished by measuring the energy loss of a particle through the TPC's gas volume. Along with the TPC there is the Forward TPC, which extends the coverage in η, and the Silicon Vertex Tracker (SVT) [Pan99], which helps in reconstructing secondary vertices of neutral particles decaying to charged particles away from the primary vertex. There is also a full barrel electromagnetic calorimeter and end-cap calorimeter which provide complete coverage for photons and electrons. The lowest level trigger system is composed of a plastic scintillator trigger barrel (CTB), and two Zero Degree Calorimeters (ZDC). The CTB array is configured as a cylindrical barrel and surrounds the TPC. The ZDC's are located 18 meters up and downstream along the beam direction and measure beam-like neutrons from the fragmentation of colliding nuclei. The design of the ZDC's is the same for all RHIC experiments, allowing for a meaningful comparison of event centrality among the RHIC experiments.

For the year 2000 data taking, the experimental setup consisted of the TPC, CTB, and ZDC. There was also one ladder of prototype silicon detector from the SVT and a small acceptance ring imaging Cherenkov detector in place.

Hadronic Observables	
a) Charged hadrons:	p, $\bar{p}$, π's, K's, Ξ^-, $\bar{\Xi}^+$, Ω^-, $\bar{\Omega}^+$, d, $\bar{d}$
b) Neutral hadrons:	Λ, $\bar{\Lambda}$, K^0_s, ϕ, ρ, K^*, $\bar{K}^*$
c) Spectra:	p_t, particle ratios, slope parameters
d) Collision Geometry:	Flow, HBT, E-by-E correlations, Event Multiplicity
Electromagnetic Observables	
e) π_0, η distributions	
f) High p_t particles and jets	

Table 3.3: Quantities measurable on an Event-By-Event basis.

STAR offers excellent capabilities to study hadronic observables using the TPC, FTPC, and the silicon detectors, and good photon and electron coverage using the

TPC and the EM calorimeter. Because of STAR's large acceptance, it is possible to measure the quantities listed in Table 3.3 on an Event-by-Event basis with reasonable statistics. For the first year, STAR has detected all quantities listed in Table 3.3 a), b), c) and d), as well as the π_0. With such a large sample of measurable particles, STAR has the unique opportunity to describe the global features of the heavy ion collisions recorded during the summer of 2000.

CHAPTER 4

The Time Projection Chamber

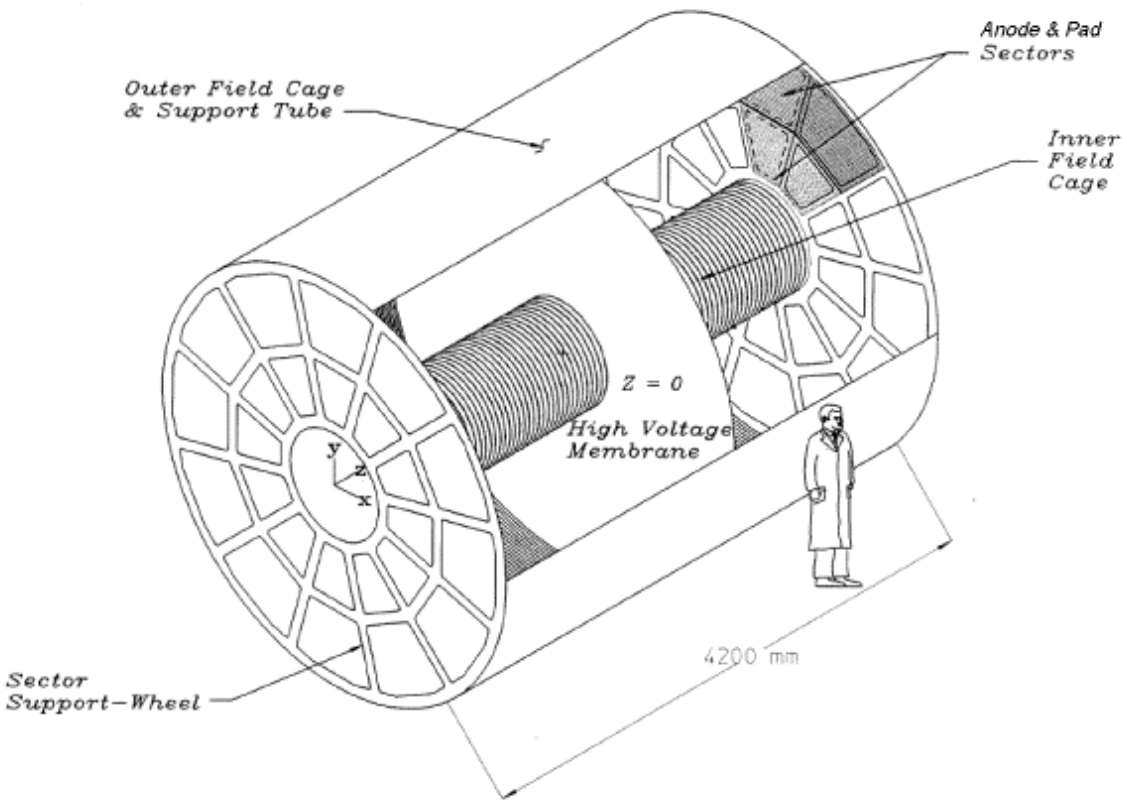

Figure 4.1: Sectioned view of STAR TPC. The major features of the STAR TPC are shown, including the inner and outer field cages, the high voltage central membrane and the MWPC sectors.

The TPC (Figure 4.1) is a fully pixelized drift chamber with a Multi-Wire Proportional Chamber (MWPC) [BR94] at both ends of the TPC for readout. The TPC has

144,000 pads which give xy coordinate information and up to 512 time buckets which provide z-position information for each hit, a total of over 70 million pixels.

Charged particles can be detected in drift chambers because they ionize the gas along their flight path. The energy required for them to do this is taken from their kinetic energy and is very small, typically a few keV per cm of gas under normal conditions. When a charged particle traverses the TPC volume, it ionizes on average gas atoms and molecules every few tenths of a millimeter along its path and leaves behind a cluster of electrons. Under the influence of an externally applied electric field, the electron clusters then drift at a constant average velocity to the readout electronics where their time of arrival and location are recorded.

In the STAR TPC, the electric field is provided by the outer field cage (OFC), the inner field cage (IFC), and the high voltage central membrane (CM) (Figure 4.1). The purpose of the OFC and IFC is to provide a nearly uniform electric field along the axis of the cylinder in which to drift the electrons to the anode plane, since any distortions in the field will result in a distortion of the recorded tracks. The OFC and the IFC also serve to define the active gas volume and were designed to contain the TPC gas and prevent it from being contaminated by outside air. The central membrane is located in the middle of the TPC and is held at a high voltage (-31 kV for the year 2000). The anode and pad planes are organized into sectors on each end of the TPC and the pads are held at virtual ground.

The OFC and IFC include a series of gradient rings (see Section 4.1) that divide the space between the central membrane and the anode planes. The total distance from the CM to either inner or outer sector anode planes is slightly greater than 2 meters (Figures 4.2 and 4.3).

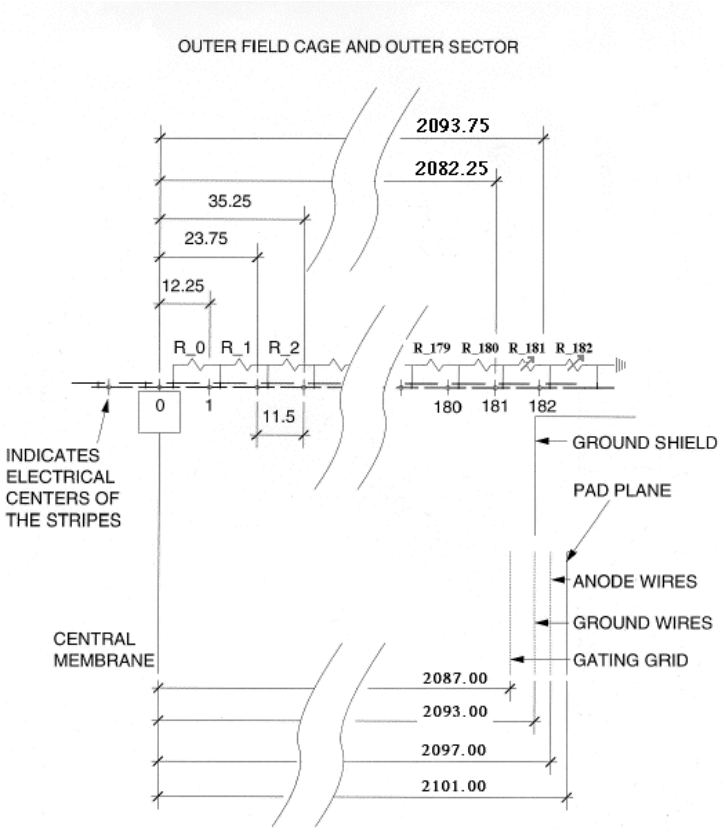

Figure 4.2: Outer Field Cage and outer sector dimensions. Dimensional units are in millimeters.

4.1 Field Cages

The field cages are designed to be low mass and "thin" for particles passing through them yet they must also be gas tight and strong enough to be self supporting. The field cages were built using two sheets of metal coated Kapton separated by a honeycomb of Nomex. The whole assembly was rolled into a tube and the sheets of Kapton were epoxied to the honeycomb to form a strong sandwich of material.

The Kapton in the outer field cage (OFC) (Figure 4.4) is laminated with a 35 micron layer of copper and the metal layer is etched into stripes so that, after rolling the tube, the stripes become rings around the tube. The inner field cage (IFC) (Figure 4.5)

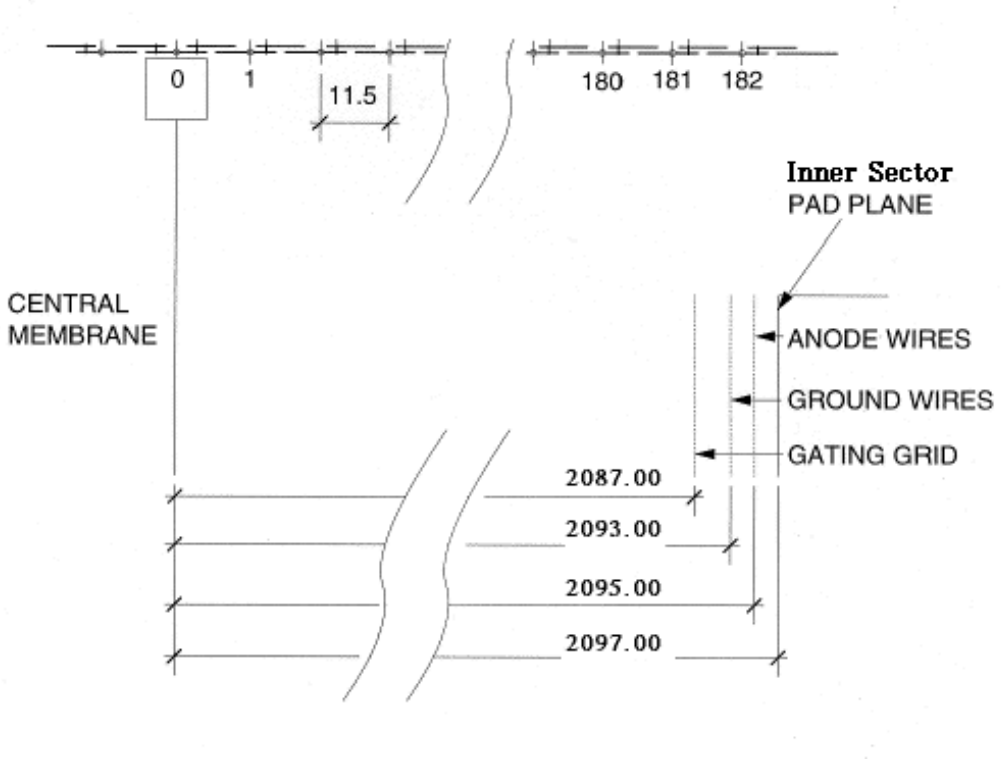

Figure 4.3: Inner Field Cage and inner sector dimensions. Dimensional units are in millimeters.

is similar to the outer field cage but the Kapton is laminated with a thinner layer of Aluminum (9 micron) and the Nomex layer is thicker (1.27 cm). The two sides of the tube are connected by metal pins. The stripes on one side of the tube are not aligned with the stripes on the other side; instead they overlap, with the stripes on one side centered over the gap on the opposite side. This allows the metal layers to become part of the mechanical structure of the tube which increases its strength. This also puts metal opposite the gap in the rings facing the TPC volume. The image charges developed on the opposite side of the gap are supposed to reduce the field distortions that might be caused by charge build up on the exposed Kapton in the gap facing the TPC.

There is approximately one ring per centimeter and the rings are biased by a chain

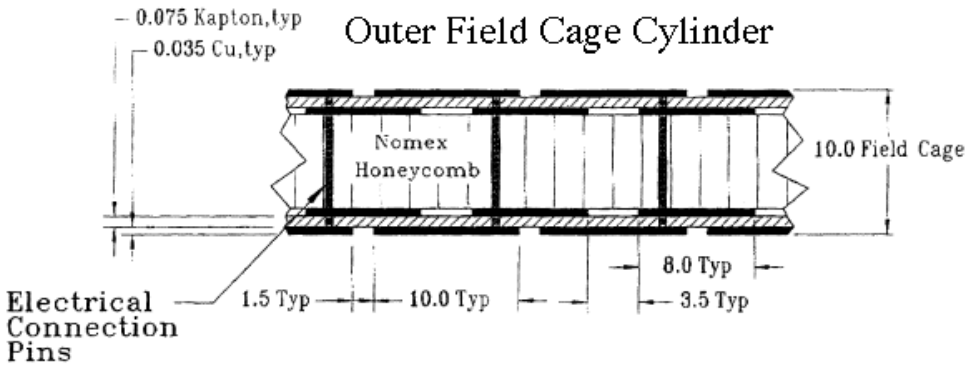

Figure 4.4: Outer Field Cage structure. Dimensional units are in millimeters.

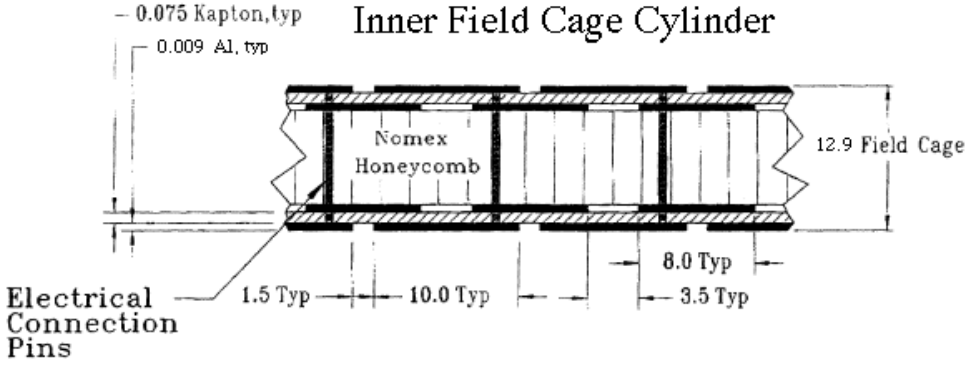

Figure 4.5: Inner Field Cage structure. Dimensional units are in millimeters.

of resistors that connect to the central membrane, the anode plane ground, and each of the gradient rings in-between. The rings are separated by two mega-ohm resistors and there are 182 rings and 183 resistors in each chain (Figures 4.2 and 4.3).

The last two resistors are adjustable and are housed in a rack which is external to the TPC. Note that the outer field cage has a ground shield attached to ring 182. It marks the end of the TPC drift volume and is used to better define the shape of the field at the terminus. The inner field cage does not have a ground shield. The spark gaps are safety devices for the protection of personnel and equipment in case the external resistors are disconnected while the field cages are biased.

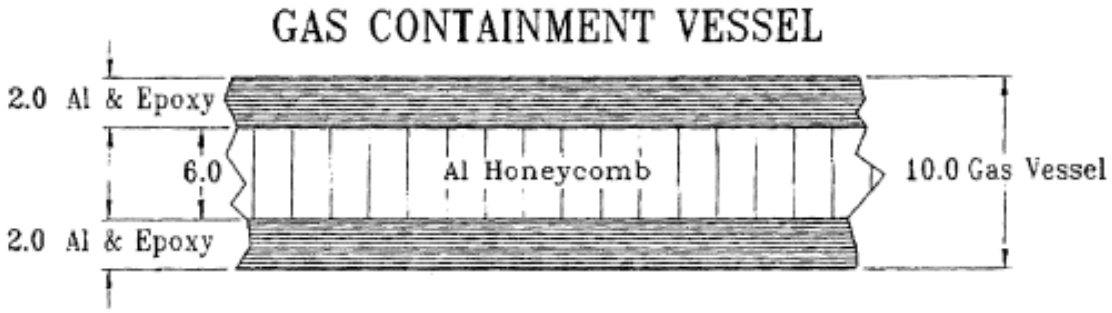

Figure 4.6: Aluminum gas containment vessel. Dimensional units are in millimeters.

The outer field cage is nested inside an aluminum gas containment vessel (Figure 4.6) which presents additional radiation lengths of material to particles passing out of the TPC in the radial direction. It is separated from the OFC by 5.7 cm of nitrogen gas. The gas vessel also has aluminum brackets glued onto its outer circumference to support the CTB trays and to temperature stabilize the TPC.

4.2 Multi-Wire Proportional Chamber

The MWPC's are located on the ends of the TPC. The MWPC's consist of three

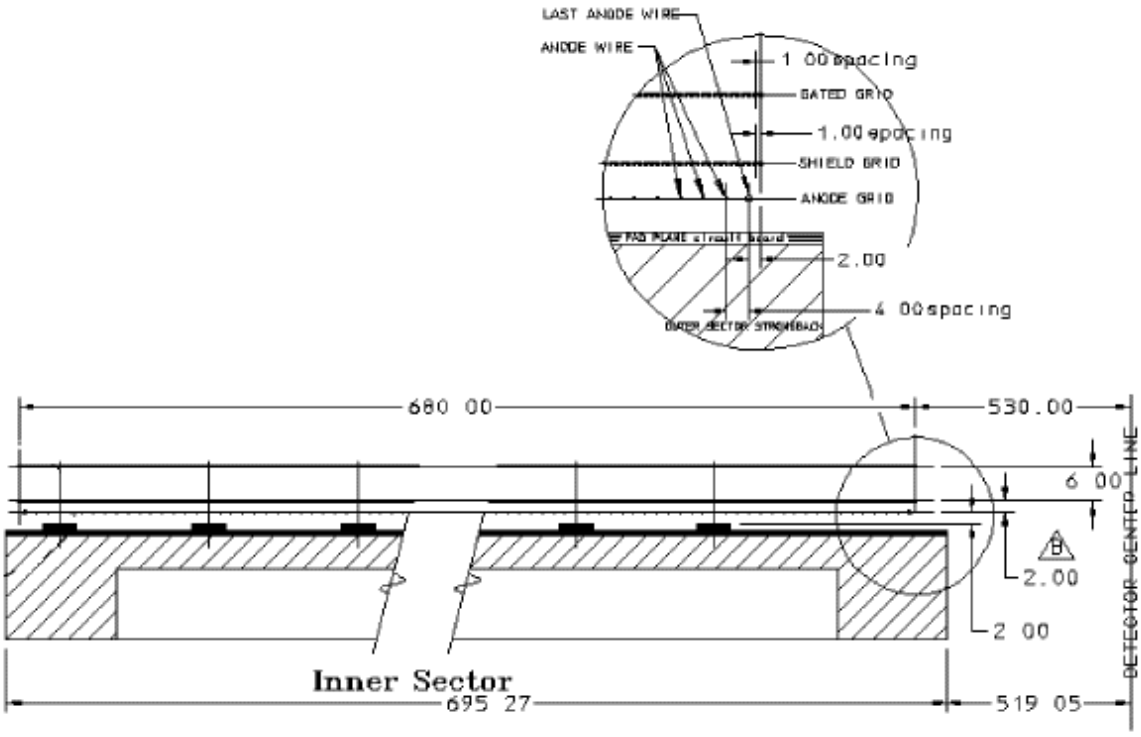

Figure 4.7: Inner sector wire geometry.

planes of wires and a pad plane (Figures 4.7 and 4.8) connected to the front end read-out electronics. The three wire planes are the gating grid, the ground grid, and the anode grid. The ground grid and gating grid help to define the drift field of the TPC. The anode wires are biased to a high voltage to provide the necessary electric field to avalanche the electrons from the track ionization.

The TPC is divided into 24 super sectors, each subsequently divided into an inner and outer sector (Figure 4.9). Although the inner and outer sector dimensions are slightly different, the ground grid and the gating grid are aligned to provide a uniform drift field.

Along with defining the drift field of the TPC, the ground grid and the gating grid perform other important tasks.

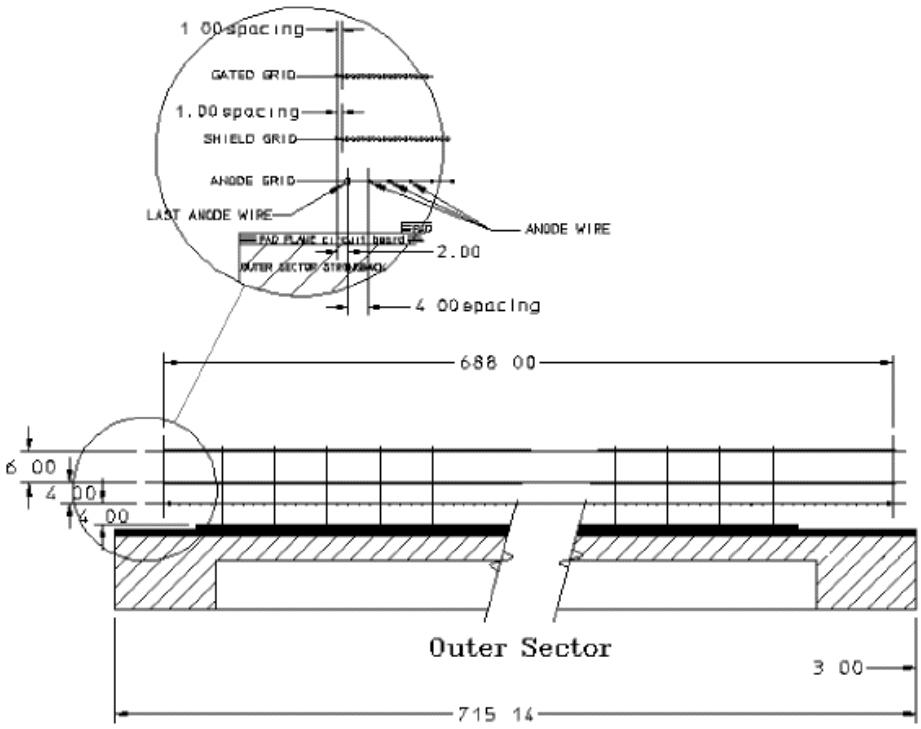

Figure 4.8: Outer sector wire geometry.

The gating grid separates the drift volume of the TPC from the amplification region. The gating grid controls the passage of electrons from the drift region into the amplification region, and prevents ions originating from the amplification process to enter the drift region. By biasing alternating wires on the gating grid positive and negative with respect to a reference voltage, the passage of ionization electrons is prohibited (Figure 4.10 (a)). When all wires are at the reference voltage, the nearby equi-pontential lines are nearly flat, allowing the passage of ionization electrons (Figure 4.10 (b)). The reference voltage on the gating grid is set such that when the grid is open, the grid is electrostatically transparent to drifting electrons. The gating grid is closed by shifting the voltages on alternate wires up or down symmetrically, leaving the average potential unchanged. Therefore, to first order, opening and closing the gating grid should only affect fields nearby.

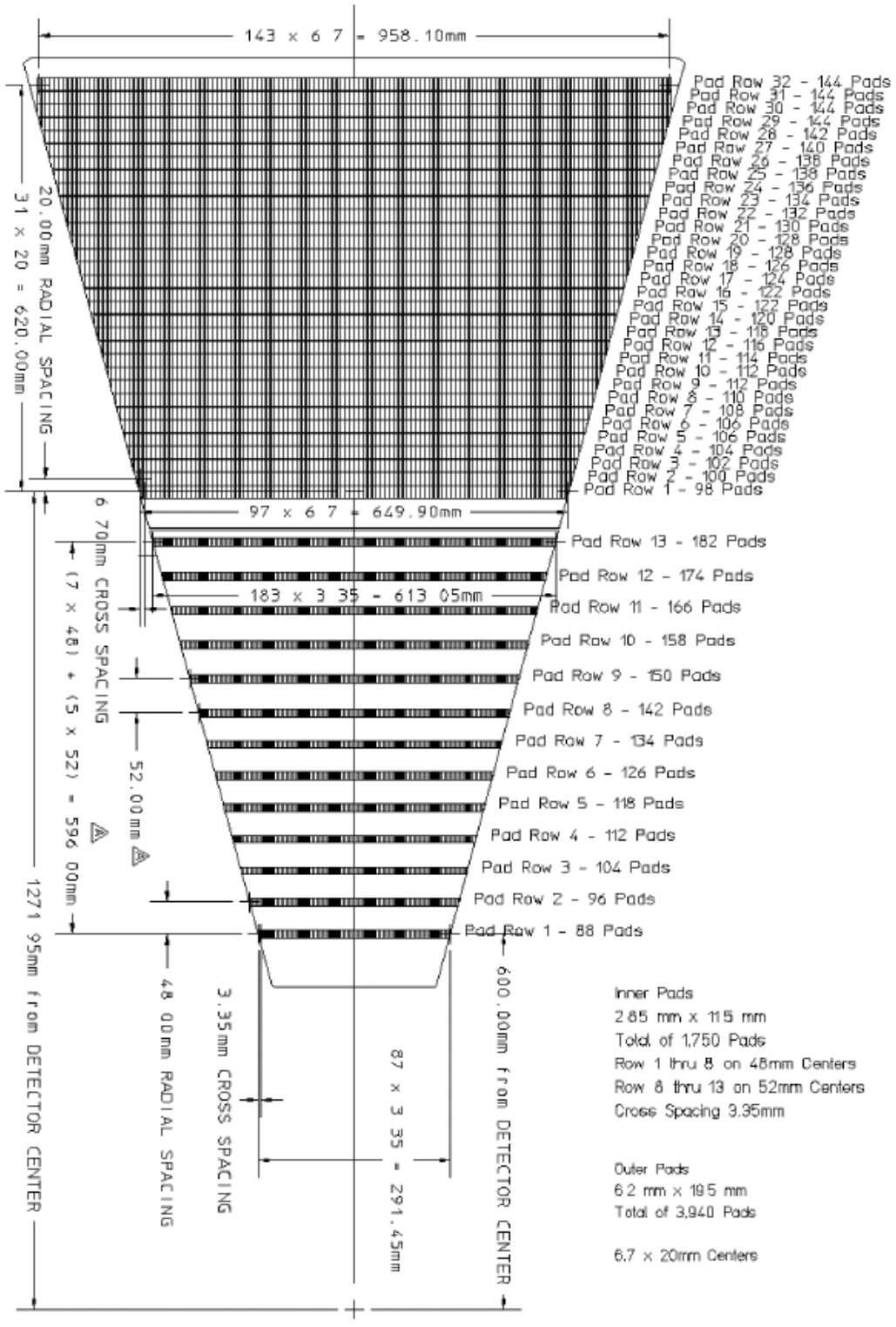

Figure 4.9: Super-sector pad plane layout.

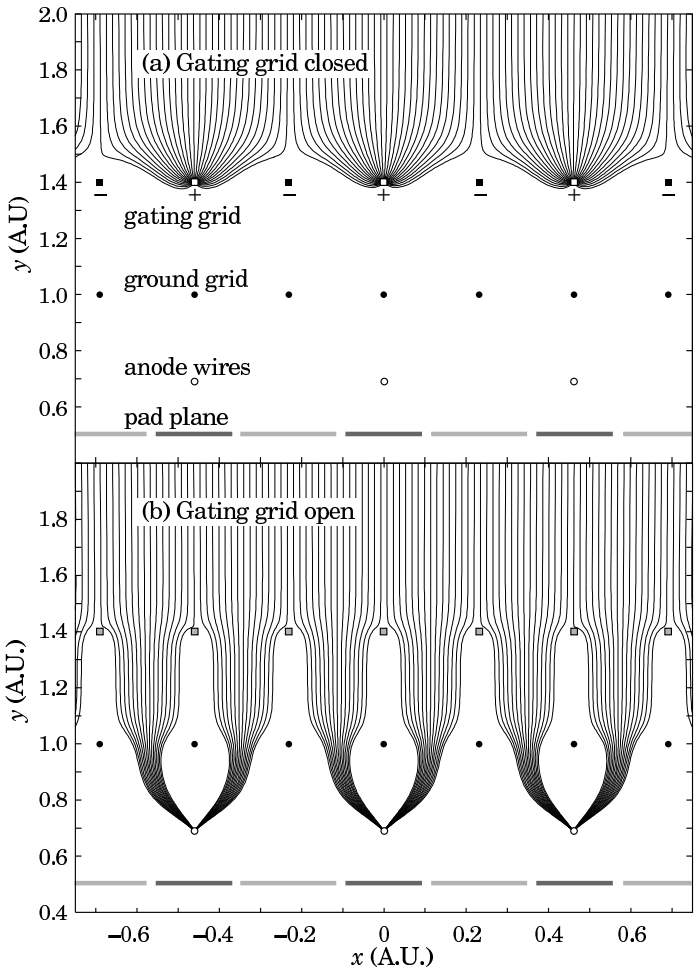

Figure 4.10: Drift field lines in a typical MWPC. The three wire planes, the gating grid, the ground grid, and the anode grids are shown as well as the pad plane. (a) Drifting electrons are collected on the gating grid until gated open by a triggering event. A shielding grid at ground potential is used to terminate the drift region. Electrons drift through an open gating grid (b) pass through to the amplification region around the anode wires. The motion of positive ions generated in the avalanche induces a signal on the segmented pad plane to provide precise measurements of ionization along the wire. The slow positive ions are blocked from entering the drift region by closing the gating grid after the electrons have drifted through. Figure was taken from the Particle Data Book [GG00].

Without the gating grid, ions from the amplification process would enter the drift region of the TPC, producing distortions in the drift field which would degrade the position resolution of the TPC. As MWPC's age, their performance tends to degrade. An increase of the dark current, a lowering of the gain, and a loss of pulse height resolution typically occur over time. At RHIC, where the charged track multiplicity per event is measured in the thousands, the MWPC would quickly deteriorate unless selection criteria are applied when recording events. By selectively reading out events, the life of the MWPC can be extended, simply because fewer electrons are being avalanched. Previous experiments employing MWPC's have reported performance losses with wire lifetimes of 10^{-4} Coulomb per cm of wire [BR94].

The ground grid lies between the anode wires and the gating grid. When switching, there is a large instantaneous current on the gating grid wires, which introduces noise into the MWPC. By positioning the ground grid with the gating grid on one side and the anode grid and pad plane on the other side, the ground grid helps to shield the pad plane and anode grid from feeling the full impact of the gating grid noise. The ground grid also helps to define the anode wire avalanche cells.

4.3 Anode High Voltage System

The anode wire high voltage system is powered using LeCroy 1471 high voltage power supplies. Two full systems are used, one controlling the inner sector high voltage and the other controlling the outer sector high voltage. There are a total of 192 channels for the anode high voltage system. Nominal operating voltages for the anode wires were +1390 volts DC for the outer sector and +1170 volts DC for the inner sector (Table 4.1) during the summer 2000 run. The LeCroy system can be controlled via both serial and ARCNet connections, the latter connection interfacing directly to the

slow controls system. There are serious limitations to communicating via the ARCNet connection, the greatest being the lack of block data transfers, which results in high levels of network traffic. Without block data transfers, the data refresh rate in the user interface is extremely slow, and the system crashes the vxWorks kernel when there is too much data being transferred simultaneously. The crashes of the kernel are due to a lack of scalability in the vxWorks interrupt buffer. One could argue that the problem is a vxWorks issue and not a LeCroy ARCNet. The problem was partially overcome by splitting the control of the two LeCroy power supplies to two independent cpus, thus reducing the amount of data being handled by the cpu at any given moment.

TPC Anode Wire Voltages	
Inner Sector (Volts)	1170
Outer Sector (Volts)	1390
TPC Gating Grid Wire Voltages	
Reference (Volts)	-127
Wire Bias w.r.t. reference (Volts)	± 75

Table 4.1: MWPC high voltage settings during the summer 2000 heavy ion physics run.

4.4 Gating Grid Driver System

The gated high voltage for the gating grid is supplied by custom modules designed and built at UCLA [Gha98]. The system consists of 12 pairs of modules, with each pair of modules controlling 4 sub-sectors. There are a total of 144 high voltage channels for the TPC gating grid. A complete set of functioning modules includes one VME control module and one high voltage module. Two modules are required because the control modules are VMEbus standard cards, while the high voltage modules reside in a crate with a special bus to supply the modules with power. The control modules communicate with a Motorola VME162 processor board, which handles the interface to the

STAR slow controls. The nominal operating voltages for all gating grid channels are -127 VDC for the reference voltage and ± 75 VDC on alternating wires (Table 4.1).

4.4.1 Gating Grid Operations

During the summer of 1999 cosmic ray testing, several problems with the gating grid drivers arose. Each high voltage stage in the gating grid consists of a switching power supply which pulses a transformer, rectifies and generates the voltage, which is then passed through a secondary linear regulator. Between the original prototyping and final production of the gating grid drivers, a component in the original design was phased out of production by the manufacturer. This component, a pass transistor (P-channel MOSFET) in the linear voltage regulation stage, was replaced by another component. It is controlled by an op-amp which compares the output of that transistor with the set-point voltage and varies the transistor's conductivity to match the output voltage to that of the reference voltage supplied by the control board. Unfortunately, we encountered problems because the replacement device did not have the capacity to deliver the required current when the voltage set-point on the gating grid was low. Although the occurrence is rare, this situation could occur during power up. For instance, in the case when the voltage drop across the MOSFET, ($V_{set\,point} - V_{out\,put}$), is maximum, we would need at least 0.5 - 1 mA just to measure it. This condition exceeded the safe operating parameters of the replacement MOSFET. We had failures in 10 percent (7 out of 72, including backup modules) of the high voltage channels, all traced to a failure in this single component. As a result, all 72 channels were repaired and upgraded to overcome this problem. This was done on site at the experimental hall and took two weeks to complete. Each module was then burned in for 5 days to ensure that the modification did resolve the problem and that other components were not compromised during the modification. Three more modules in production will include

this design change.

4.4.2 Mismatches in the Gating Grid Voltages

As part of the summer 2000 detector commissioning, I studied the transmission of electrons as a function of gating grid voltage and distortions to the drift field as a function of mismatched gating grid voltages. Both studies were conducted using the TPC laser system and with the magnetic field at 0.25 Tesla (half the nominal field strength). Electron transmission is a typical study conducted in TPC's and results from other TPC's have been published [BR94]. There are also solutions for the transmission function available which ignore the effects of gas diffusion [BR94]. Measuring the distortions caused by mismatched voltages allows us to set reasonable alarm limits on the high voltages.

The transmission study was done by keeping the gating grid in a closed state, with wires at their bias voltages. Laser triggers were sent, and we looked for traces of a laser signal in our data. This was repeated for different bias voltage settings. The study revealed two things. First, the gating grid completely attenuated the laser signal for all voltages that we were capable of setting. The gating grid drivers had difficulty with low bias voltage settings so we were unable to study this region of the transmission curve. The second result, which was more important, was the discovery that one of the sectors was always transmitting electrons. This was a cause for some concern since there were several possible failure points. There could have been anything from a cable problem up to a sector problem, the latter requiring the replacement of a sector. Fortunately, it was found that the high voltage gating grid cable for that sector was disconnected at the TPC sector connection. As a result, the voltage on that sector floated to an unknown value, allowing that sector to transmit electrons continuously. When we looked at the history of anode wire trips on the entire sector due to excess DC or peak currents, this

sector showed a pattern of trips when beam was in the accelerator, which were most likely due to severe beam losses. After the sector cable was connected, no trips have been recorded to date on that sector.

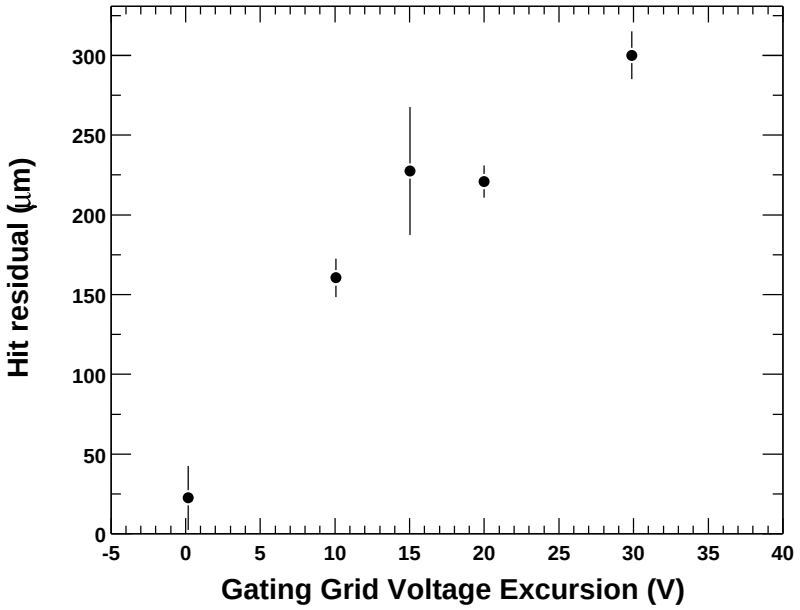

Figure 4.11: Mean *x* residual (along pad row) vs. gating grid voltage excursion.

The distortion study was done by varying the gating grid voltages on the 12 o'clock and 6 o'clock outer sectors. The residual of the hits in pad row 12 to 15 were then averaged over many laser events. From previous numerical calculations and discussions with the detector designers [Wie00, Wie00], we expected to see a systematic pull of the drift electrons in one direction if there was a voltage mismatch of at least 10 volts on the gating grid. Figure 4.11 shows the final result of this study. As expected, we see measurable effects when the voltages are mismatched by 10 volts, followed by a linear increase in the mean *x* residual.

4.5 TPC Gas

There are many factors that must be considered in choosing the best gas for the TPC. Gas purity, multiple scattering, drift velocity, cost, and safety are just a few of the more important issues.

The STAR TPC is very large and ionization electrons from a track may drift as much as two meters before reaching the anode plane. The gas must have sufficiently small attenuation for drifting electrons. Since the electron attenuation is a strong function of the oxygen and water content, the gas must be kept relatively pure. Typically, the oxygen and water concentrations should be kept below 40 parts per million. As a safety precaution, the entire detector will shut down if either the oxygen or water content exceeds 80 parts per million in the TPC gas. Oxygen poses an extra hazard when mixed with flammable gas. Due to the presence of high voltages on the wires of the MWPC, there is a potential for sparking which could result in ignition if the oxygen content is high. The experimental and safety requirements demand that the gas must be easy to re-circulate and clean in order to achieve these stringent standards. Noble gases are good candidates because they are easily cleaned with simple technologies and many pure organic gases are also easily handled. Examples of these gases are helium, argon, methane, ethane, and iso-butane.

STAR has considered two gas mixtures: Argon(90%)-Methane(10%), also known as P-10, and Helium(50%)-Ethane(50%). The noble gas component has a very low affinity for free electrons while the organic gases quench the propagation of UV photons throughout the TPC volume. This property of organic gases is critical for stable electron amplification. The avalanches near the anode wires produce many UV photons which could produce photo-electrons if they propagate to metal surfaces such as the pad plane or the other wire planes. If the UV photons were not quenched in the

gas, the photo-electric effect would lead to a catastrophic feedback effect where UV photons from an avalanche would produce more electrons which would lead to more avalanches. The argon-methane mixture will be used in the TPC because it is the least hazardous of the two. The argon component, however, increases the multiple scattering of the primary particle relative to helium so the best performance of the TPC would be achieved with the helium mixture. The dangers, however, posed by the helium-ethane mixture outweigh the benefits of better TPC resolution. The helium-ethane mixture requires a higher electric field to obtain an acceptable drift velocity, and the diffusion of helium may damage other detector systems in STAR. The STAR TPC will most likely continue to use P-10 throughout its lifetime.

4.6 TPC Gain Variations

The gas gain in the TPC is affected by the gas density and is measurable in the TPC. Since the TPC is operated at atmospheric pressure, the pressure is recorded by the gas system. According to the ideal gas law, the gas density (ρ) is proportional to the pressure of the gas (Equation 4.1).

$$P/T = \rho R \tag{4.1}$$

$$R = \text{ideal gas constant}$$

From Diethorn's formula for gain [Die56], we obtain Equation 4.2 [BR94]. In Equation 4.2, ΔV is the average potential difference an electron must traverse to obtain the required energy to produce one free electron from the TPC gas. The mean charge per unit length on the anode wire is denoted as λ, and ε_0 is the permittivity of free space. The constant (S) is negative because as the density of the gas rises, the mean free path of the electrons decreases. As a result, the mean of the electron kinetic energy distri-

bution decreases, resulting in fewer electrons which exceed the threshold energy for multiplication.

$$\frac{dG}{G} = S\frac{d\rho}{\rho} \qquad (4.2)$$
$$S \equiv \frac{\lambda ln2}{\Delta V 2\pi\varepsilon_0}$$

With STAR, the TPC temperature was well regulated so one can reduce Equation 4.2, using the ideal gas law (Equation 4.1) to relation 4.3.

$$\frac{dG}{G} = S\frac{dP}{P} \qquad (4.3)$$

Since the gas pressure was monitored, the variations can be accounted for. The TPC gas system parameters were stored in the conditions database, which is briefly described in Section 4.9. Figure 4.12 is a plot showing the result of a study done in

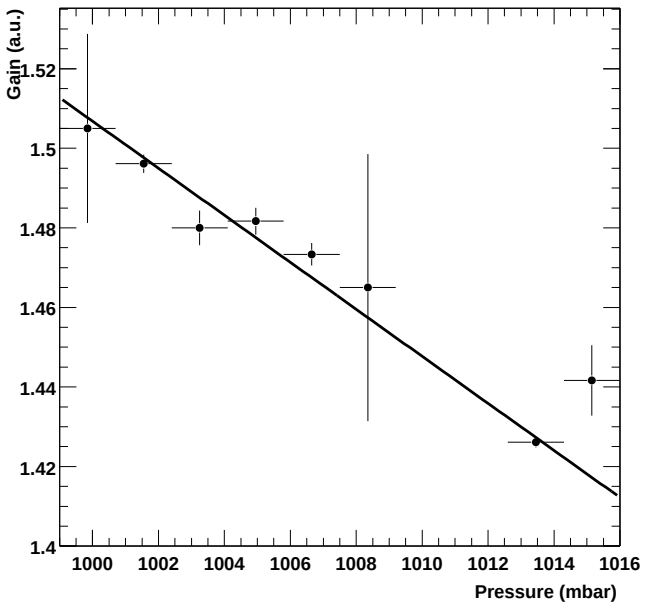

Figure 4.12: Change in gain vs. change in pressure in the STAR TPC.

October 2000 of the relationship between gain and pressure in the STAR TPC. The results were obtained by calculating the mean position of the pion band in the momentum range $0.25 < p < 0.30$ GeV/c for several runs. This number was then compared to the pressure during the run. The pressure was corrected for a calibration offset in the barometric pressure readings from the TPC gas system. With this data, the slope, *S*, in Equation 4.3 was extracted and found to be -3.7.

4.7 TPC Drift Field

The STAR TPC uses the field cages to establish a longitudinal electric field to drift the electrons from any point in the TPC to the multi-wire proportional chambers. The drift rate is a function of the applied field, but the relation is non-linear and depends on the gas composition (Figure 4.13).

4.7.1 Drift Velocity

For accurate track reconstruction, it is reasonable to choose an electric field near the peak in the drift velocity curve. This ensures that the drift velocity is saturated and the drift velocity is least sensitive to minor changes in the gas pressure or temperature caused by the local environment. The STAR TPC, however, has an automatic drift velocity stabilization feedback loop which works by monitoring the drift of laser tracks in the TPC. Since the origin of these tracks is well known in time and space, it is easy to calculate the actual drift velocity and to apply corrections to the drift field to compensate for any time dependent variations in the gas properties. The operating point for the drift velocity must therefore be slightly off peak in order to provide some slope to the observed changes in parameters and to avoid the problem of a double valued solution when the drift velocity is observed to drop. A review of Figure 4.13

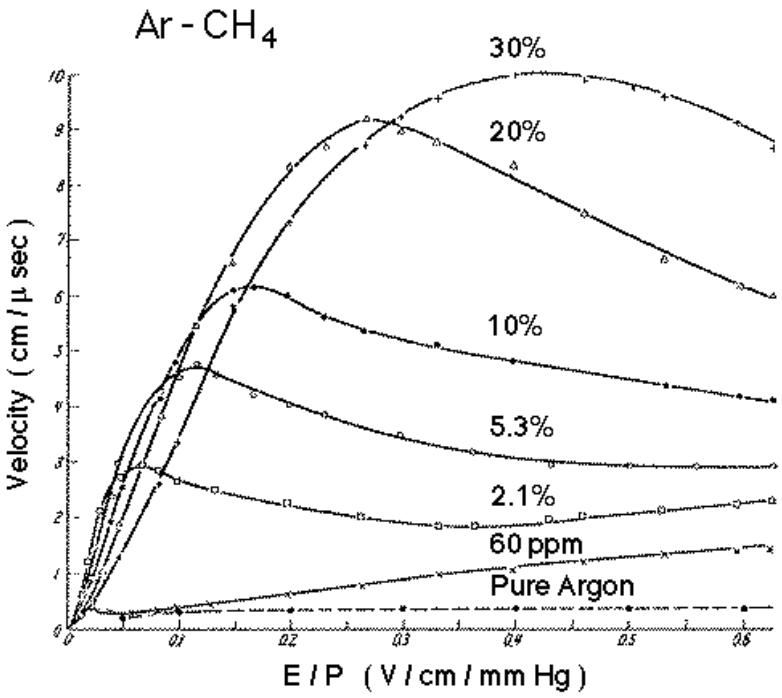

Figure 4.13: Drift curves: velocity vs. E/P.

reveals that any reduced field greater than 0.16 V/cm/mm-Hg satisfies these conditions. Transforming to standard temperature and pressure, this means the drift field should be slightly greater than 120 V/cm, which is why the TPC is operated at an average gradient of about 145 V/cm.

We tested the drift velocity stabilization feedback loop during the summer 2000 run but did not use it for data taking. In retrospect, I believe this was the correct choice. While a feedback loop to stabilize the drift velocity is appealing, there are many pitfalls to this. The most obvious is the need to track not only field cage voltage but also the gating grid voltage accordingly. If the gating grid voltage is not adjusted, there will be a field mismatch at the gating grid, which will distort the drift field. Another concern is the stability of the feedback loop. It is conceivable to have a runaway feedback mechanism, either in the form of oscillations or a complete divergence from a reasonable voltage setting.

4.7.2 Imperfections in the Drift Field

There are many ways the the TPC drift field may be distorted. These include:

- Misalignment of the TPC in the magnet. If the center-line of the magnet does not correspond to the center-line of the TPC, there will be an ExB effect.
- Misalignment, bulging or other deformation of the central membrane will cause distortions near the center of the TPC.
- Misalignment of the TPC sectors in z.
- Mismatches in sector and field cage voltages
- Distortions due to defective wire connections, or lack of MWPC wires at sector boundaries

- ExB effect due to a component of the magnetic field in the $r-\phi$ direction. This is the major ExB effect we correct for, and is present in all solenoidal magnets.

It was shown [LWT00] in November 2000 that there is a constant distortion at the inner-outer sector boundary. This distortion has been attributed to a gap in the wiring of the MWPC. There is at least a 1 cm region near the inner-outer sector boundary (pad rows 13–14) which has no wiring. The field in that region is no longer uniform, and causes the distortion seen in Figure 4.14. Other distortions away from the boundary have been attributed to the $r-\phi$ magnetic field component.

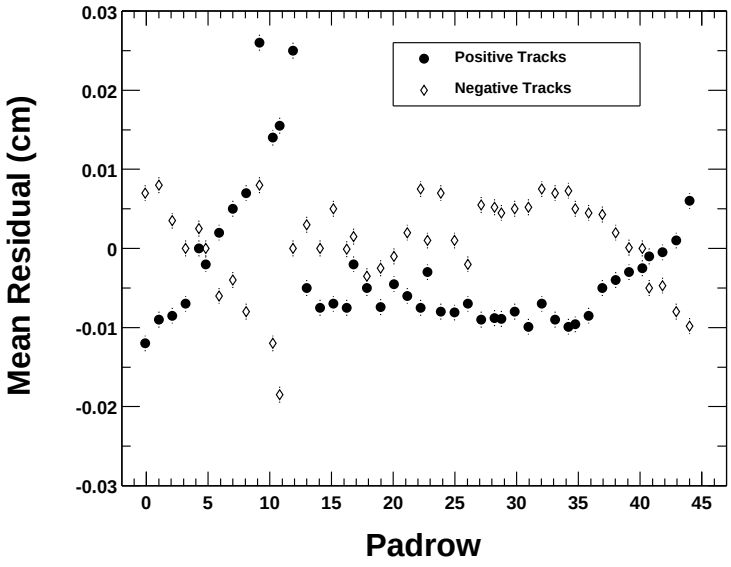

Figure 4.14: Mean residual (cm) in *xy* plane vs. pad row for tracks with $0.4 < p_t < 1.2$ GeV/c. No electric or magnetic field distortion corrections applied. Note the discontinuity at pad row 13 and 14, which is the inner/outer sector boundary.

This effect was not apparent during the distortion study (Section 4.4.2) most likely because of two reasons. The first reason is that the distortion is bipolar across the sector boundary, which effectively canceled out when I averaged over both inner and

outer sector pad rows. Secondly, the laser tracks are very wide, which reduces our sensitivity to distortions.

4.8 STAR TPC Slow Controls

The Gating Grid Drivers (GGD) for the TPC and FTPC as well as all other TPC subsystems are controlled using EPICS, the Experimental Physics and Industrial Control System. EPICS is a set of software tools and applications originally developed by Los Alamos National Laboratory and Argonne National Laboratory for the purpose of building distributed control systems to operate devices such as particle accelerators, large experiments, and telescopes. EPICS is built on a software communication bus. The functional subsystems, which provide data acquisition, supervisory control, closed loop control, archiving, and alarm management greatly reduce the need for low level programming.

Using EPICS, a substantial set of software has been developed to control the STAR TPC. This software includes distributed databases to provide local control of the TPC subsystems. The databases are loaded and executed in I/O Controllers (IOCs). The databases provide data acquisition, data conversion, alarm detection, interlocks, and closed loop control. The STAR IOCs consist of a VME back-plane, a 68020 CPU running the vxWorks real-time kernel, an ethernet connection, and a serial port. At UCLA, a database was developed to control the GGD. Control of the gating grid's analog input and output, along with digital output has been achieved.

At the heart of EPICS is Channel Access (CA), which is the software bus provided to communicate between various EPICS subsystems. CA allows the system components and user extended components to perform channel connections, gets, puts, and monitors on any field of the database using TCP and UDP protocols. Channel connec-

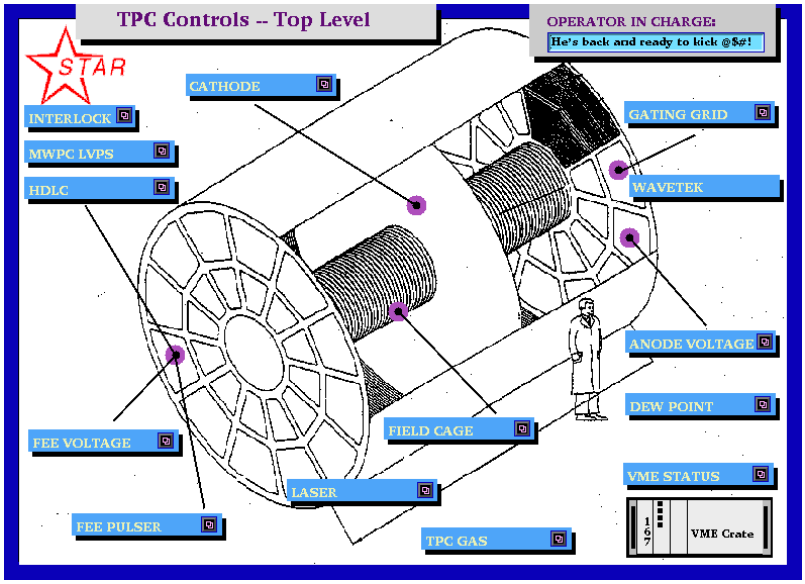

Figure 4.15: Top level user interface for the STAR TPC slow controls. All TPC controls are accessible from this point of entry.

tions are performed by connecting a unique channel name to the IOC containing the channel. CA provides notification to its clients when a connection is broken and another notification when it re-connects. This connection management is used to keep all subsystems informed of the status of other IOCs, on which it may depend for parameter information. This is essential in STAR since all TPC subsystems are interconnected.

Although the software structure is quite complicated, the end user interacts with the TPC subsystems through easy to use Graphical User Interfaces (GUI's). The GUI's were built using the Motif-Based Editor and Display Manager (MEDM). MEDM allows the experimenter to easily control the relevant parameters for the TPC by taking care of CA. Figure 4.15 shows the top level user interface for the STAR TPC. From this point, an operator can control any of the TPC subsystems. Figure 4.16 shows the Gating Grid main control interface. From here, sectors may be controlled independently or together.

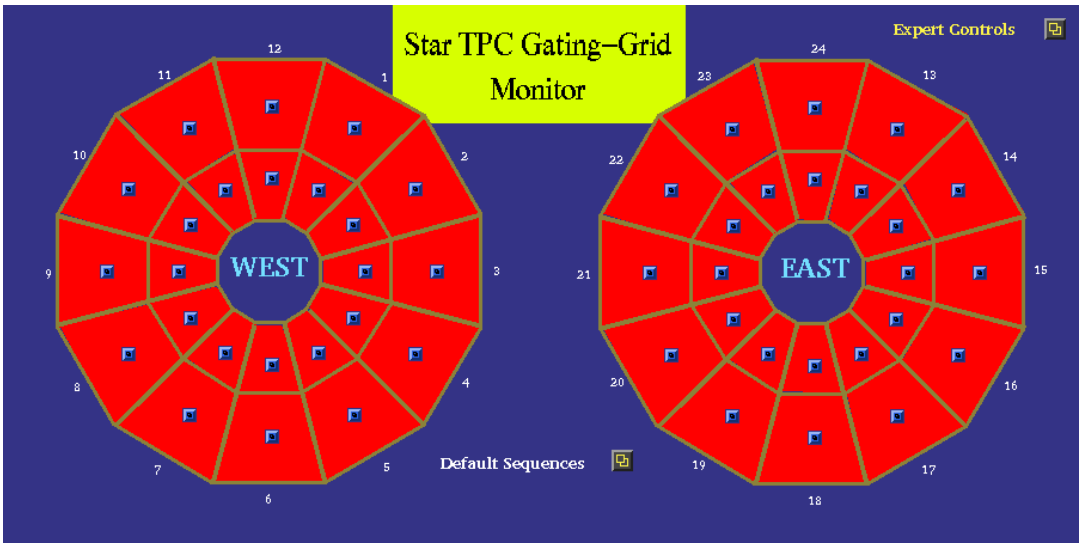

Figure 4.16: User interface for the gating grid driver controls. From this GUI, the user can monitor the operating state all 48 sub-sectors.

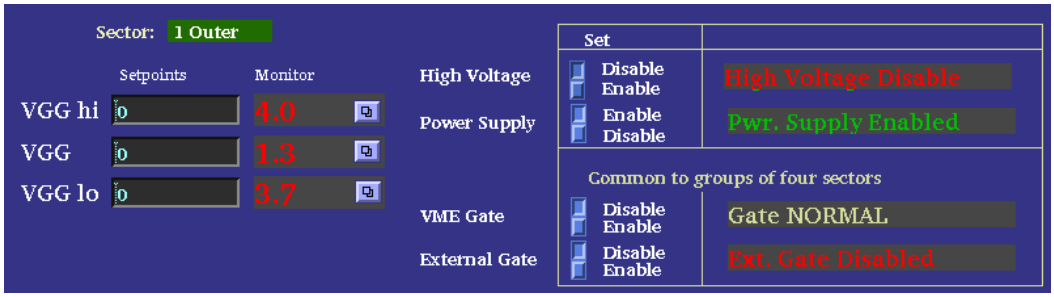

Figure 4.17: User interface for the gating grid sector control. This GUI controls the power supply and high voltages for one sub-sector, sector 1-outer.

Figure 4.17 is the gating grid sector control interface. With this, the various parameters for each sector may be controlled. GGD parameters that are adjustable by the experimenter include the power supplies, high voltage output enable, control of the gating action and control of the high voltage set-points. There are a total of 264 parameters which must be specified. To maximize the ease of use, the GGD includes global controls (Figure 4.18). Global control allows an operator to set all 24 sectors of the TPC to the same state. Threshold levels for the high voltage minor and major alarms are also set on this GUI. Finally, a set of automated control software was developed to bring the GGD online. The TPC operator may turn the GGD on or off by simply pressing a single button.

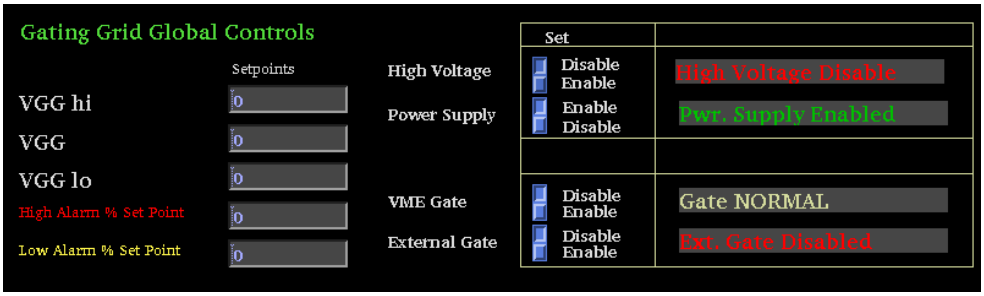

Figure 4.18: User interface for the gating grid global controls. From here, all 48 sub-sectors may be controlled in unison. This is ideal for normal operations in which all sectors have the same voltages.

Installation of the GGD modules included calibration of the high voltage outputs. Each of the 144 high voltage outputs on the gating grid were calibrated to within one percent of the requested value. This high degree of uniformity is necessary in the TPC because the potential on the gating grid affects the drift field in the TPC and delineates the drift volume of the TPC from the amplification region. The gating grid must match the potential of the field cage to prevent distortions in the drift field of the TPC. A mismatch produces a transverse component of the electric field, distorting the trajectories of drifting electrons. Deviations of $\sim$ 10 volts between the gating grid

and the field cage will cause unacceptable distortions in the drift field. These same deviations in the gating grid potential could also affect the transparency of the gating grid to electrons. This will affect the quality of the signals by decreasing the number of drift electrons that reach the sense wires for amplification.

Calibration of the GGD output voltages was done in three steps. Given a set point for each high voltage channel, the first step was to determine the actual output voltage onto the TPC and comparing this value with the monitored value. The output to the TPC was measured using a voltmeter and a oscilloscope with voltage divider probes. The associated uncertainty within the voltmeter and scope was small and thus neglected. The ADC read-back value was always calibrated first because it is considered more reliable than the DAC output value. The DAC has an associated integral non-linearity which makes it less favorable to use in calibration. The DAC output is also dependent on a reference voltage, which also makes the DAC unfavorable to use in the calibration process. The ADC scale was adjusted in the software so that the monitored read-back corresponded to the actual voltage out of the GGD. Once this was accomplished, the DAC scale was adjusted so that the output and monitored voltages matched the requested voltage to within one percent. The final step was to adjust the gain on the output of the DAC. Code was written in the EPICS framework to effectively correct the gain of the DAC. This involved measuring the output voltage for several set-points, calculating the actual gain, and then adding a gain correction in the software to achieve a gain of one.

An automatic calibration system was developed to calibrate the Gating Grid Driver modules. The calibration software was designed to run in vxWorks and when necessary, the calibration code is uploaded into the control VME crate. With the software in place, only the ADC calibration must be performed by a systems specialist. The calibration of the DAC and gain correction are both handled completely by software.

4.9 TPC Conditions Database

STAR employs a mySQL database to store important information. This information includes run information, DAQ configurations, detector calibrations and detector conditions information. There are over 5000 separate conditions parameters recorded for the TPC. TPC conditions information includes voltage read-backs, power supply status, trigger status, network status, and gas system parameters. All parameters are retrieved from STAR's slow controls system.

Service daemons were created to store TPC conditions information. The daemons are clients designed to monitor TPC parameters via EPICS CA and store the readings in the STAR online conditions database. Various C++ Application Programmer Interfaces (API)'s were developed by STAR online personnel to allow clients to interface with STAR's mySQL database. There were two main requirements for the service daemons. The first is the ability to handle massive amounts of information. This includes not only the ability to read thousands of values, but also to write values selectively, based on criteria such as a minimum change or a maximum time interval between writes. The second consideration is stability. The daemons have to be up 100% of the time. As such, the code must be tolerant to faults such as excessive network traffic, which would cause delays in reading conditions information from the TPC.

To allow user friendly operation of the archiving system, shell scripts were developed to allow easy command line user interface in the UNIX environment. Functionality in the script includes the ability to start and stop an archiving run, and also an option to check the status of the daemon. Error logging for the daemon is handled via the system logger. The error messages are then logged in the system log files for later retrieval. If a fatal error occurs, diagnostic e-mail is sent to relevant personnel, describ-

ing the error condition. There is also a web-page [1] which gives up to date information on the status of the archiving daemons.

[1] http://onlsun1.star.bnl.gov/cgi-bin/startpc/status.cgi

CHAPTER 5

Analysis Methods

5.1 Trigger

Data used in this analysis was taken with two different trigger conditions: a minimum-bias trigger requiring a coincidence between both ZDC's and a central trigger additionally requiring a high energy deposition in the CTB. The central trigger corresponded to approximately the top 15% of the measured cross section for $Au+Au$ collisions. Data from both the minimum-bias trigger and central trigger were used for this analysis. STAR recorded 761,000 minimum-bias events and 884,000 central events. For the results presented here, a combined total of 750,000 minimum-bias and central trigger events were used.

5.2 Event Selection

Event Cuts	
Primary Vertex Position	-80 cm $< z <$ 80 cm
Number of Bins for Primary Vertex Position	16

Table 5.1: Event selection criteria common to all centrality classes.

The results that are presented have been extracted from events which passed certain criteria. These criteria are listed in Table 5.1. As mentioned previously in Section 3.1.2, the collision vertex position varied considerably during the summer 2000 run.

As a result, the pseudo-rapidity (η) distribution of the accepted particles varied event to event and it was necessary to apply a cut on the position of the primary vertex. Events were selected with a primary vertex z position (z) from the center of the TPC of $|z| < 80$ cm. These events were further divided according to z into 16 bins (10 cm per bin) to facilitate the background calculation, which is discussed in Section 5.5.

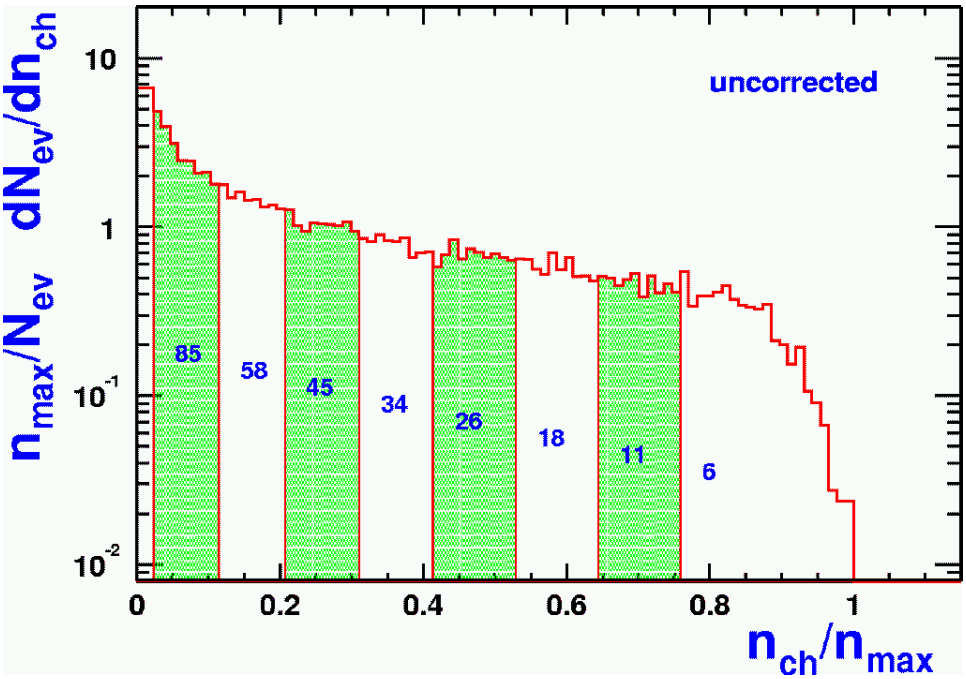

Figure 5.1: The minimum-bias primary track charged multiplicity distribution in a pseudo-rapidity interval $-0.75 < \eta < 0.75$ as a function of the number of tracks normalized by the maximum observed number of tracks. The eight centrality regions used in this analysis are shown. The integral under the curve is 1.0 and the cumulative fraction corresponding to the lower edge of each centrality bin is indicated as a percentage. Figure taken from [Ack01].

For the centrality measurement, the total charged multiplicity distribution within a pseudo-rapidity window $|\eta| \leq 0.75$ was divided into three bins: 20–360, 360–560 and ≥ 560. These bins correspond to 85–26%, 26–11% and the top 11% of the measured cross section for $Au + Au$ collisions [Ack01]. Figure 5.1 shows the uncorrected charged multiplicity distribution for minimum-bias events and the centrality binning. The coarse centrality definitions were required due to the limited statistics available

from the year 2000 data-set. Table 5.2 describes the flow centrality binning. The three centrality bins correspond to flow bins 1–4 in the low multiplicity centrality, bins 5–6 for the mid-central bin, and bins 7–8 for the central bin.

Centrality Bin	Measured cross section	Geometric $Au+Au$ cross section
1	58–85%	53–77%
2	45–58%	41–53%
3	34–45%	31–41%
4	26–34%	24–31%
5	18–26%	16–24%
6	11–18%	10–16%
7	6–11%	5–10%
8	Top 6%	Top 5%

Table 5.2: Flow centrality as defined in reference [Ack01]. Charged multiplicity is measured within a pseudo-rapidity window $|\eta| \leq 0.75$ for an event. The numbers for both the measured cross section as well as the geometric cross section associated with each centrality bin are listed.

5.3 Track Selection

Track Quality and Kinematic Cuts	
Track Distance of Closest Approach to Primary Vertex	< 3 cm
Number of Hits on Track	> 15
Number of Hits on Track/ Total Possible Hits	> 0.55
$\lvert$Pseudo-rapidity$\rvert$ (η)	< 1.1
Momentum of Track	> 0.1 GeV/c
Momentum of Track	< 1.0 GeV/c
Particle Identification Cuts	
Kaon PID Efficiency	$< 2\sigma_k$

Table 5.3: Requirements placed on candidate K^+ and K^- tracks. These cuts are optimized taking into account requirements for adequate signal and minimization of background while reducing possible systematic uncertainties from the efficiency calculation.

Tracks were selected using the criteria listed in Table 5.3. Tracks were required to originate from the primary interaction vertex. This cut was applied globally during the

reconstruction phase and required that the extrapolation of the track helix pass within 3 cm of the reconstructed primary interaction vertex. Reconstructed tracks were also required to have at least 16 space points used in calculating the track parameters, and a ratio of the number of space points used in the reconstruction to the total possible number of space points to exceed 55%.

Kinematic cuts were also required for various reasons. A pseudo-rapidity cut of $|\eta| < 1.1$ was applied to the candidate tracks to reduce acceptance-induced multiplicity variations at large η, which could cause distortions in the mixed-event background calculation. The candidate tracks were also required to have a transverse momentum (p_t) in the range $0.1 < p_t < 1.0$ GeV/c. The upper limit on the p_t was in place to reduce the combinatorial possibilities, hence the computational time. The upper p_t cut was high enough to reduce the computational time while allowing for the reconstruction of all the available signal. The lower p_t cut was in place but had a negligible effect on the overall efficiency because there is a low momentum cutoff associated with energy loss of kaons through the beam pipe and detector material at a momentum $p \simeq 0.130$ GeV/c.

Particle identification (PID) was achieved by correlating the ionization energy loss (dE/dx) of charged particles in the TPC gas with their measured momentum (Figure 5.2). By truncating the largest 30% of the dE/dx values along the track, a sample was selected to calculate the mean $\langle dE/dx \rangle$. For the highest multiplicity events, the average $\langle dE/dx \rangle$ resolution was found to be about 11%. The measured $\langle dE/dx \rangle$ is reasonably described by the Bethe-Bloch function smeared with a resolution of width σ. Tracks within two σ of the kaon Bethe-Bloch curve were selected for this analysis, which allows the reconstruction of adequate signal while keeping the combinatorial background to a reasonable level to allow for the extraction of a statistically significant signal.

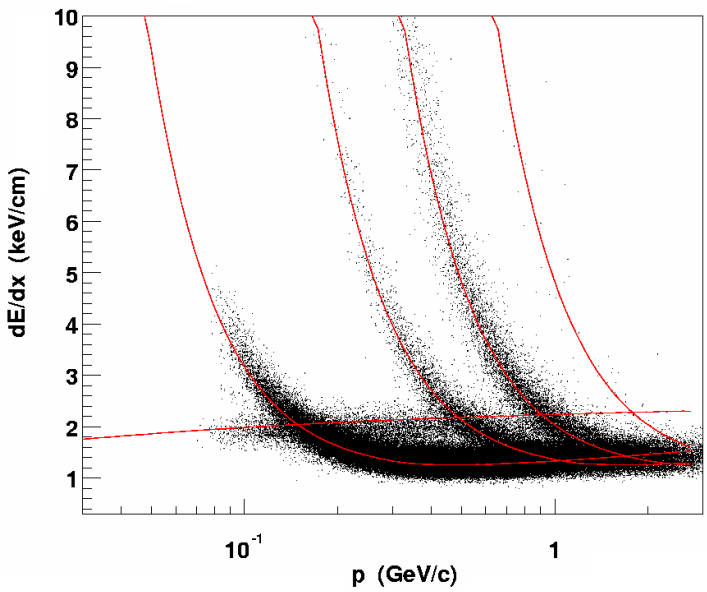

Figure 5.2: The measured $\langle dE/dx \rangle$ vs. p for reconstructed tracks in the TPC.

The cuts in use are optimized to reduce the reliance on detector simulations, minimize effects from run-by-run variations in the data-set and maximize the signal to background ratio. The Monte-Carlo may affect the results because we need to apply corrections to the raw data for the effects of detector acceptance and software efficiency. While maximizing the signal to background ratio is important for the statistical precision of the measurement, the most pressing issue was ensuring the validity of the result. With this caveat, the focus of the analysis was on obtaining adequate statistical significance for the measurement of ϕ meson production while reducing the systematic uncertainties in the results which may be introduced from the simulations.

5.4 Building the Signal

Reconstruction of the ϕ meson was accomplished by taking all tracks that passed

the cuts and calculating kinematic quantities for all possible permutations of these tracks. Figure 5.3 shows the K^+K^- invariant mass distribution in nine p_t bins at mid-rapidity ($|y| < 0.5$) for the 11% most central events. For comparison, Figure 5.4 shows the K^+K^- invariant mass distribution from low multiplicity events. The signal to background is considerably better in low multiplicity events (Figure 5.4) since the random combinatorial background is drastically reduced.

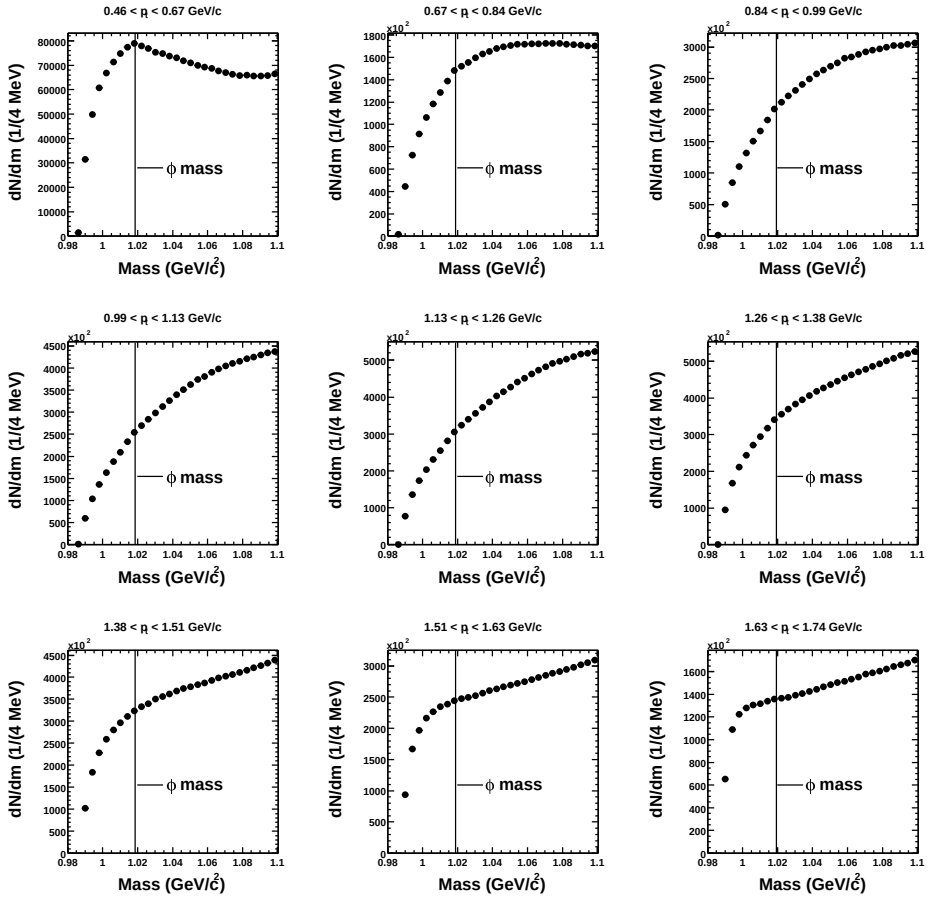

Figure 5.3: Invariant mass distribution for nine p_t bins at mid-rapidity ($|y| < 0.5$) for the 11% most central events. The vertical line marks the PDG [GG00] mass for the ϕ meson. The errors on the points are smaller than the size of the markers.

In this method there is a delicate balance between considerations of signal efficiency and the statistical uncertainty. If our track selection is too stringent, we will

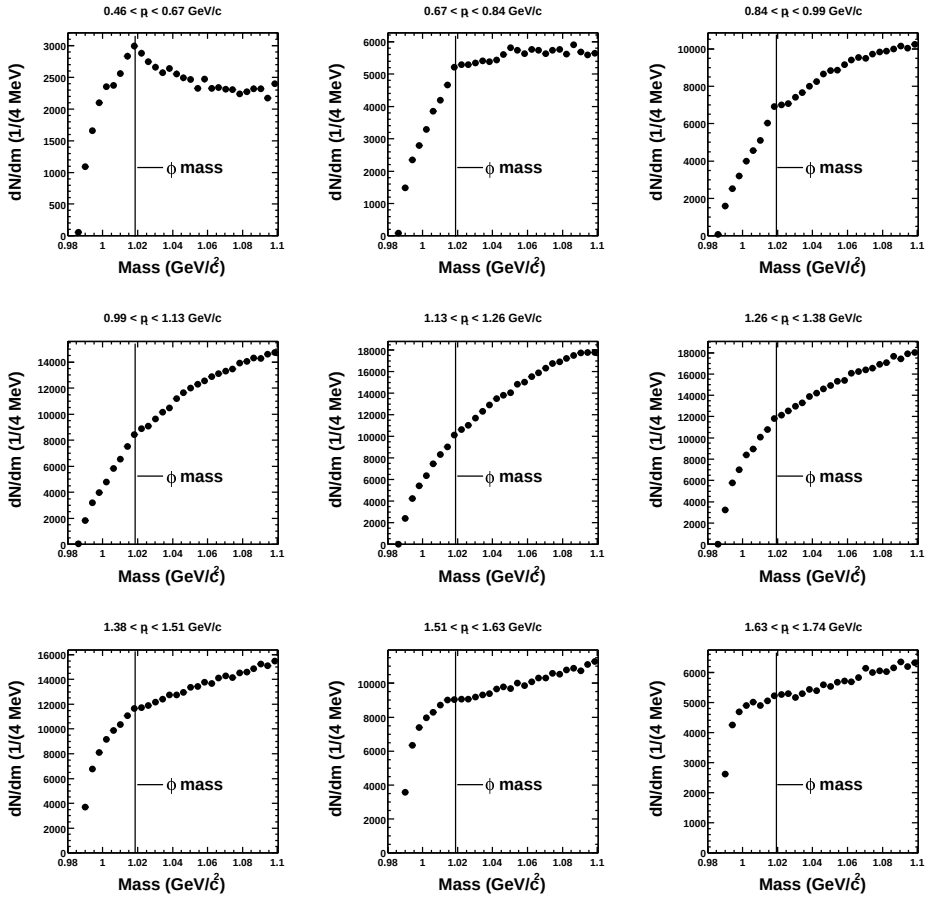

Figure 5.4: Invariant mass distribution for nine p_t bins at mid-rapidity ($|y| < 0.5$) for the 85–26% centrality bin. The vertical line marks the PDG [GG00] mass for the ϕ meson. The errors on the points are smaller than the size of the markers.

lose signal but at the same time increase the ratio of signal to background. Tight cuts also increase our dependence on simulations and our sensitivity to run-by-run variations. On the other hand, if we loosen the track requirements, we increase both the computing time and also the $\sqrt{N}$ statistical fluctuations from random combinations of track pairs.

5.5 Describing the Background

All selected K^+K^- pairs for each event passing the track selection requirements defined in Section 5.3 are plotted in the invariant mass distribution. There is no way to distinguish a K^+K^- pair from a ϕ meson decay from random combinations of K^+ and K^- candidates produced in the collisions and accepted into the TPC. The signal peak in the invariant mass distribution therefore sits on a large background from random combinations of uncorrelated K^+ and K^- candidates. Fundamental to the measurement of the ϕ meson peak in the K^+K^- invariant mass distribution is the ability to correctly estimate and subtract this background. The event mixing technique, originally proposed by Kopylov [Kop74] and further elucidated by L'Hote [LH94] and Drijard, Fischer, and Nakada [DFN84] provides a powerful method for estimating the background distribution.

5.5.1 Event Mixing

Suppose we have a sample of pairs formed from single tracks with truly uncorrelated momenta. From this original sample of pairs, a second, mixed-event sample of pairs is formed, in which a pair partner is taken from one event and the other pair partner is taken from a different event. In the case of either sample, the form of the invariant mass distribution arises from the random sampling of the acceptance and

efficiency-modified momentum space distribution of the pair partners. The invariant mass distribution for the mixed-event sample must have the same form as that of the original sample.

The same-event sample is of interest because it contains a subset of signal pairs for which the pair-partner momenta are in fact correlated. The classical application of the event mixing technique is the study of like-particle correlations. In this case, the assumption is that the only correlation between the momenta of like particles from the same-event is statistical, and that event mixing this sample will destroy this correlation. The resulting relative momentum distribution will resemble the product of the single particle inclusive momentum distributions, but will also contain experimental acceptance and reconstruction biases: everything of significance to the correlation analysis is contained except for the correlation itself.

Figure 5.5 shows the same-event distribution (filled circles) and the normalized mixed-event background distribution (open squares) for nine p_t bins at mid-rapidity ($|y| < 0.5$) for the 11% most central events while Figure 5.6 shows the invariant mass distribution for the 26–85% centrality bin. In situations where the signal to background ratio is high and the background distribution is relatively flat, it is possible to obtain reasonable results by fitting the background distribution to a polynomial, and extracting the resonance peak. A situation, however, may arise where the resonance sits right at the point where the entire invariant mass distribution peaks. In this case, it is very difficult to estimate the exact shape of the background under the peak, which may change the estimated resonance production by as much as 60% (see Reference 1 in [DFN84]).

For STAR, we see that the the situation is complicated by acceptance effects. Since the acceptance for kaon pairs varies with the transverse momentum of the pair, the shape of the total invariant mass distribution varies with p_t (Figures 5.5 and 5.6). By

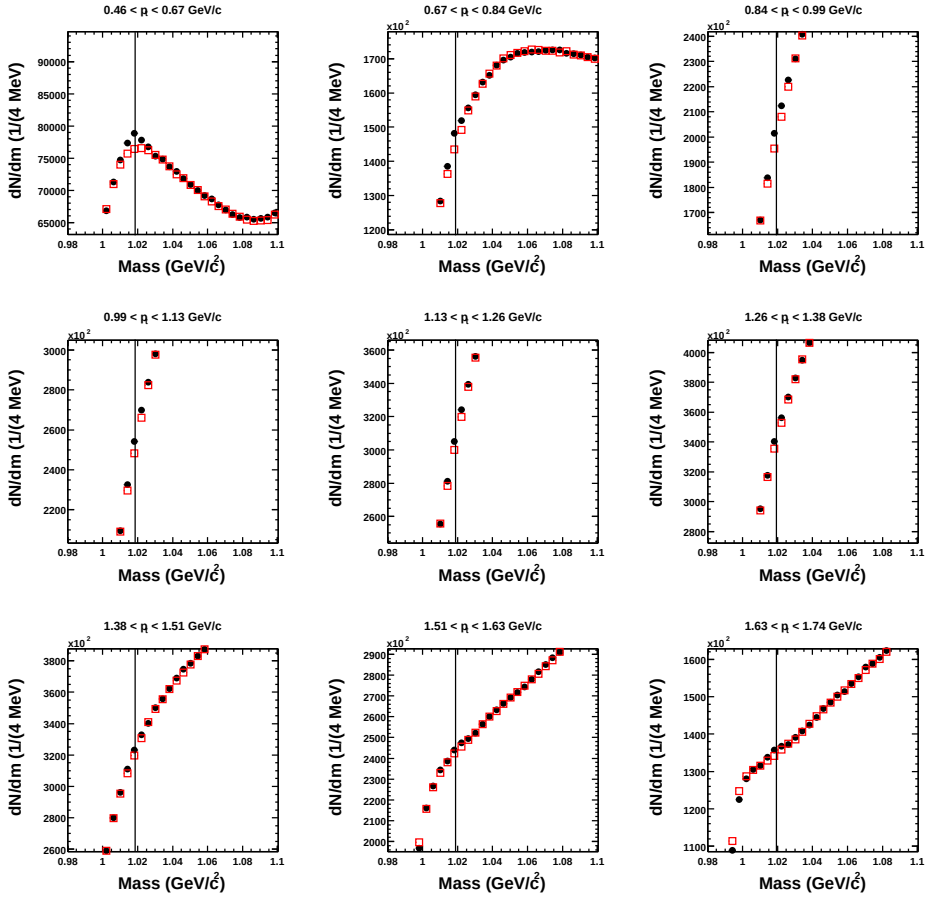

Figure 5.5: Invariant mass distribution for nine p_t bins at mid-rapidity ($|y| < 0.5$) for the 11% most central events. Filled circles are the data-points from the same-event distribution and the open squares are the data-points from the normalized mixed-event distribution. For clarity, the maximum and minimum were set to 120% and 80% of the bin content in the ϕ mass region. The vertical line marks the PDG [GG00] mass for the ϕ meson. The errors on the points are smaller than the size of the markers.

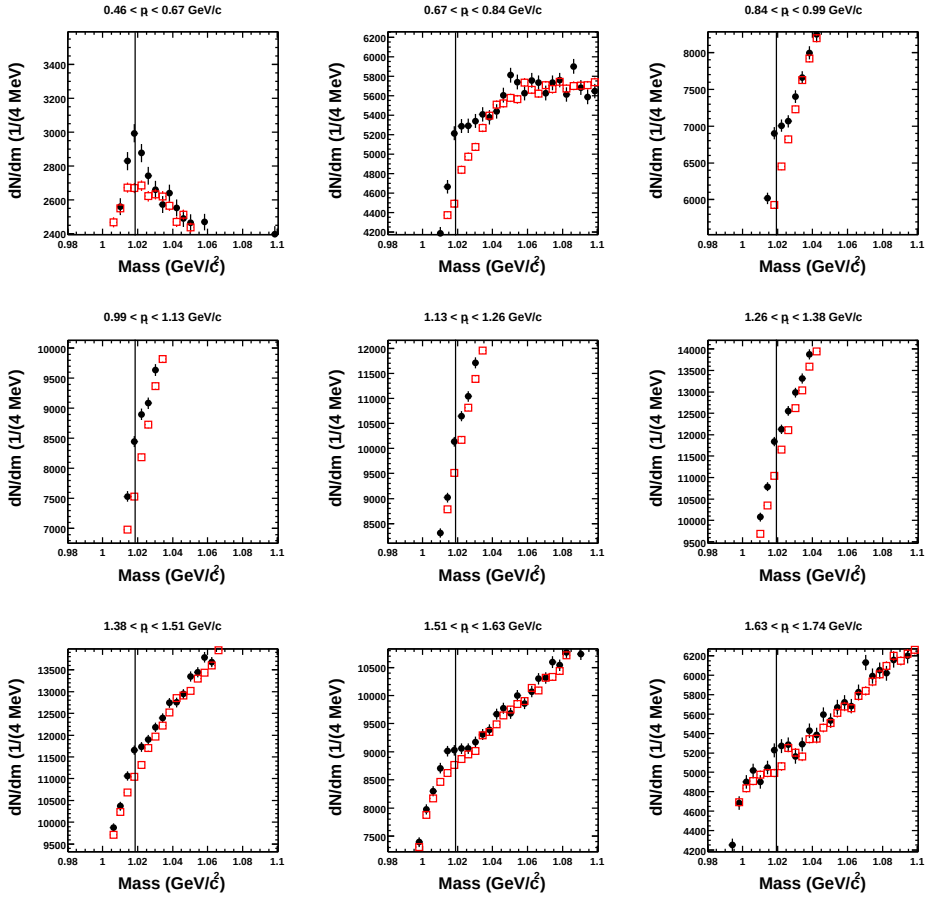

Figure 5.6: Invariant mass distribution for nine p_t bins at mid-rapidity ($|y| < 0.5$) for the 26–85% centrality bin. Filled circles are the data-points from the same-event distribution and the open squares are the data-points from the normalized mixed-event distribution. For clarity, the maximum and minimum were set to 120% and 80% of the bin content in the ϕ mass region. The vertical line marks the PDG [GG00] mass for the ϕ meson. Error bars shown are statistical errors only.

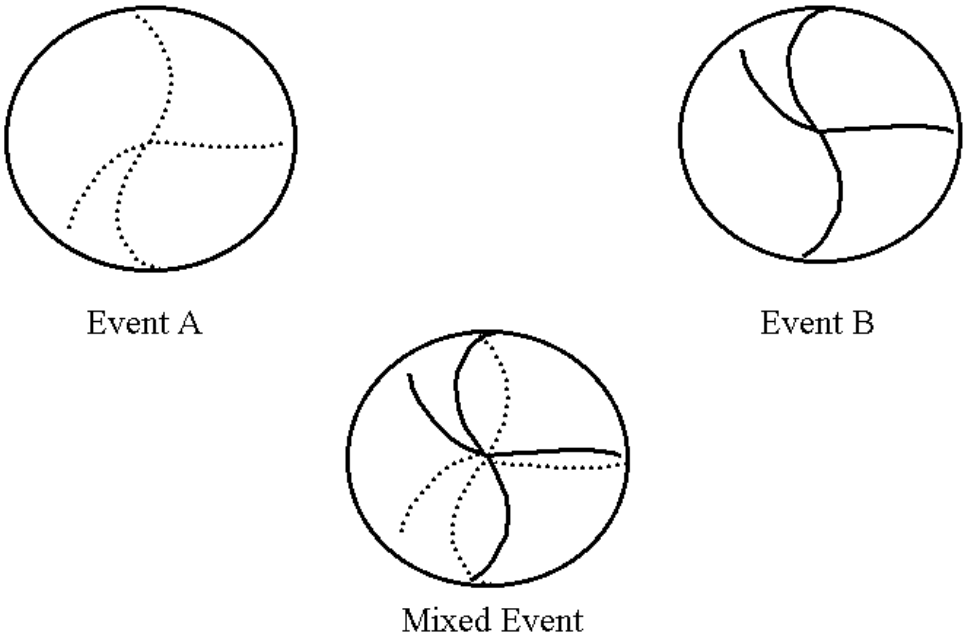

Figure 5.7: Diagram of the event mixing technique. Positive tracks are taken from Event A and negative tracks are taken from Event B. The tracks are then combined into one event and all combinations of positive and negative tracks in the mixed-event are calculated.

using tracks from different events for the background calculation, we approximately preserve the event-by-event single particle phase space distribution, which is the dominant factor in determining the shape of the background distribution. In this way, we minimize the systematic uncertainty from the background calculation, particularly in situations where the peak of the total invariant mass distribution coincides with the resonance peak position.

In the final analysis, each event used in calculating the same-event distribution was used in the mixed-event background calculation. In order to improve the statistics of the background, each event was mixed with two other events. The mixing was done by employing a First-In-First-Out (FIFO) buffer with N elements. When a new event was selected, the events in the FIFO were shifted up one element, and the new event placed in the lowest element of the FIFO. This new event was then mixed with all the other events in the FIFO. An event in the last element of the FIFO was deleted.

5.5.2 Residual Correlations

The majority of the background in the K^+K^- invariant mass distribution originates from uncorrelated pairs which are reproduced in the event mixing method. The correlations, however, in the same-event distribution are never fully removed by event mixing [Zaj84], and there remain residual correlations in the invariant mass distribution.

It is obvious that if the same-event sample contains a strong correlation such as a prominent, sharp peak in the invariant mass distribution from the decay of a resonance, then some artifact of this correlation may be preserved in the mixed-event spectra. For the case in which a subset of the same-event pairs come from a resonance, the single particle phase space distributions of the secondary particles may be different from the single particle momentum distributions of the same species in the uncorrelated background. The mixed-event distribution will therefore have multiple contributions: contributions from mixed-event pairs where both pairs are from the background, from pairs in which one partner is from the background and the other is from a resonance, and from pairs in which both partners are from different resonances. In fact, since the same-event distribution is filled with all possible pairings, including pairings in which one pair partner comes from a resonance and the other comes from the background, some effect similar to the residual correlations must be present even in the same-event spectra. The effect of the separate contributions is examined in detail L'Hote [LH94]. In general, the smaller the experimental acceptance, the more the correlation in the same-event distribution is preserved in the mixed-event distribution. It has nevertheless been demonstrated that the effect of the residual correlations is always present, even for an experiment with a 4π acceptance, regardless of the origin of the correlations.

Other sources of extraneous correlations include effects from momentum conservation, like-particle correlations, Coulomb interaction between particles, other reso-

nances, γ conversions to e^+e^- in detector material and detector effects such as acceptance variations and track merging.

Presumably, in central $Au+Au$ collisions at RHIC, the constraints of global energy and momentum conservation do not introduce a significant correlation to the momenta of individual particles. The presence of other resonances due to mistaken PID hypothesis (i.e. $\rho \to \pi^+\pi^-$ and $K^0_s \to \pi^+\pi^-$) has been studied. In light of the statistical analyzing power of the data-set from the first year of running, these resonances are not a source of concern for this analysis. The Coulomb attraction between K^+ and K^- pairs is observed right above the two kaon mass threshold in the K^+K^- invariant mass distribution.

Due to difficulties in completely separating kaons from electrons and positrons using dE/dx, it is possible that correlated electron-positron pairs from γ conversions in detector material may appear in the K^+K^- invariant mass distribution. Since the relative invariant momentum of the e^+e^- pair from γ conversions is small, this correlation will appear as a residual background near the two kaon mass threshold.

The STAR TPC was designed to be symmetric about the center of the interaction region. Variations in the acceptance occur since the collision vertex position may vary considerably event-by-event. This variation in the collision vertex position translates into a non-statistical variation in the single particle inclusive momentum distribution. This non-statistical variation will lead to a mismatch between the mixed-event and same-event invariant mass distributions which may prevent the extraction of the signal. By binning the events according to their primary z position and performing event mixing only with events within the same vertex bin, it is possible to minimize this effect.

A final source of residual correlations which was of concern for this analysis was the effect of detector resolution on the invariant mass distribution. Track merging

occurs for two high momentum tracks with low relative momentum (q). The sagitta of these tracks is of the order of the electron cluster size (about 3 cm). This effect places a constraint on the lowest measurable q for higher momentum kaon pairs. Track merging results in a dip at low invariant mass, which increases with increasing pair momentum.

Due to the difficulties inherent in describing the low mass background, the invariant mass region below the ϕ meson mass was excluded in the normalization of the mixed-event background distribution.

5.6 Extracting Spectra

The ϕ spectra for the various centralities was extracted by subtracting out the normalized mixed-event background from the same-event distribution. The normalization and subtraction is done in each $p_t - y$ or $m_t - y$ bin. Figure 5.8 shows the background subtracted invariant mass distribution (subtracting the normalized mixed-event distribution (open squares) from the same-event distribution (filled circles) in Figure 5.5) in nine p_t bins, where $|y| < 0.5$ for the 11% most central events. Figure 5.9 is the background subtracted invariant mass distribution in $|y| < 0.5$ and $0.46 < p_t < 1.74$ GeV/c from the 11% most central data while Figure 5.10 is from the 26–85% centrality bin.

The background subtracted invariant mass distribution in each bin was then fit to a Breit-Wigner function plus a background function (Equation 5.1),

$$\frac{1}{2000\,\pi}\frac{A\Gamma}{(m-m_0)^2+\Gamma^2/4}+B \tag{5.1}$$

$\Gamma =$ Full Width Half Maximum (FWHM)

$A =$ Area of Breit-Wigner

$m_0 =$ Resonance position

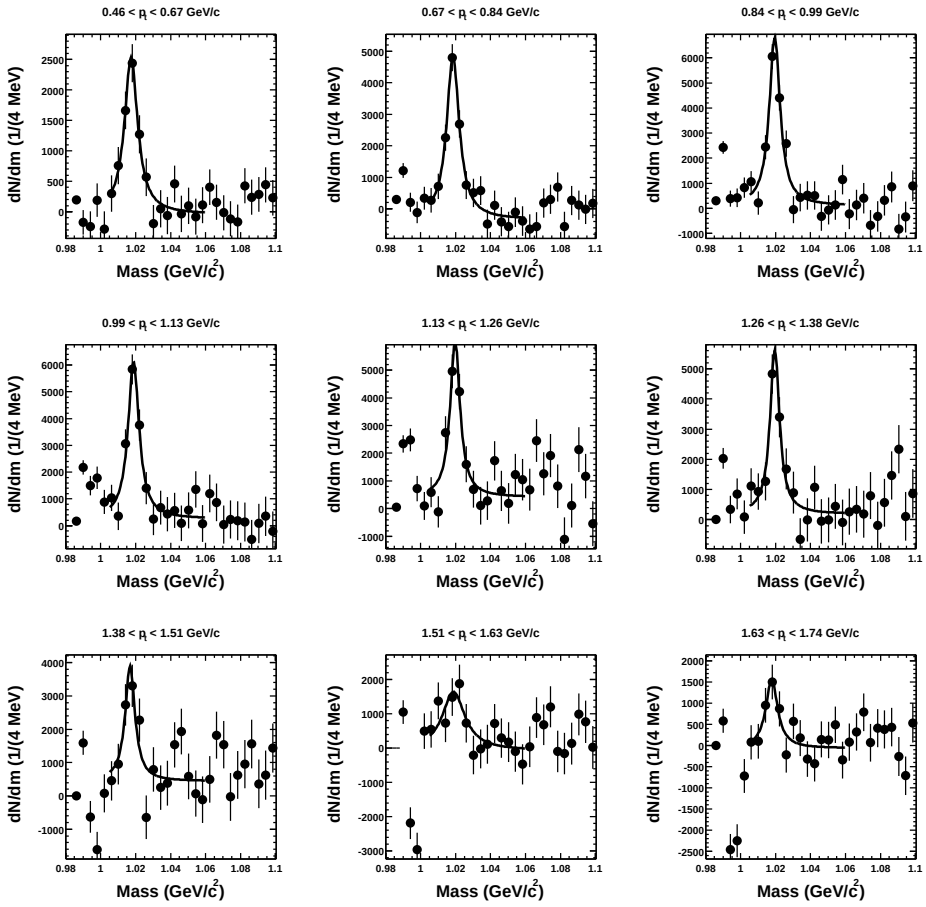

Figure 5.8: Background subtracted invariant mass distribution for K^+K^- pairs from central events for nine $m_t - y$ bins at mid-rapidity, $|y| < 0.5$. The line through the data-points is to guide the eye. Error bars shown are statistical errors only.

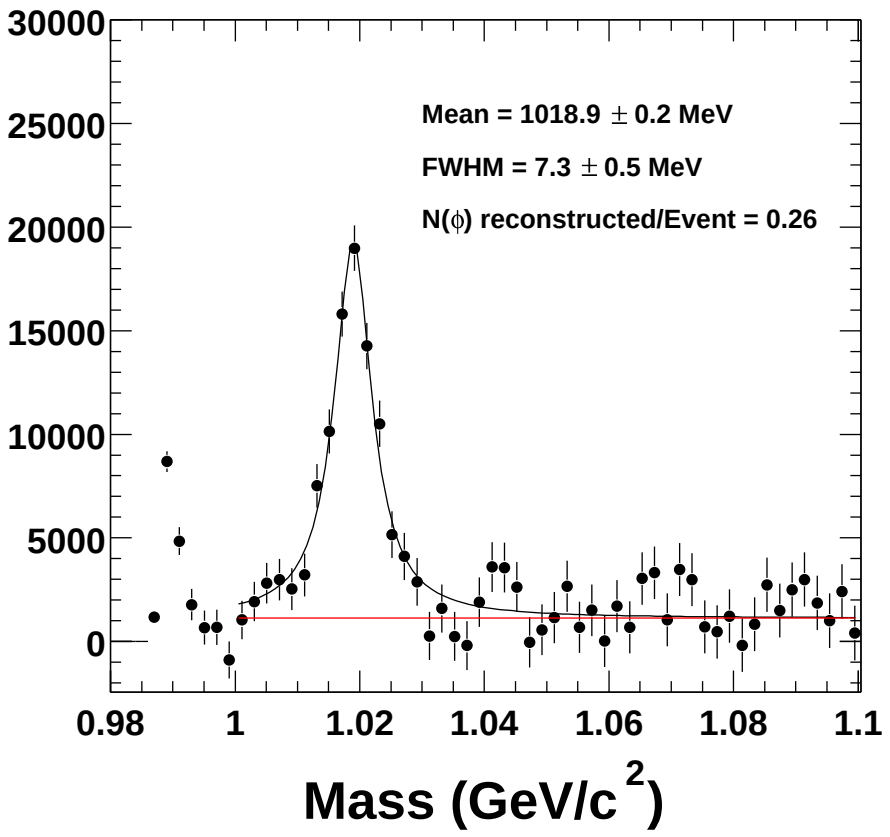

Figure 5.9: Background subtracted invariant mass distribution for K^+K^- pairs from the 11% most central events at mid-rapidity, $|y| < 0.5$ and $0.46 < p_t < 1.74$ GeV/c. Error bars shown are statistical errors only.

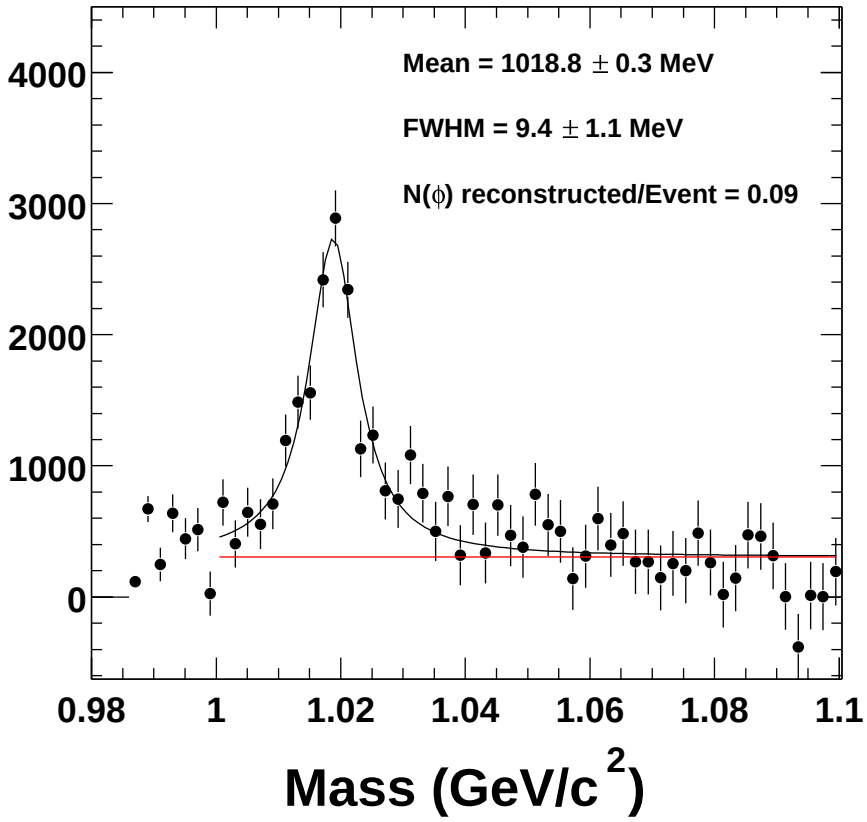

Figure 5.10: Background subtracted invariant mass distribution for K^+K^- pairs from the 26–85% centrality bin at mid-rapidity, $|y| < 0.5$ and $0.46 < p_t < 1.74$ GeV/c. Error bars shown are statistical errors only.

$B =$ Background

where A is the area, Γ is the width (FWHM) in GeV of the Breit-Wigner function, m_0 is the resonance position in GeV and B is the background hypothesis. Note that the yield (A), m_0 and Γ were free parameters in the fit. It was necessary to include a residual background hypothesis to the fit of the invariant mass distribution for reasons described in Section 5.5.2.

Contributions to the residual background included e^+e^- pairs from γ conversions and track merging, backgrounds which are not reproducible in event mixing. The effects from e^+e^- pairs from γ conversions are apparent in the $0.99 < p_t < 1.13$ GeV/c and $1.13 < p_t < 1.26$ GeV/c bins (bins 4 and 5 in Figure 5.8) as a residual background near the two kaon mass threshold. This is due to the difficulty of separating the electron/positrons from kaons using dE/dx. Between a single particle momentum of $0.5 < p < 0.6$ GeV/c, the kaons and electron/positrons are indistinguishable using dE/dx PID. As a result, mis-identified e^+e^- conversion pairs with low relative momentum are reconstructed as a low mass background. Since this real correlation is not accounted for in event mixing, extra care was taken in fitting the invariant mass distributions in these two bins to account for the contamination from e^+e^- conversion pairs. Track merging, as discussed in Section 5.5.2, manifests itself as a dip in the invariant mass distributions for the high p_t bins (bins 7 – 9 in Figure 5.8). Figures 5.11, 5.12 and 5.13 are the raw invariant spectra extracted for low multiplicity, mid-central, and central events in the rapidity interval $|y| < 0.5$.

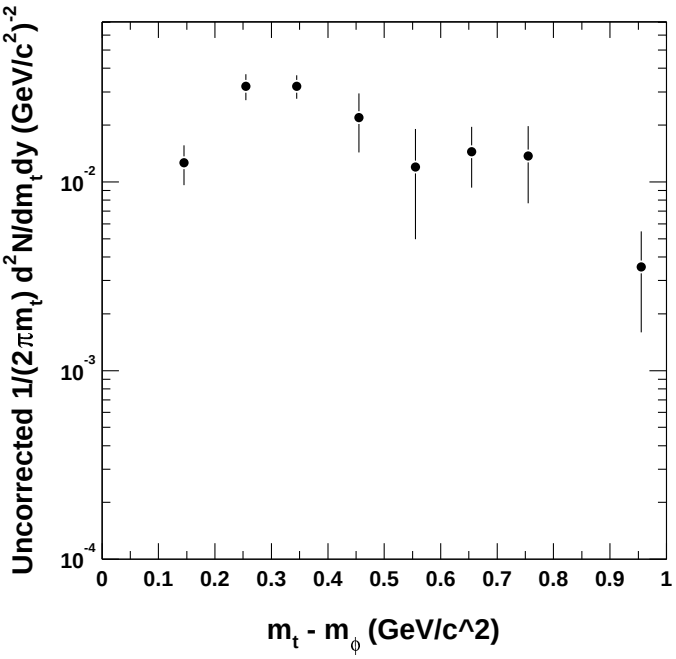

Figure 5.11: Uncorrected ϕ meson invariant multiplicity vs. transverse mass distribution for low multiplicity events. Error bars shown are statistical errors only.

5.7 Efficiency Correction

The simulation programs GSTAR and TRS were used to correct the raw invariant multiplicity distributions for detector acceptance, response, and tracking efficiency effects. Simulated ϕ mesons were generated using a flat $p_t - y$ distribution and passed through GSTAR and TRS. The ϕ mesons were then decayed by GEANT 100% to the $\phi \rightarrow K^+ + K^-$ decay channel.

The output of TRS, which simulated the TPC response at the pixel level, was then combined with the raw data. The combination of real and simulated data were then passed through the standard STAR reconstruction chain. After reconstruction of the complete event, the Monte-Carlo tracks were correlated to reconstructed tracks using

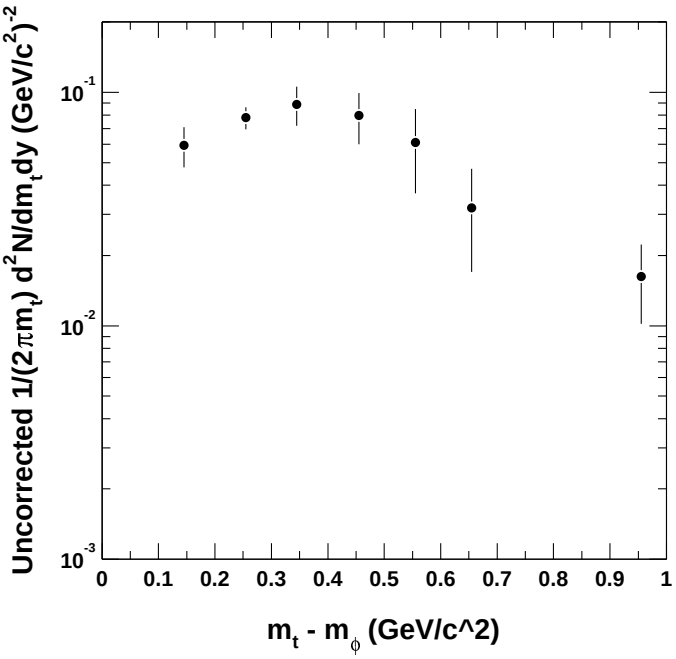

Figure 5.12: Uncorrected ϕ meson invariant multiplicity vs. transverse mass distribution for mid-central events. Error bars shown are statistical errors only.

STAR standard code. The process of correlating the Monte-Carlo information and the reconstructed information is referred to as "Association". The Monte-Carlo track and the reconstructed track information is associated, and the tracking efficiency and detector acceptance for ϕ mesons decaying to K^+K^- pairs is calculated. For each ϕ meson decaying to a K^+K^- pair, the off-line cuts were applied to the daughter kaons, and the efficiency for ϕ meson reconstruction was determined simply by comparing the input ϕ meson distribution with the distribution of ϕ mesons which had both daughter kaons pass the off-line track selection criteria. Since the kinematic quantities for every possible permutation of selected K^+ and K^- tracks are calculated, the only criteria necessary for determining the reconstructability of the ϕ meson is that both daughters are accepted into the candidate kaon track pool. The only requirement when associ-

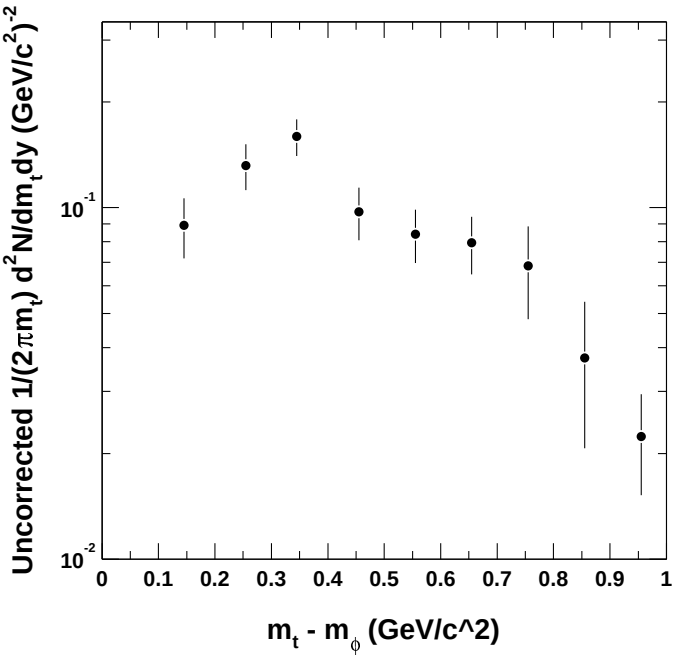

Figure 5.13: Uncorrected ϕ meson invariant multiplicity vs. transverse mass distribution for central events. Error bars shown are statistical errors only.

ating the Monte-Carlo track with the reconstructed track was that the number of hits common to both the Monte-Carlo and reconstructed tracks be at least 3 hits. All candidate associations were then stored in a ROOT [BR97] TTree.[1] The TTree with the Monte-Carlo information was then used to study the stability of the Monte-Carlo correction against the cuts used for the signal extraction from real data. By varying cuts in the Monte-Carlo, the cuts were optimized to be insensitive to the simulation while maximizing the signal.

[1]The row-wise and column-wise ntuples have been one of the major strengths of the PAW package [Div99]. Trees extend the concept of ntuples to all complex objects and data structures found on raw data tapes and DST's. The idea is that the same data model, same language, same style of queries can be used on all data sets in an experiment. Trees are designed to support not only complex objects, but also a very large number of them in a large number of files. Ntuples are simple trees with one branch only.

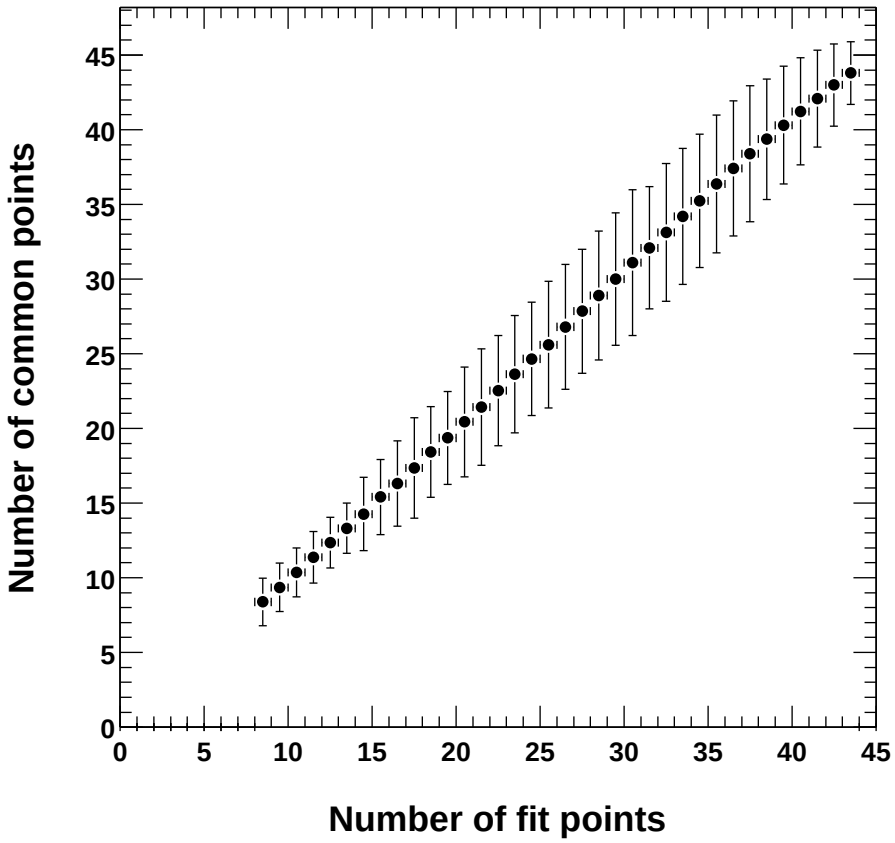

Figure 5.14: Number of common hits vs. number of fit points used to reconstruct the track. The error bars are 3σ error bars from a gaussian fit to the distribution of number of common hits for each value of the number of fit points.

The Monte-Carlo association efficiency was also studied. Figure 5.14 shows the correlation between the common hits requirement when associating tracks and the off-line number of fit points requirement applied to real data. It was determined that the final result would be insensitive to association inefficiency as long as the number of common hits requirement were five fewer than the number of fit points requirement for the off-line data.

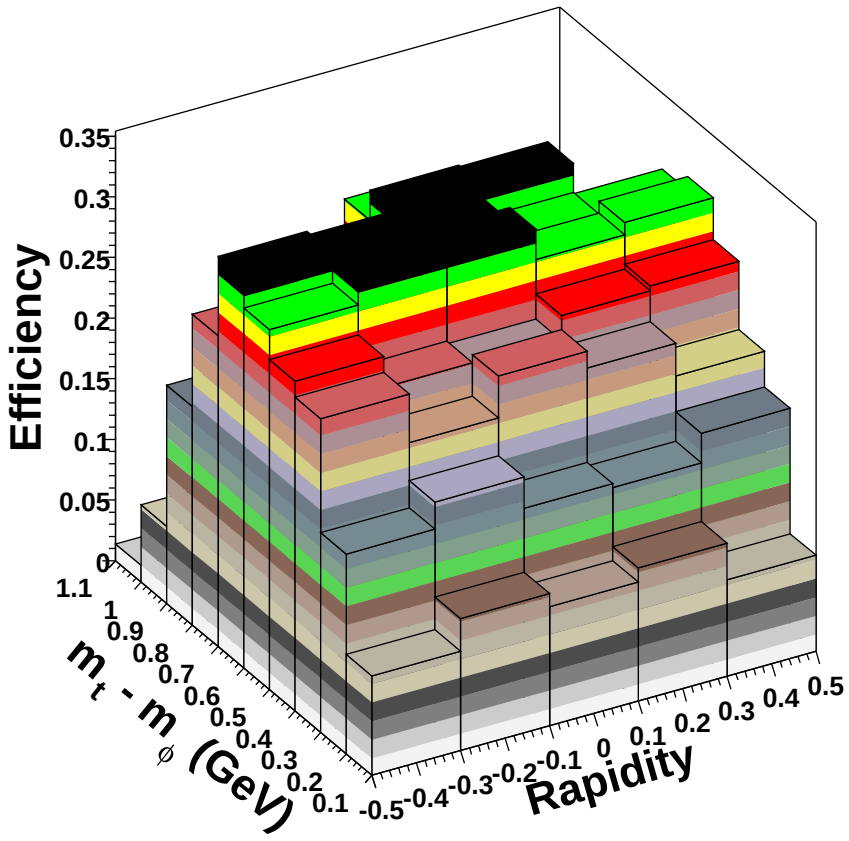

Figure 5.15: Efficiency for ϕ meson reconstruction vs. $m_t - m_\phi$ and rapidity for minimum-bias events. The efficiency shown here includes the detector acceptance and tracking efficiency.

Figure 5.15 shows the efficiency for ϕ meson reconstruction vs. $m_t - m_\phi$ and rapidity for minimum-bias events. The efficiency shown here includes the detector ac-

ceptance and tracking efficiency.

5.8 PID Efficiency Correction

Centrality Bin	Characteristic $\langle dE/dx \rangle$ width (δ)
0–11%	0.5855
11–26%	0.5541
26–85%	0.5272
STAR Standard	0.45

Table 5.4: Measured characteristic $\langle dE/dx \rangle$ resolution for the three centrality bins used in this analysis. The characteristic $\langle dE/dx \rangle$ width, δ, is the width associated with a gaussian distribution. The STAR standard resolution was determined by Calderon [Cal00] while the resolution values applied to this analysis were measured by Tang [Tan01]

The PID efficiency correction for the ϕ meson (ε_ϕ) was calculated by determining the K^+ (ε_{K^+}) and K^- (ε_{K^-}) PID efficiency corrections. The PID resolution for K^+ and K^- particles are identical and the efficiencies ε_{K^+} and ε_{K^-} were calculated by determining the fraction of kaons accepted with a given cut according to the normal error integral (Equation 5.2).

Table 5.4 shows the characteristic $\langle dE/dx \rangle$ width, δ, for the three centrality bins used in this analysis. Initial estimates of δ performed by Calderon [Cal00] proved to be inadequate to obtain the proper normalizations. A more detailed analysis of the $\langle dE/dx \rangle$ resolution performed by Tang [Tan01] provided the necessary precision to obtain reasonable PID corrections. The resolution degrades with increasing event multiplicity, which can qualitatively be understood as being related to the difficulty in track reconstruction as the hit density increases in the detector. Figure 5.16 shows the dependence of the $\langle dE/dx \rangle$ resolution as a function of the number of dE/dx points ($N_{dE/dx}$) used to calculate the mean dE/dx. The resolution is proportional to $1/\sqrt{N_{dE/dx}}$, and

for the majority of tracks, the $\langle dE/dx \rangle$ resolution was about 10–15%.

$$\varepsilon_{K^{\pm}} = erf\left(\frac{n \cdot \delta_{STAR}}{\delta_R \sqrt{2}}\right) \tag{5.2}$$

$$\varepsilon_{\phi} = \varepsilon_{K^+} \cdot \varepsilon_{K^-} \tag{5.3}$$

$\varepsilon_i =$ Efficiency for particle i

$\delta_R =$ Measured characteristic $\langle dE/dx \rangle$ width

$\delta_{STAR} =$ STAR software $\langle dE/dx \rangle$ width

$erf =$ Normal error integral

$n =$ Number of sigma cut

The ϕ PID efficiency, ε_{ϕ}, is the product of ε_{K^+} and ε_{K^-} (Equation 5.3) and provides an overall normalization factor to the final yield. The shape of the transverse mass distribution remains unchanged.

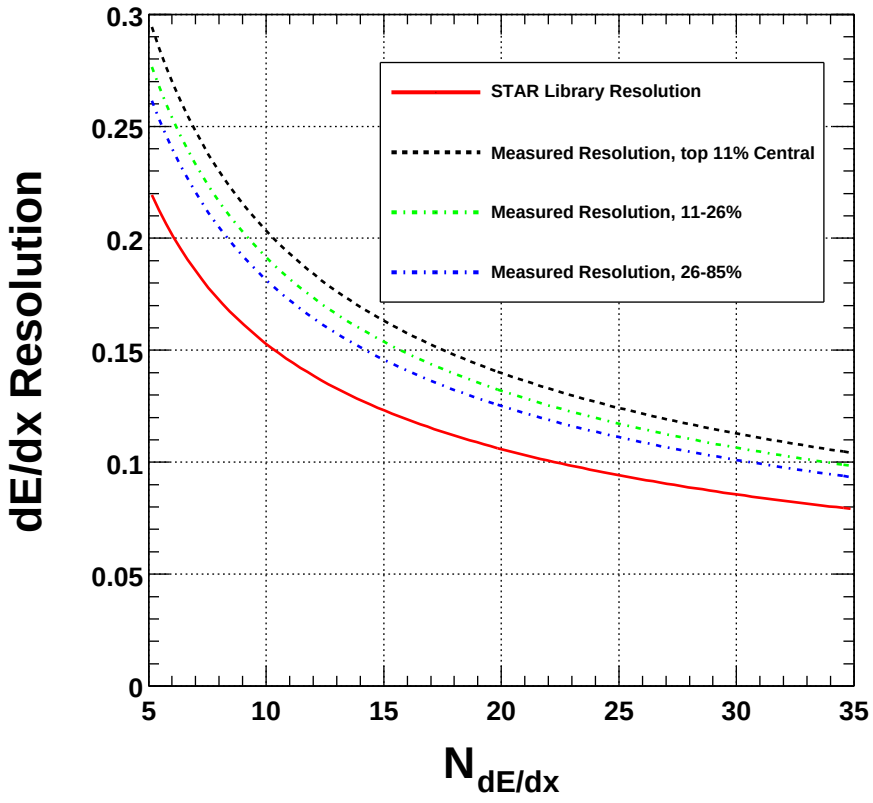

Figure 5.16: $\langle dE/dx \rangle$ resolution vs. number of space points used in the truncated mean dE/dx calculation. The resolution is proportional to $1/\sqrt{N_{dE/dx}}$, and the $\langle dE/dx \rangle$ resolution for typical tracks in the TPC was about 10–15%.

CHAPTER 6

Results

6.1 Widths of the Invariant Mass Distributions

The widths of the invariant mass distributions in each $m_t - y$ bin were studied. Of particular interest is the idea that chiral symmetry restoration would manifest itself as modifications to the properties of the ϕ meson [HK94, LS91]. The TPC was studied using Monte-Carlo ϕ mesons embedded into real events.

Figure 6.1 shows the mass resolution as a function of p_t at mid-rapidity in central events. The mass resolution distribution in each p_t bin was fit to a Breit-Wigner function to extract a width to determine the characteristic mass resolution in each bin. Table 6.1 lists the measured mass width of the ϕ for each p_t bin for the most central data and the corresponding detector mass resolutions. Figure 6.2 shows the width of the ϕ meson as a function of $m_t - m_\phi$ after de-convolution of the detector resolution estimated from the Monte-Carlo. The mass resolution was included as a constrained parameter in the fit to the invariant mass distribution. A limit was set at one sigma for the maximum allowable variation of the resolution parameter in the fit. Although we cannot exclude a mass broadening for the ϕ mesons from the K^+K^- decay channel, with our current statistics, the width the ϕ mesons measured in this analysis are consistent with the width quoted in the PDG [GG00] ($\Gamma = 4.41$ MeV/c^2).

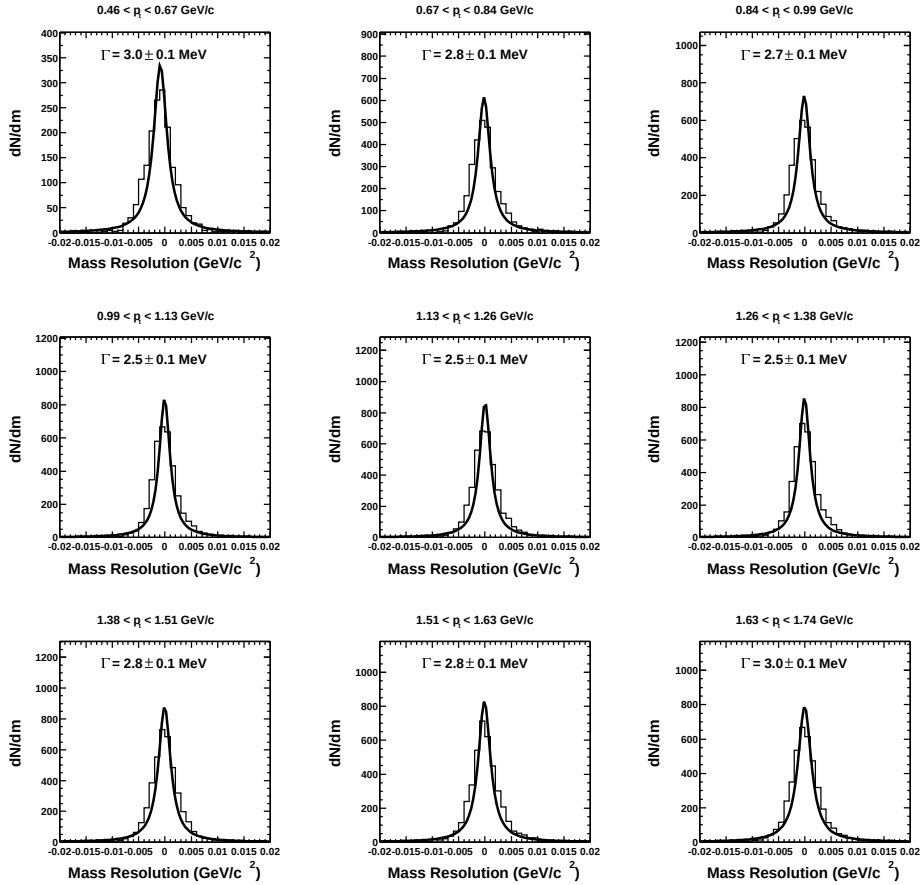

Figure 6.1: ϕ mass resolution determined from embedding in central events. The mass difference between the input to the Monte-Carlo and the output after simulation and reconstruction is shown for nine $p_t - y$ bins. The distributions were fit to a Breit-Wigner function to determine Γ. The measured widths in Figure 5.8 are consistent with the natural width of the ϕ ($\Gamma = 4.41$ MeV$/c^2$) convoluted with the simulated detector resolution.

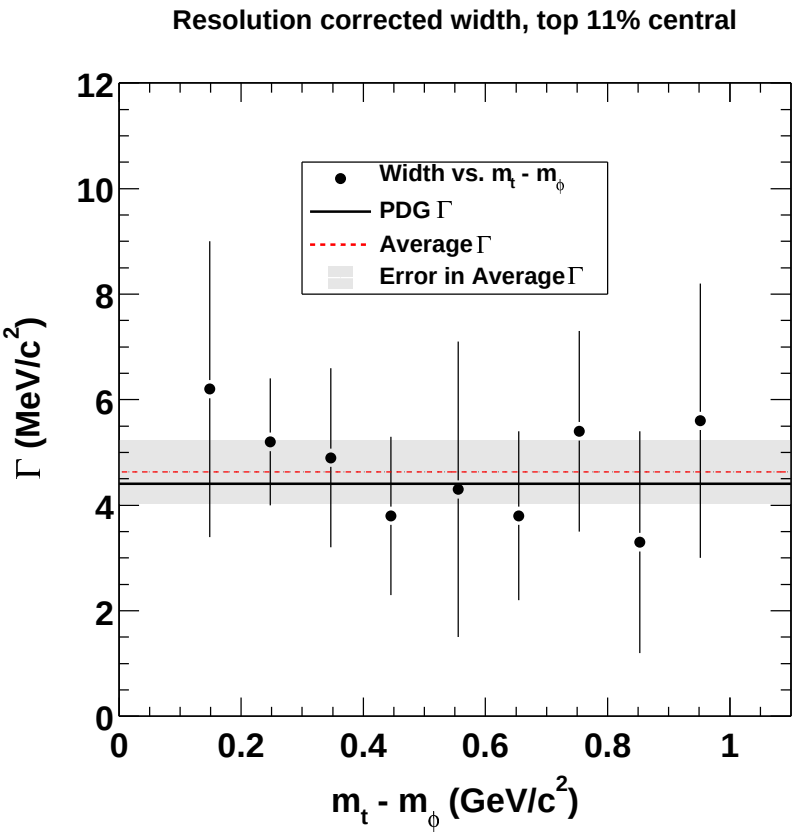

Figure 6.2: FWHM vs. $m_t - m_\phi$ for central events after de-convolution of the detector resolution from the ϕ mass distribution. The line is a fit to the points and has a value of $\Gamma_{Fitted} = 4.6 \pm 0.6\ \mathrm{MeV/c^2}$. The widths of the invariant mass distributions are consistent with the natural width quoted from the PDG. Error bars shown are statistical errors only.

$m_t - m_\phi (\mathrm{GeV}/c^2)$	Γ (MeV/c^2)	Γ_R (MeV/c^2)	Γ (De-convoluted)
0.10–0.20	9.1 ± 1.9	3.0 ± 0.1	6.2 ± 2.8
0.20–0.30	7.6 ± 1.2	2.8 ± 0.1	5.2 ± 1.2
0.30–0.40	8.3 ± 1.2	2.7 ± 0.1	4.9 ± 1.7
0.40–0.50	6.1 ± 1.3	2.5 ± 0.1	3.8 ± 1.5
0.50–0.60	5.2 ± 1.2	2.5 ± 0.1	4.3 ± 2.8
0.60–0.70	6.3 ± 1.4	2.5 ± 0.1	3.8 ± 1.6
0.70–0.80	7.9 ± 2.8	2.8 ± 0.1	5.4 ± 1.9
0.80–0.90	7.4 ± 4.9	2.8 ± 0.1	3.3 ± 2.1
0.90–1.00	7.2 ± 2.3	3.0 ± 0.1	5.6 ± 2.6

Table 6.1: Measured mass widths (Γ) and resolution (Γ_R) in nine m_t bins for central events. Results show that after correction for detector resolution, the widths are compatible with the accepted ϕ width, with a mean value for Γ de-convoluted of 4.6 ± 0.6 MeV/c^2 (Figure 6.2). Errors listed are statistical errors only.

$m_t - m_\phi$ (GeV/c^2)	0–11%	11–26%	26–85%
0.10–0.20	1.157 ± 0.225	0.786 ± 0.162	0.131 ± 0.032
0.20–0.30	0.891 ± 0.132	0.558 ± 0.067	0.205 ± 0.033
0.30–0.40	0.822 ± 0.098	0.506 ± 0.099	0.133 ± 0.019
0.40–0.50	0.441 ± 0.075	0.374 ± 0.094	0.089 ± 0.031
0.50–0.60	0.345 ± 0.059	0.234 ± 0.092	0.041 ± 0.024
0.60–0.70	0.317 ± 0.059	0.128 ± 0.060	0.046 ± 0.017
0.70–0.80	0.284 ± 0.084	0.000 ± 0.000	0.049 ± 0.022
0.80–0.90	0.195 ± 0.087	0.000 ± 0.000	0.000 ± 0.000
0.90–1.00	0.194 ± 0.062	0.149 ± 0.057	0.026 ± 0.015

Table 6.2: Invariant yield in each $m_t - m_\phi$ bin for three event centralities. Errors listed are statistical errors only.

6.2 Transverse Mass Distributions

The results of the analysis were plotted as the invariant multiplicity vs. transverse mass ($\frac{1}{2\pi m_t}\frac{d^2N}{dm_t dy}$ vs. $m_t - m_\phi$) for three centrality bins in Figure 6.3. Table 6.2 lists the value and statistical error for each data point in Figure 6.3. In the region where the pion band crosses the kaon band in dE/dx, corresponding to the kaon $p_t \simeq 0.80$ GeV/c, the signal to background ratio degrades. This leads to the larger statistical error bars in the most central bin and prevented the extraction of meaningful ϕ yields in this region for

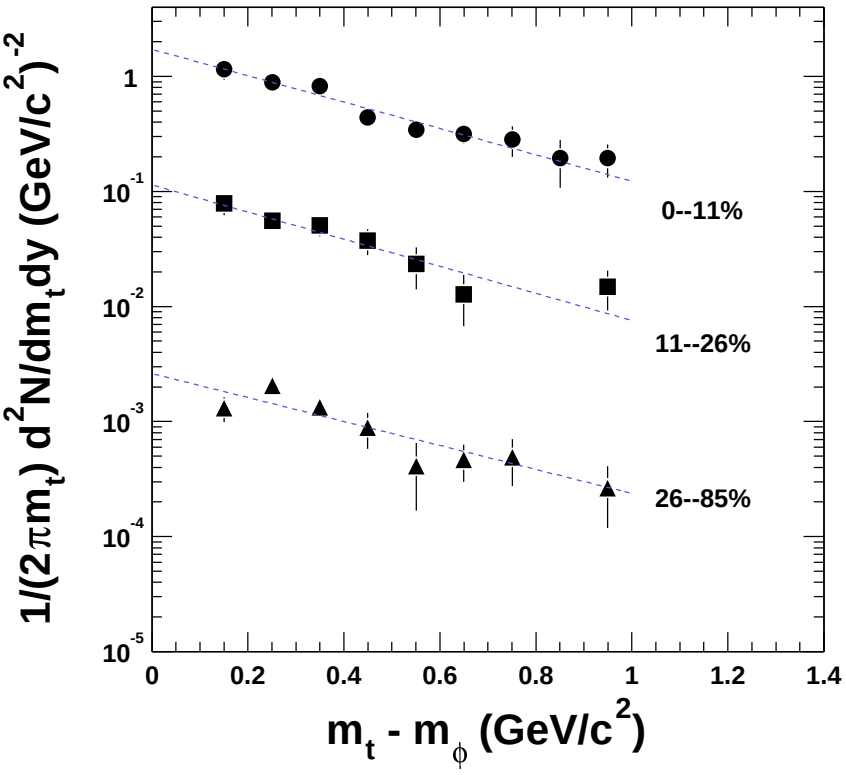

Figure 6.3: Transverse mass distributions of mid-rapidity ϕ mesons for three centrality bins. Invariant yields are shown dashed lines represent exponential fits to the data. Data points from the 11–26% bin were scaled by 0.1 and data points from the 26–85% bin were scaled by 0.01. Error bars shown are statistical errors only.

the two lower multiplicity bins.

6.3 Fits to the Transverse Mass Distributions

The transverse mass distributions were fit to Equation 6.1

$$\frac{1}{2\pi m_t}\frac{d^2N}{dm_t dy} = \frac{1}{2\pi} A\, e^{-(m_t - m_0)/T} \tag{6.1}$$

and the slope parameter T extracted. The rapidity density, dN/dy at mid-rapidity, was extracted by integrating the fit to the measured transverse mass distribution (Equation 6.1). By integrating both sides of Equation 6.1, we get an analytic expression relating dN/dy to the transverse mass parameters:

$$\begin{aligned}
\int_{m_0}^{\infty} m_t dm_t \frac{1}{2\pi m_t}\frac{d^2N}{dm_t dy} &= \int_{m_0}^{\infty} m_t dm_t A\, e^{-(m_t-m_0)/T} \\
u &= (m_t - m_0)/T \\
du &= dm_t/T \\
\frac{dN}{dy} &= AT \int_0^{\infty} du(uT + m_0)e^{-u} \\
&\vdots \\
\frac{dN}{dy} &= AT(m_0 + T)
\end{aligned} \tag{6.2}$$

Combining Equations 6.1 and 6.2 gives Equation 6.3, which is the fit function used for the results presented here. dN/dy and T were free parameters in the fit. Note that the dN/dy returned by the fit represents an extrapolation over full phase-space. From the fitted slope parameters, the fraction of ϕ mesons in the measured m_t region, assuming an exponential distribution is $\sim 70\%$. The results of the fits to the invariant multiplicity distributions in the three centrality bins is shown in Table 6.3. Figure 6.4 shows the slope parameters for three centrality bins. While the yield increases with centrality as one would expect, there seems to be no dependence of the slope parameter on collision centrality.

$$\frac{1}{2\pi m_t}\frac{d^2N}{dm_t dy} = \frac{dN/dy}{2\pi T(m_\phi + T)} e^{-(m_t - m_\phi)/T} \tag{6.3}$$

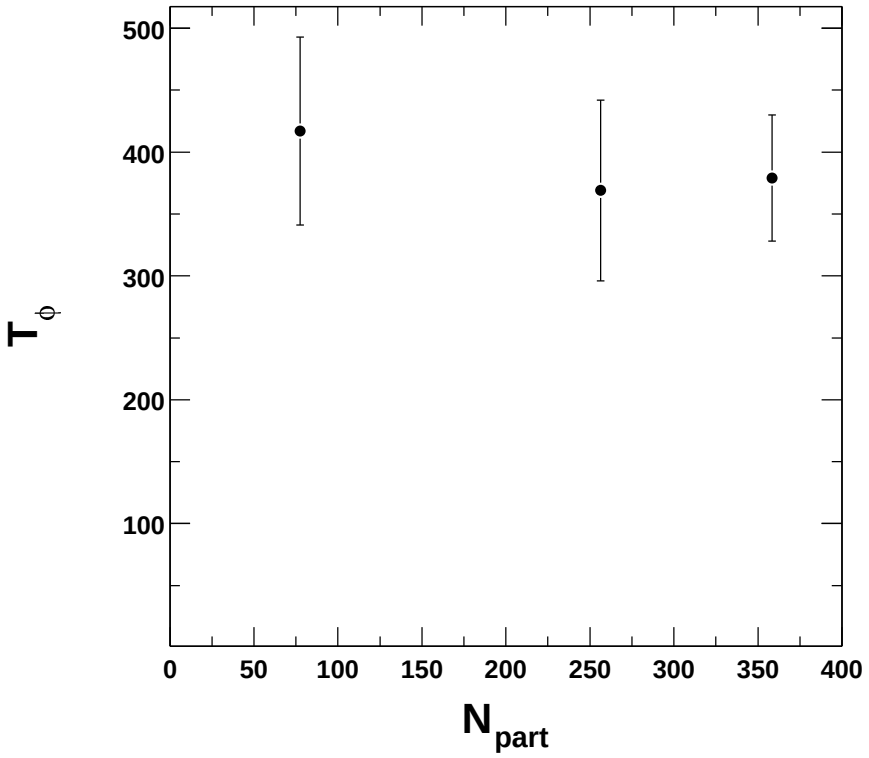

Figure 6.4: The ϕ slope parameter for three centrality bins. Error bars shown are statistical errors only.

6.4 Particle Ratios

6.4.1 Calculation of h^- and N_{part}

In order to make meaningful comparisons to data from other experiments, it is necessary to characterize a set of events with an observable quantity common to all experiments. A reasonable choice is the mean N_{ch} for a set of events, or the negatively charged hadron multiplicity (h^-) for the events. In $p+A$ and $A+A$ collisions, it

Event Centrality	0–11%	11–26%	26–85%
T(MeV)	379 ± 51	369 ± 73	417 ± 76
$dN/dy_{\|y\|<0.5}$	5.73 ± 0.37	3.33 ± 0.38	0.98 ± 0.12
N_ϕ/N_{h^-}	0.021 ± 0.001	0.019 ± 0.002	0.019 ± 0.002
N_ϕ/N_{K^-}	0.14 ± 0.01	0.12 ± 0.02	0.14 ± 0.02

Table 6.3: Mid-rapidity ϕ slope parameters and extrapolated dN/dy for three centrality bins. Centrality is denoted as the fraction of the measured cross-section with 0% corresponding to the most central events. The values for dN/dy reflect a correction for trigger bias, which is discussed briefly in Section 6.4.1. Although the ratios N_ϕ/N_{h^-} and N_ϕ/N_{K^-} have yet to be discussed, they are also listed for convenient reference. Errors listed are statistical errors only.

is also desirable to measure the number of nucleons that participate in the collision (N_{part}). This number may be inferred by using the h^- value in conjunction with model calculations. The convention is to use the measured h^- when comparing results from different experiments.

Historically, laboratory experiments have always used incoming projectiles with a net charge ≥ 0 (e.g. $e^+ + e^-$, $p + \bar{p}$, $p + p$, $p + A$ and $A + A$). A description of an event should be independent of the total charge of the incoming projectiles. Negatively charged hadrons, being free of projectile particles, offer the cleanest description of the event. The N_{part} value is determined from the h^- value for this reason.

It is possible to relate the N_{ch} multiplicity distribution within a pseudo-rapidity interval $|\eta| < 0.75$ to the negatively charged hadron multiplicity and the number of participants (N_{part}). The h^- distribution [Adl01b] for each centrality bin is determined using a look-up table by first converting the N_{ch} number to an uncorrected h^- value and then the uncorrected h^- value to a corrected h^- value for negative hadrons with a $p_t > 0.10$ GeV/c [CX01a]. An extrapolation to $p_t = 0$ GeV/c introduces an overall normalization increase of 7%. Figure 6.5 shows the relation between h^- and N_{ch}.

Although the h^- distribution gives a good indication of the relative centrality of an event sample from a specific collision system and energy, it is desirable to find a

common scaling to compare results from other experiments studying different collision systems at various energies. A common practice to allow this comparison is to define centrality by the number of participants (N_{part}). The number of participants describes the number of incoming projectile nucleons that participated in the collision. The number of participants scaling used was determined by Chen and Xu [CX01b] and follows the power law in Equation 6.4.

$$\langle h^- \rangle = 0.4042 \langle N_{part} \rangle^{1.097} \tag{6.4}$$

Table 6.4 lists the values of h^- and N_{part} for each centrality bin. There are two sets of values for the mid-central bin, 5-6 and 5-6*. The mid-central data-set is a mixture of data taken with both a minimum-bias and a central trigger. There is an inherent trigger bias in the mid-central bin due to the use of data taken with two different triggers. The values listed in 5-6* are the raw values of h^- and N_{part} for the biased data-set. The values listed in 5-6 represent a scaling to make the values representative of a minimum-bias data-set.

Flow Bins	h^- ($p_t > 0.10$ GeV/c)	h^- (Extrapolated)	N_{part}
1-4	47	50	77
5-6*	176	189	256
5-6	160	171	235
7-8	254	272	358

Table 6.4: The values of h^- and the number of participants for the three centrality bins. There are two sets of values for the mid-central bin, 5-6 and 5-6*, as discussed in the text.

The extrapolated dN/dy listed in Table 6.3 are corrected for the trigger bias caused by using events taken with the minimum-bias and central trigger. The correction for trigger bias is necessary for comparisons to models. The models assume a minimum-bias distribution and need comparisons to data-sets commensurate with this assumption. The yield dN/dy is scaled assuming the ϕ yield increases uniformly with the

negative hadron multiplicity. Inherent in this scaling is the assumption that there is no centrality dependence of the relative yield of ϕ mesons. The N_ϕ/N_{h^-} ratio should be constant when using this assumption. Section 6.4.2 describes the results for the N_ϕ/N_{h^-} ratio and it is clear that within the statistics available, this assumption is reasonable.

6.4.2 The Ratios N_ϕ/N_{h^-}, N_ϕ/N_{K^-} and N_ϕ/N_{part}

The particle ratios N_ϕ/N_{h^-}, N_ϕ/N_{K^-} and N_ϕ/N_{part} have been calculated as a function of centrality in this analysis. Figure 6.6 shows the results N_ϕ/N_{h^-} vs. N_{part}. At this energy, ϕ production seems to scale linearly with the number of particles produced. The N_ϕ/N_{K^-} ratio (Figure 6.7) is also independent of centrality. This indicates that ϕ meson production at this energy increases correspondingly with the overall increase in strangeness production. The N_ϕ/N_{part} ratio (Figure 6.8) seems to increase as a function of centrality. This is expected from the N_ϕ/N_{h^-} ratio. Since N_{part} is derived from h^- and they are related by Equation 6.4, if the N_ϕ/N_{h^-} ratio is truly flat, the N_ϕ/N_{part} ratio must increase with increasing centrality. Unfortunately, any statement on a trend in these results is tenuous at best: the analysis is statistics limited and will require further investigation.

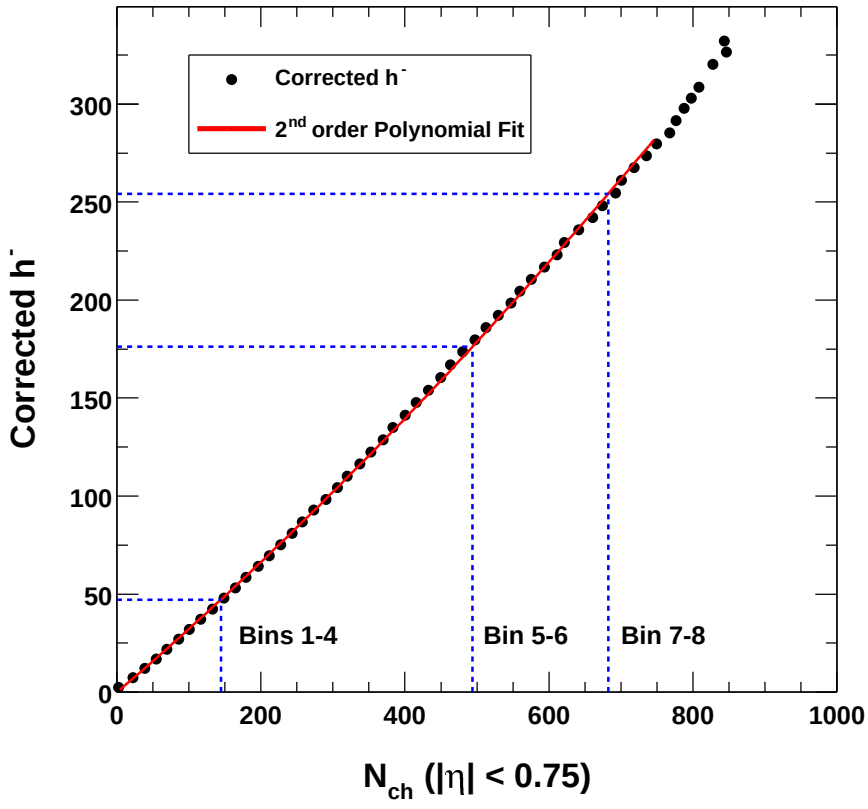

Figure 6.5: Plot of the corrected h^- for $p_t > 0.10$ GeV/c vs. measured N_{ch} within a pseudo-rapidity interval $|\eta| < 0.75$. The line through the data-points is a second order polynomial fit to the data. The dashed lines represent the N_{ch} and h^- values for the three centrality bins used in this analysis. The extrapolation to full phase space ($p_t = 0$ GeV/c) increases the h^- yield by 7%.

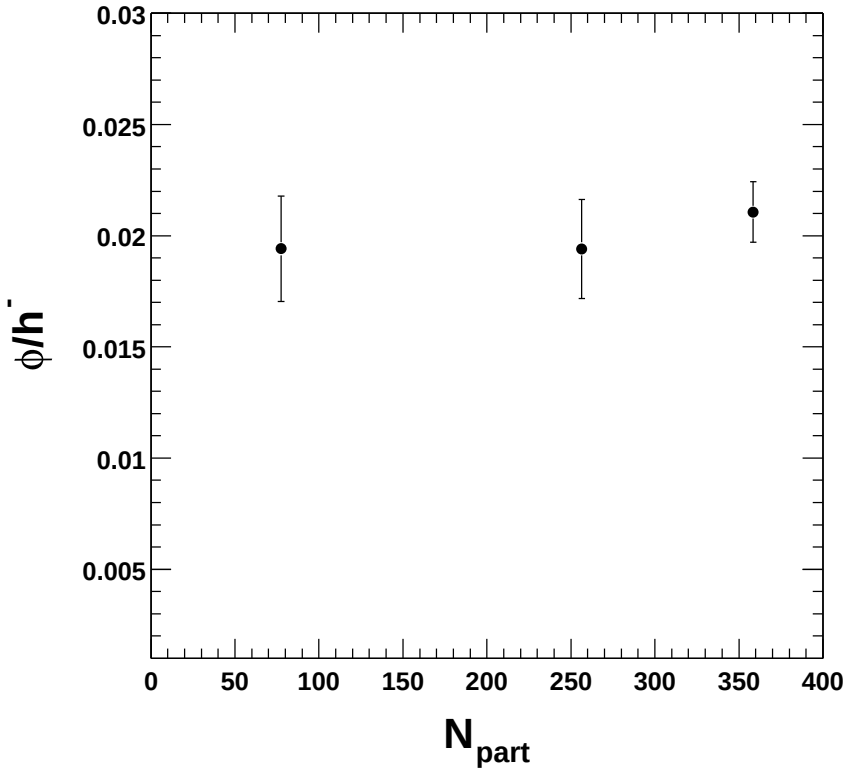

Figure 6.6: N_{ϕ}/N_{h^-} ratio vs. N_{part}. Error bars shown are statistical errors only.

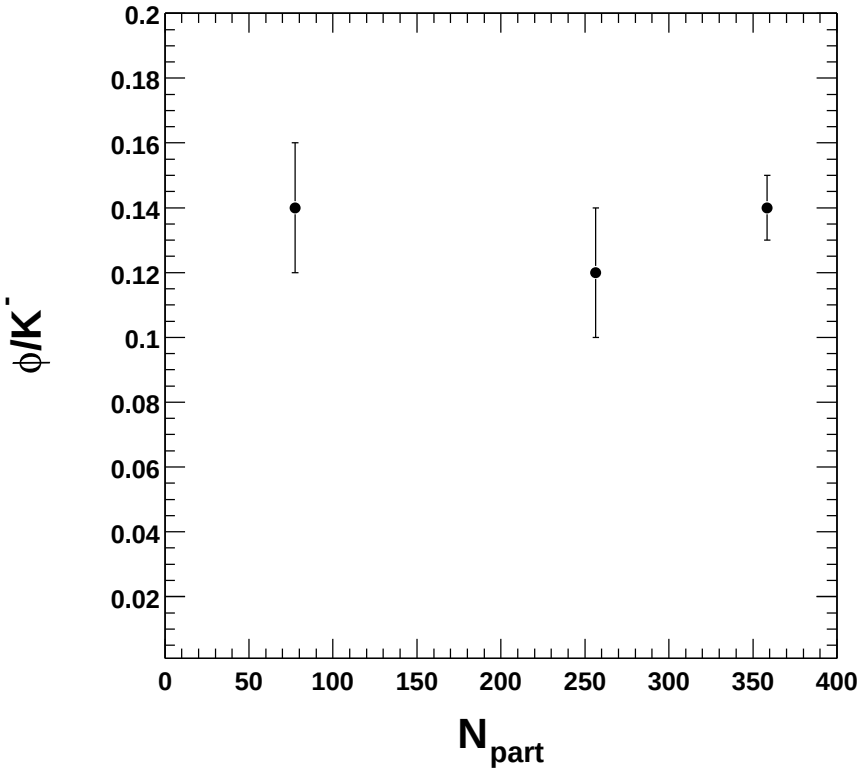

Figure 6.7: N_{ϕ}/N_{K^-} ratio vs. N_{part}. Error bars shown are statistical errors only.

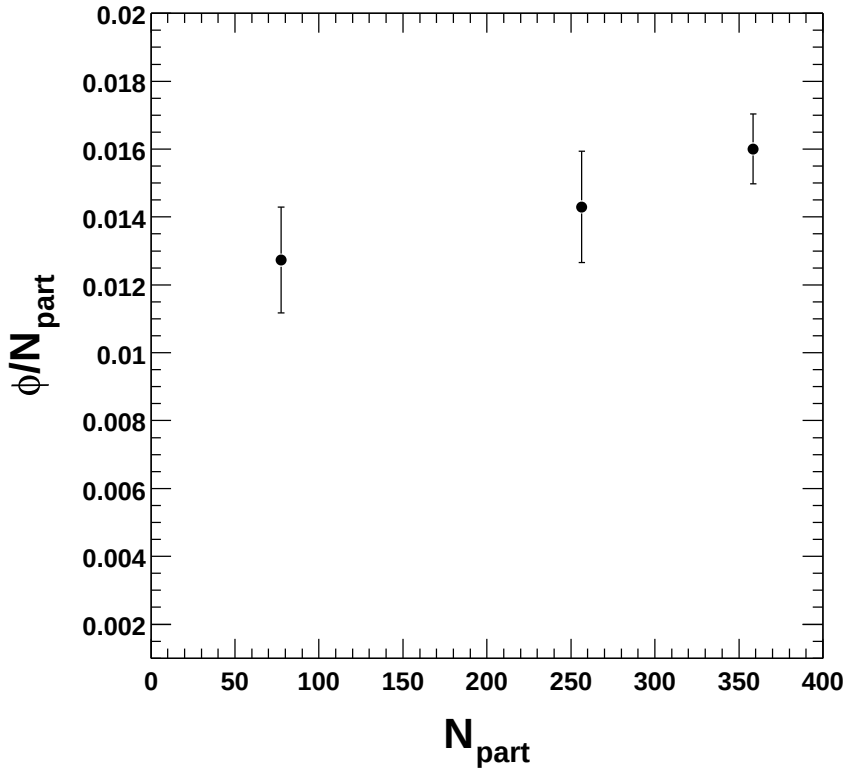

Figure 6.8: N_{ϕ}/N_{part} ratio vs. N_{part}. Error bars shown are statistical errors only.

CHAPTER 7

Systematic Uncertainties

For this analysis, I have attempted to place an upper limit on the systematic uncertainty. The study of systematic uncertainties was limited due to the relatively low statistics available. While the best effort was made to describe these uncertainties, the study is limited by the statistical precision of the measurement. By studying the effects of variations in the cuts used, the full range of the systematic uncertainty is estimated to be $\pm 12\%$ for T and $\pm 10\%$ for dN/dy. Systematic errors on the ratios are larger due to the uncertainties associated with the h^- and K^- yields. The full range of the systematic uncertainty is $\pm 20\%$ for N_ϕ/N_{h^-} and $\pm 25\%$ for N_ϕ/N_{K^-}.

7.1 Efficiency Calculation

Systematic uncertainties due the Monte-Carlo simulation have been studied. The uncertainties lie in the inability of the Monte-Carlo to completely describe the detector response. To estimate the possible systematic uncertainties due to slight mis-matches between the Monte-Carlo data and the real data, the off-line cuts used in the analysis were varied and the corrected ϕ meson distribution, fitted yields and slopes were studied. The event vertex selection cuts listed in Table 5.1 as well as the track quality and kinematic cuts in Table 5.3 were varied and the variations in the fitted yields and slope parameters due to the cuts are quoted as systematic uncertainties.

7.2 Particle Identification

The ϕ analysis is dependent on particle identification (PID). Since the multiplicity in a single $Au+Au$ event is so large, the combinatorial background is overwhelming. By applying a PID cut, we reduce the low momentum pion contamination, which is the dominant source of combinatorial background.

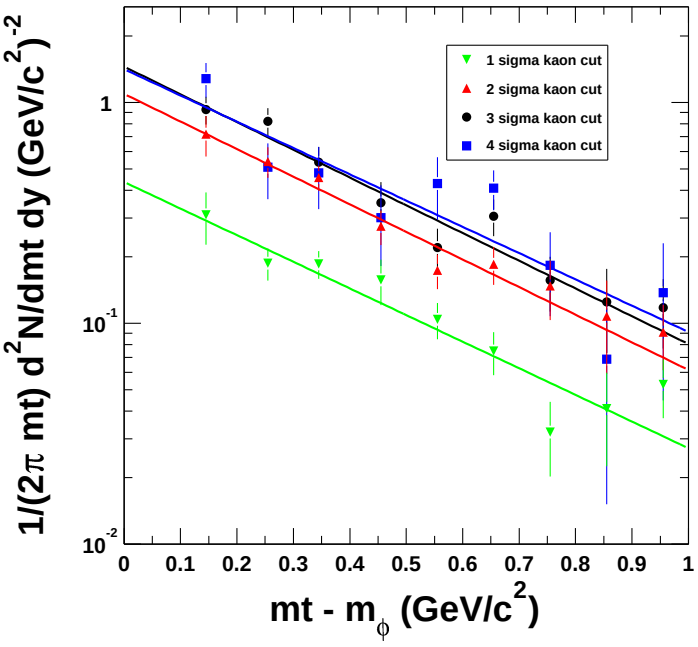

Figure 7.1: Transverse mass distributions from the 11% most central events. The distributions shown were extracted by applying four different PID cuts to the data: 1, 2, 3 and 4 σ_k. The distributions were corrected for acceptance and tracking efficiency. Error bars shown are statistical errors only.

The major concern for this analysis has been the possibility of a momentum dependence of the PID cut. This was a concern since this would directly affect T_ϕ. To study the possibility of a momentum dependence in the PID cut, we ran through the data with four different PID cuts of 1, 2, 3 and 4 σ_k. The results from these four cuts

after tracking efficiency and acceptance corrections are shown in Figure 7.1. The variation in T vs. PID cut (Figure 7.3) and dN/dy vs. PID cut (Figure 7.4) was found to be much smaller than the statistical uncertainty. The slope and yield from 4 σ_K have larger statistical uncertainties than the 3 σ_K data points because more background is added while very little additional signal is gained.

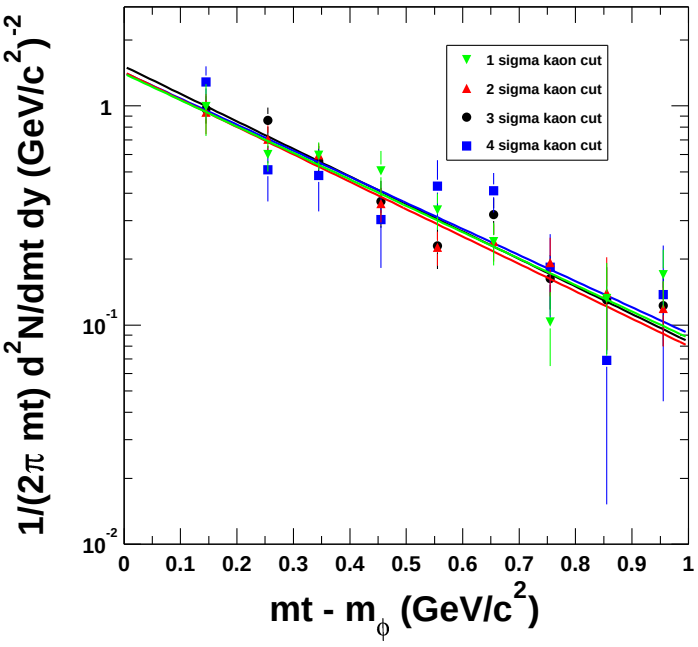

Figure 7.2: Transverse mass distributions from the 11% most central events. The distributions shown were extracted by applying four different PID cuts to the data: 1, 2, 3 and 4 σ_k. The distributions were corrected for acceptance, tracking efficiency and PID efficiency. Error bars shown are statistical errors only.

7.3 Event Mixing

Due to the low statistics and relatively high signal to noise ratio for this analysis, the systematics from the event mixing background was deemed small. To estimate

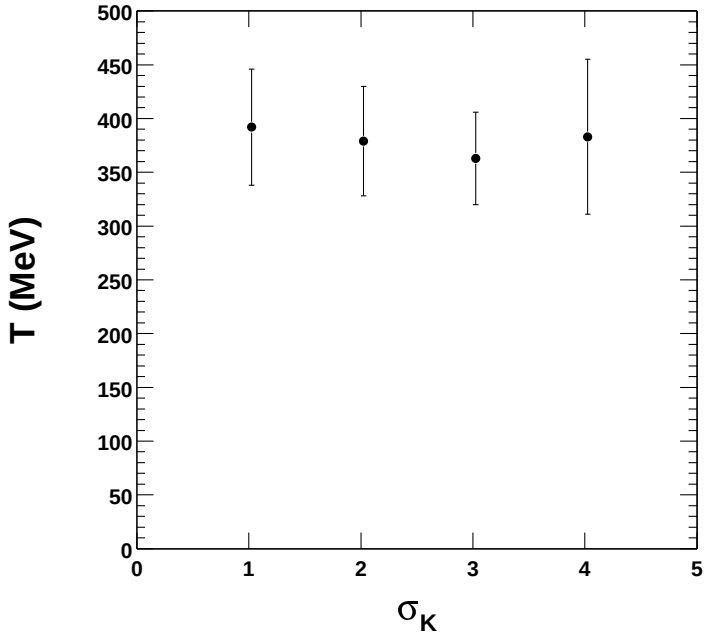

Figure 7.3: T_ϕ from the 11% most central events using four different PID cuts: 1, 2, 3 and 4 σ_k. Error bars shown are statistical errors only.

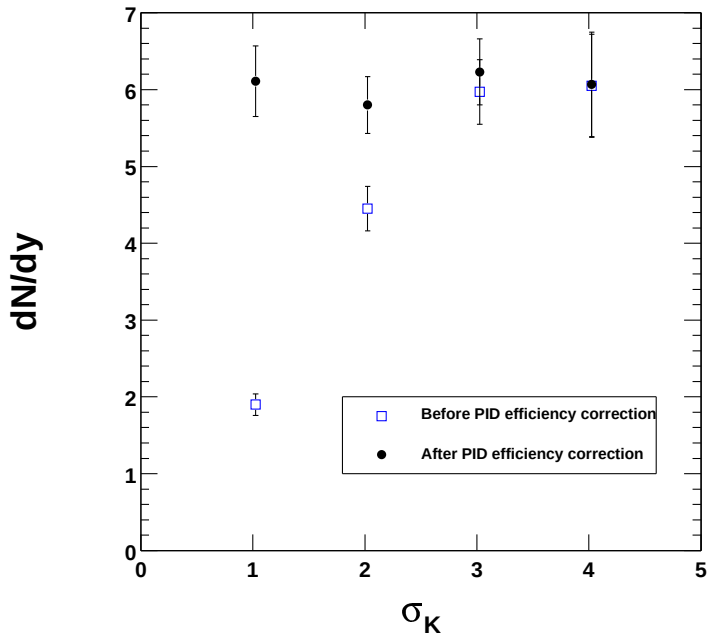

Figure 7.4: Extrapolated dN/dy from the 11% most central events after applying four different PID cuts to the data: 1, 2, 3 and 4 σ_k. Open boxes are extrapolated dN/dy before PID efficiency correction and filled circles are dN/dy after all corrections are applied. Error bars shown are statistical errors only.

the uncertainty from the event mixing, several background hypothesis were used in an attempt to describe the residual background present in the background subtracted invariant mass distribution (Section 5.5.2). The background hypotheses were: constant, linear, second order polynomial and exponential. For the analysis done here, the constant and linear background hypotheses proved adequate to describe the major features of the residual background. The differences between yields obtained from various background hypotheses were within the statistical uncertainty of the measurement.

CHAPTER 8

Discussion

8.1 ϕ Meson Production

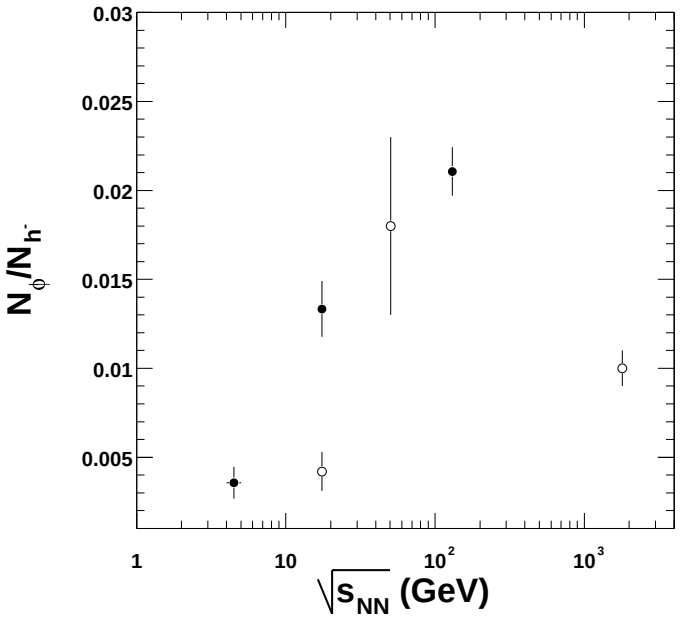

Figure 8.1: N_ϕ/N_{h^-} ratio vs. $\sqrt{s_{NN}}$ for approximately the 10% most central heavy ion collisions (filled circles), $p+p$ and $p+\bar{p}$ collisions (open circles). Error bars shown are statistical errors only.

In heavy ion collisions, we see an increasing trend for both strangeness production and ϕ meson production. The N_ϕ/N_{h^-} ratio increases from the AGS ($\sqrt{s_{NN}} = 4.9$ GeV)

to the SPS ($\sqrt{s_{NN}} = 17.2$ GeV) to RHIC ($\sqrt{s_{NN}} = 130$ GeV) (Figure 8.1). On the other hand, there is no energy dependence in the N_ϕ/N_{K^-} ratio (Figure 8.2) for both heavy ion collisions and $p+p$ collisions from the AGS to RHIC. The ratio N_ϕ/N_{K^-} is also about 0.1 for $p+\bar{p}$ collisions at the Tevatron [Ale93, Ale95].

The suggestion that kaon coalescence may contribute significantly to ϕ meson yields in heavy ion collisions was originally based on the similarity of the ϕ meson distribution to the product of the K^+ and K^- rapidity distributions. In its simplest form, the coalescence model suggests that the probability of forming a ϕ meson from kaons in heavy ion collisions is proportional to the number of $K\bar{K}$ pairs per unit volume in the collision region (Equation 8.1).

$$N_\phi \propto \frac{N_K N_{\bar{K}}}{V} \tag{8.1}$$

Under the assumption that $V \propto N_{part}$, an observation that $N_\phi/N_{K^+K^-}$ is inversely proportional to $\langle N_{part} \rangle$ would be consistent with the hypothesis that kaon coalescence contributes significantly to ϕ meson production. Results from STAR presented at Quark Matter 2001 [Har01] indicate that the K^+/K^- ratio is independent of both centrality and p_t. With the K^+/K^- ratio and the results for the ϕ/K^-, we can infer that Equation 8.1 is effectively:

$$N_\phi \propto \frac{N_{K^-} N_{K^-}}{V} \tag{8.2}$$

As mentioned in Section 2.3.1, Baltz and Dover performed an analysis of ϕ meson production in $Si+Au$ collisions at the AGS. Their estimates of ϕ meson production were two orders of magnitude lower than what has been measured [Col95, Wan94, Mou01]. Using the coalescence model, the AGS E917 experiment [Bac00] also performed essentially an identical analysis for $Au+Au$ collisions and also found that the coalescence model under-predicts their fiducial ϕ meson yield by a factor of 10.

The ratio N_ϕ/N_{K^-} is observed to be relatively constant with N_{part} (from comparisons of $Pb+Pb$, $Au+Au$, $p+p$, and $p+\bar{p}$ collisions) for all energies. Although the flat N_ϕ/N_{K^-} ratio that we measure vs. centrality at RHIC would be in qualitative agreement with the trend expected in a simple coalescence model (i.e. $1/V \propto 1/N_{part}$), it seems improbable that similar relative particle compositions would be observed in $p+p$, $p+\bar{p}$ and heavy ion collisions at energies spanning three orders of magnitude if the production mechanisms were fundamentally different. Furthermore, as seen in Figure 8.3, the kaon slope parameter is relatively close to the ϕ slope parameter. In a kaon coalescence model, one would expect that the momentum of the ϕ should be $p_\phi \simeq \sum_i p_i$, where p_i is the momentum of the kaons which coalesce to form the ϕ. One would expect T_ϕ to be about twice as large as T_K, which is not the case at RHIC. The ϕ/K^- ratio would therefore seem to indicate that the probability of s and $\bar{s}$ quark hadronization into K^- and ϕ mesons is independent of collision energy and system size, and that ϕ mesons are most likely not produced from coalescence. Furthermore, as discussed in the next section, the spectra of the ϕ meson deviates from a spectra expected from a coalescence model. Higher statistics would be desirable for a detailed study of the centrality dependence of ϕ meson production.

8.2 Dynamical Properties of the ϕ Meson at RHIC

Figure 8.3 shows the preliminary results of T vs. mass for π^-, K^-, $\bar{p}$, ϕ, Λ and Ξ^- from STAR. In the highest multiplicity $Au+Au$ collisions at RHIC, the ϕ slope parameter is 379 $\pm$ 51 (stat) $\pm$ 45 (syst) and there is no dependence on event centrality (Table 6.3) within our statistical uncertainty. The preliminary number for the STAR measurement of the anti-proton slope parameter, however, measured in the p_t range $0.25 < p_t < 1$ GeV/c and without correction for feed-down from anti-hyperons, is found to be over 150 MeV higher than the ϕ meson slope measured in $0.5 < p_t < 1.7$

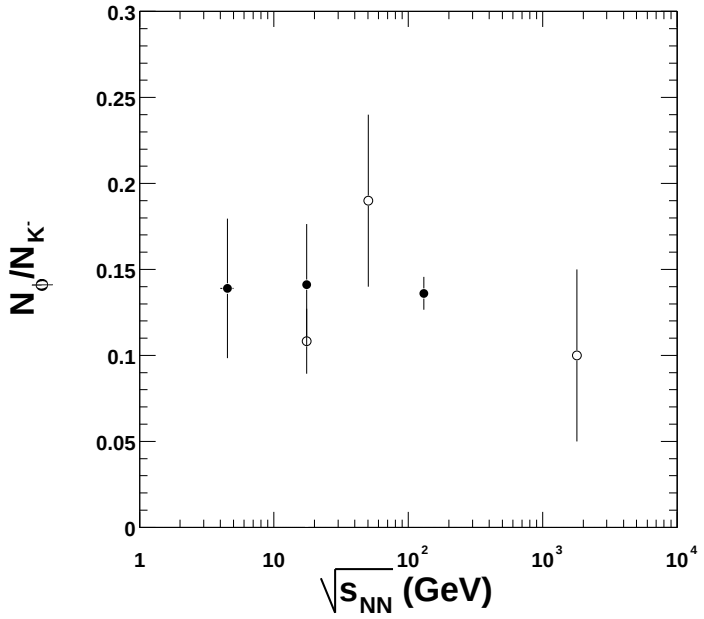

Figure 8.2: N_ϕ/N_{K^-} ratio vs. $\sqrt{s_{NN}}$ for approximately the 10% most central heavy ion collisions (filled circles) and $p+p$ collisions (open circles). Error bars shown are statistical errors only.

GeV/c. In addition, the anti-proton slope shows a clear dependence on event centrality [Har01] (Figure 8.4). Note that if a strong collective flow develops in the system, the measured slope parameter should depend strongly on the fitting range. From Equation 2.4, we would expect similar slope parameters for the $\bar{p}$ and ϕ meson since their masses are similar ($m_{\bar{p}} = 0.938$ GeV/c^2, $m_\phi = 1.019$ GeV/c^2). The ϕ, Λ and Ξ^- ($s\bar{s}, uds, dss$ quark content, respectively) slope parameters seem to be independent of their masses, with a mean value $\langle T \rangle = 352 \pm 4$ MeV. From these preliminary results, several possible implications arise:

- The cross sections for these particles are much smaller than that of the anti-proton, leading to fewer interaction in the final hadronic state.

- The ϕ, Λ and Ξ^- particles may freeze-out earlier at a higher system temperature. Coupled with their a-priori smaller cross-sections, these particles would retain a memory of their freeze-out epoch.

There has been much debate on whether Figure 8.3 is meaningful. At the heart of the debate is the effect of radial flow and the dependence of the measured slope parameter not only on the mass of a particle but also the kinematic range, p_t measured. The effect is to cause the slope parameter to depend on the measured p_t range. Results for the anti-proton slope parameter from PHENIX [Zaj01] and STAR [Har01] show a significant difference. PHENIX and STAR have different coverages in p_t for anti-protons due to the limitations on particle identification, with PHENIX measuring the kinematic region $\sim 0.5 < p_t < 3.5$ GeV/c while STAR measures the region $\sim 0.25 < p_t < 1.0$ GeV/c. While the spectra seem to overlap smoothly, PHENIX measures an appreciably smaller slope parameter than the STAR measurement (Figure 8.5). To account for the p_t dependence of radial flow, a hydrodynamically motivated fit was done to the STAR anti-proton and ϕ data by Kaneta and Xu [KX01]. In their fit, Kaneta and Xu uses the hydrodynamical model of Schnedermann *et al.* [Sch93]. This model is an application of the Cooper-Frye formula and the functional form of the fit is:

$$\frac{dN}{m_t dm_t} \propto \int_0^R r\, dr\, m_t K_1\left(\frac{m_t \cosh\rho}{T_{th}}\right) I_0\left(\frac{p_t \sinh\rho}{T_{th}}\right) \qquad (8.3)$$

$$\rho = \tanh^{-1}\beta_r$$

The Cooper-Frye formalism assumes a cylindrical boost-invariant source with a radius R_0, and requires an assumption on the collective velocity profile, β_r, as a function of the distance from the center of the cylinder. For their analysis, Kaneta and Xu used a linear radial velocity profile, $\beta_r = \beta_s(r/R)$, where β_s is the surface radial velocity.

The spectra are fit to extract a thermal freeze-out temperature, T_{th} and an average β_s. Equation 2.4 is an approximation to the Cooper-Frye formula, and is discussed by Bearden *et al.* [Bea97].

The result of the fit to the STAR data is shown in Figure 8.6. The plot is a χ^2 contour map as a function of T_{th} and β_s for the ϕ meson and anti-proton. The minima for the fits are denoted by the diamonds and the contours represent the χ^2 95% confidence level. It is clear that at about the 95% confidence level, there is a quantitative difference in the hydrodynamical properties of the ϕ and anti-proton. The anti-proton fit to the hydrodynamical model consistently yields a higher surface velocity and lower thermal temperature. Within this framework, these results indicate that the ϕ meson may stop interacting at an earlier stage and undergo fewer scatterings with nuclear matter than the anti-proton.

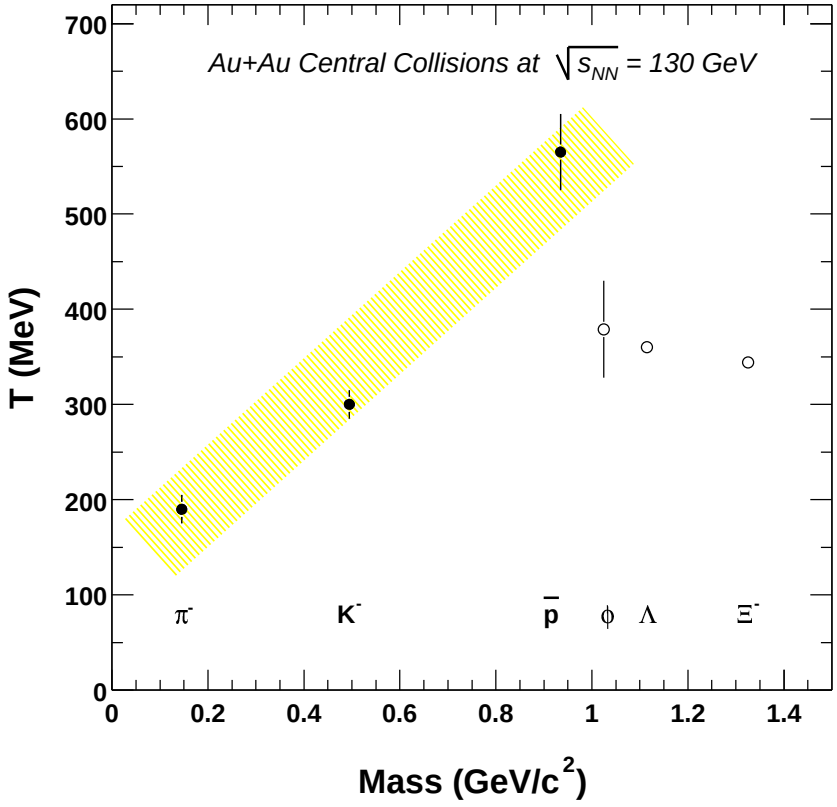

Figure 8.3: T vs. mass for particles measured in the most central events at STAR. The slope parameters for π^-, K^- and $\bar{p}$ follow an increasing linear trend with mass which is consistent with these particles interacting with a common radial velocity field. The ϕ, Λ and Ξ^- do not seem to follow this trend. Their measured slope parameters are similar. Error bars shown are statistical errors only.

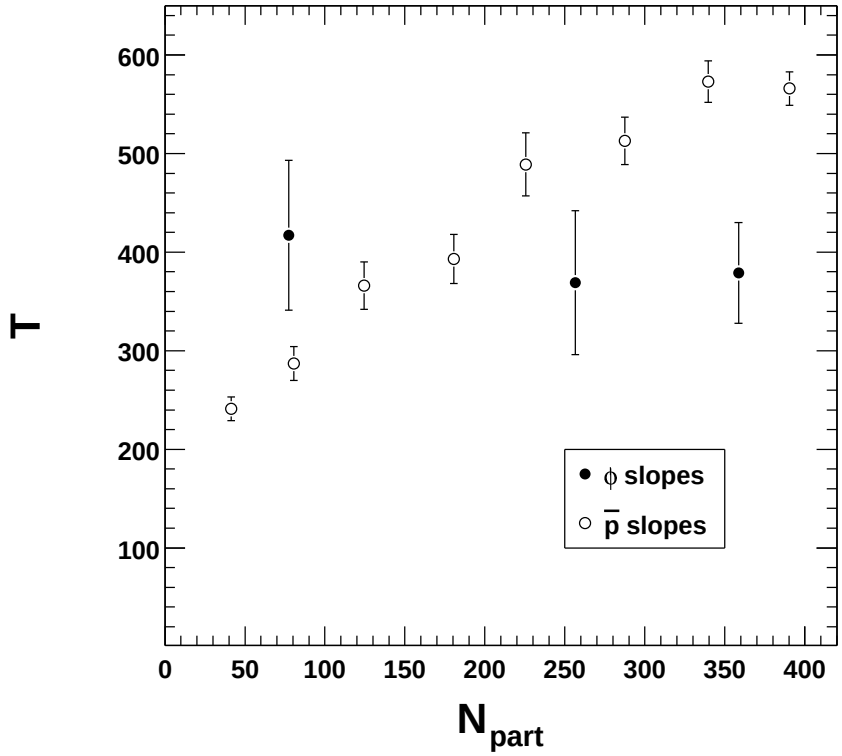

Figure 8.4: Slope parameters for the ϕ meson and anti-proton for various centrality bins. Error bars shown are statistical errors only.

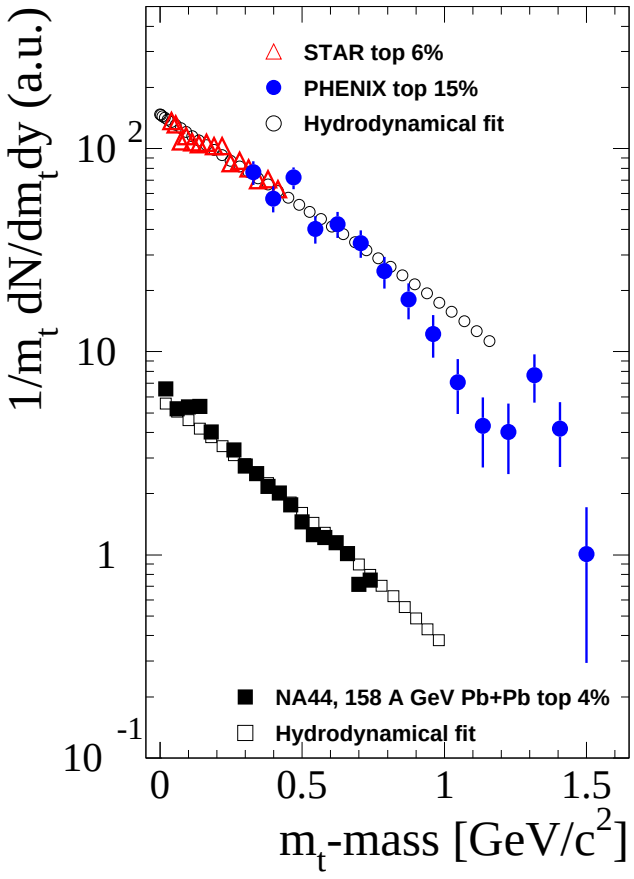

Figure 8.5: The preliminary transverse mass distributions for anti-protons from RHIC (STAR and PHENIX measurements) and SPS (NA44) measurement. The data were fit to a hydrodynamical model. A significant curvature is observed at RHIC, which is consistent with the effects of collective radial flow. Error bars shown are statistical errors only.

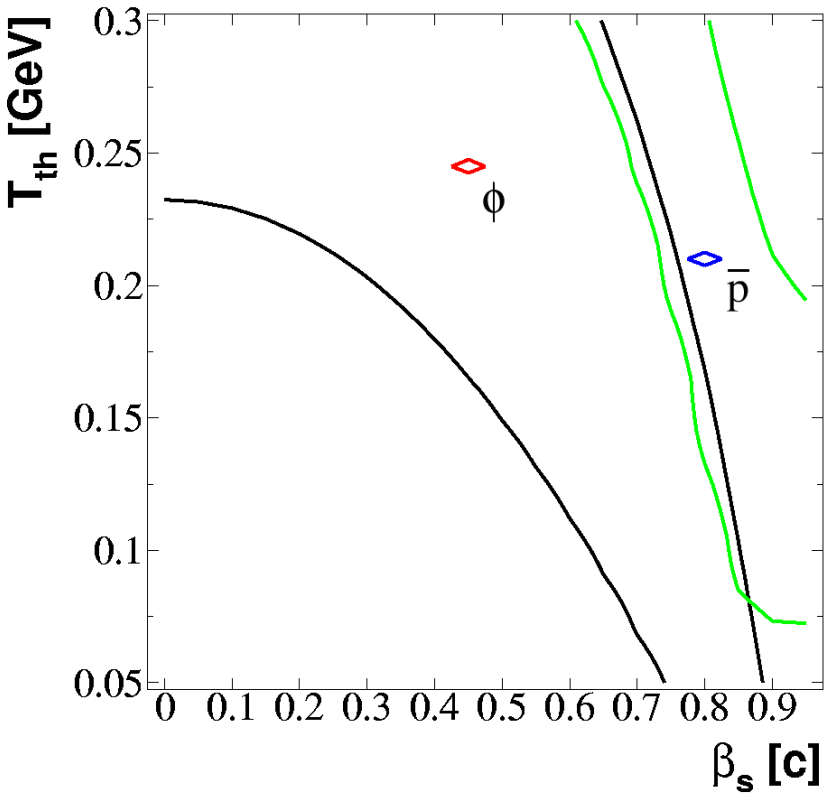

Figure 8.6: The χ^2 contour map of T_{th} and β_s for a hydrodynamical fit to the STAR ϕ and anti-proton data. The χ^2 minima are represented by the diamonds and the contours represent the χ^2 95% confidence level.

CHAPTER 9

Conclusion

Veni, vidi, video. An initial study of the production properties of ϕ mesons in $Au+Au$ collisions at $\sqrt{s_{NN}} = 130$ GeV has been completed. The centrality dependence of the mid-rapidity ϕ yield and transverse momentum distributions have been described. This represents the first results on vector meson production at RHIC.

9.1 Production Rates

Results from the first year of data from RHIC seem to indicate a significant increase in the production rate for ϕ mesons over previous heavy ion experiments at the AGS and SPS. This points to an overall increase in strangeness production. Possibly the most intriguing conclusion on ϕ meson production is the universality of the ϕ/K^- ratio. While the collision energy and system size may differ by several orders of magnitude, the ϕ/K^- ratio remains the same within the experimental uncertainties of the current World data from $\sqrt{s_{NN}} = 4.9$ to 1800 GeV. This may indeed be coincidence, but one would logically presume that this ratio would point to a production mechanism which is independent of the initial colliding system.

There seems to be little evidence to support the kaon coalescence model as the dominant production mechanism for the ϕ meson. It is unlikely that ϕ mesons are created mostly from equilibrated $s\bar{s}$ pairs in $p+p$ systems. This may be feasible in heavy

ion collisions, where the number density of strange and anti-strange quarks is large, but for a simple colliding system such as $p+p$, it would at the very least be a stretch of the imagination to assume this production mechanism dominates. Two possible mechanisms may be important: light quark fusion ($q\bar{q} \rightarrow \phi$, and gluon fusion $ggg \rightarrow \phi$), both of which are partonic models of production. This is somewhat surprising in light of the significant interest in the past few years of describing ϕ production by invoking the coalescence of final state kaons. The conclusion of "direct" (i.e. non-hadronic) production of the ϕ meson should be investigated further with the upcoming data from RHIC.

9.2 Dynamical Properties

It is not sufficient to characterize the m_t spectra of many particles with a simple exponential function with a slope parameter T, especially if the effects of hydrodynamical expansion of nuclear matter depends on the transverse momentum and mass of the particle. In spite of this, the controversial T vs. mass plot may still provide useful information.

In Section 8.2, the dynamical properties of the ϕ meson were shown to be quantitatively different from the anti-protons. The slope parameters for the ϕ and anti-proton as well as the hydrodynamical model fit to their spectra both indicate a quantitative difference albeit given the PHENIX anti-proton spectra, it is possible that the ϕ and anti-proton may have similar slope parameters in the high p_t region.

This still does not elucidate the discrepancy in the ϕ measurements at the CERN SPS. Two different experiments measuring two different decay channels for the ϕ observed vastly differing spectral shapes. NA49 measured a ϕ slope parameter from the K^+K^- channel similar to the proton and anti-proton. NA50 measured the ϕ slope pa-

rameter from the $\mu^+\mu^-$ decay channel and found that it differed significantly from the proton and anti-proton slopes. A superficial interpretation would assume one experiment was wrong: the conclusions drawn about the ϕ cross section for nuclear matter from either one of the experiments drastically differ. The NA49 results indicate that the ϕ meson cross section for nuclear matter is large and that the ϕ participates in radial flow. The NA50 results, however, indicate that the ϕ meson does not interact with nuclear matter and does not participate in radial flow. Johnson, Jacak and Drees [JJD01] and Soff *et al.* [Sof01] have attempted to explain the discrepancy between the two measurements as resulting from the re-scattering of the daughter kaons in the final hadronic state in the NA49 measurement. They can account for 10 to 20% of the discrepancy through the destruction of the kaon correlation due to final state scattering.

It is important that the same experiment perform measurements of the ϕ meson from both the hadronic channel (K^+K^-) and the leptonic channel ($\mu^+\mu^-$ or e^+e^-). While this was not the case at the CERN SPS, it will occur at PHENIX and possibly STAR. With complementary measurements, we may begin to understand the production properties of the ϕ meson.

9.3 Future Directions

There are a multitude of wish-list items that come to mind as I close this chapter in the ϕ analysis. I do not want to burden the reader (if there are any) with a compilation of my desultory thoughts: instead I will expound on a few.

First and foremost is the statistics available for this analysis. With the large acceptance of the STAR TPC, the acceptance for ϕ mesons was reasonable but the acceptance for background was also large. The ϕ signal sat on a huge combinatorial background which reduced the statistical significance of the measurement. There are two

methods of overcoming this limitation. The first would have been to take more data since the signal typically beats the background by a factor of $\sim \sqrt{N_{events}}$. This option was somewhat beyond the control of the STAR collaboration since it is the accelerator group which is ultimately responsible for delivering collisions to the experiments. The other would have been to have a more comprehensive particle identification system in place. The TPC does a fantastic job but one can always improve the situation by placing complementary detector systems in STAR. One example would be a barrel Time Of Flight (TOF) system. Not only would this system have reduced the pion background tremendously, but it would also have increased our p_t coverage since kaons and pions are easily identified up to at least 1 GeV/c in momentum.

Finer centrality binning will also be a future issue. The centrality dependence of ϕ slopes, yields, and ratios with other particles will provide useful information. A centrality dependence of the slopes, when compared to the centrality dependence of slope parameters for other particles, may give an indication of the relative cross sections for the various particle species as well as the magnitude of kaon re-scattering. A difference in the centrality dependence of the ϕ and K slopes will pose additional difficulties for the kaon coalescence model of ϕ production, since dynamical coalescence requires a correlation in space, time and momentum space. The ϕ/K ratios may give further insight into the production mechanism for the ϕ meson. The relative yield of the ϕ at future RHIC energies compared to previous measurements will provide a further indication for strangeness production.

Measurements of the ϕ meson in $p+p$, $p+A$ and light nucleus-nucleus (e.g. $C+C$, $S+S$) collisions will be critical to further understand the production mechanisms and dynamical properties of the ϕ, as well as establishing the conditions present when ϕ mesons were formed. The simple $p+p$ colliding system will establish a baseline for the production properties of the ϕ. We may then study the properties of the ϕ meson

at a fixed collision energy while varying the system size. The advantage of varying the system size over a centrality measurement is the ability to control the number of participants more accurately. The systematic study of ϕ production vs. system size may be more sensitive to dynamical fluctuations than a study of the centrality dependence in the heavy $Au+Au$ system. Perhaps the ϕ meson will be sensitive to dynamical fluctuations in strange quark production.

Possibly the most innovative measurement will be to measure the elliptic flow (v_2) of the ϕ meson. The elliptic flow measurement is sensitive to the anisotropic emission of particles in momentum space, which is induced by an initial asymmetry in position space. This asymmetry occurs because of the finite size of the colliding nuclei; if the collision is off-center, the overlapping region of the two colliding nuclei is no longer circular but more elliptical. A conclusion that the ϕ meson has a smaller cross section than the proton would mean that the measured anisotropy in the emission of ϕ mesons may be representative of the anisotropy of the system at the moment of thermal freeze-out of the ϕ, which, from Figure 8.6, is presumably earlier and at a higher system temperature. Perhaps the ϕ cross section may be described within Weinberg's classical analysis of soft pion-nucleon cross sections [Per86]. In this framework, the ϕ, with an iso-spin zero, would have a small cross section with nuclear media. We may then infer that the moment that an $s\bar{s}$ hadronizes into the ϕ also corresponds to its thermal freeze-out. If ϕ production is dominated by the partonic production modes, we may hope that the ϕ meson carries information regarding the partonic state that it emerged from. It is most likely that people may deride this naïve proposition of a small ϕ cross section and the possible implications I draw. As a defense, I point to the plethora of models currently available.

Our understanding of heavy ion collisions is far from complete. The search for the Quark-Gluon Plasma continues. Perhaps we may never dis-entangle the various

processes involved in heavy ion collisions. While it is utterly unreasonable to even attempt to claim an understanding of the first year of RHIC data and its implications for the QGP search, it was apparent at Quark Matter 2001 that the community has established a foothold in understanding the basic properties of $Au+Au$ collisions at $\sqrt{s_{NN}} = 130$ GeV. Ralph Waldo Emerson once said:

All life is an experiment.
The more experiments you make the better.

With results from preceding experimental efforts, this prologue from RHIC and future measurements from both RHIC and LHC, we may some day come to a definitive picture for nucleus-nucleus collisions in our search for the Quark-Gluon Plasma.

APPENDIX A

Relativistic Kinematics

In this appendix, aspects of relativistic kinematics relevant to heavy ion physics and resonance analysis are reviewed. The purpose of this appendix is to provide an introduction for the reader who is new to heavy ion physics, and to set forth the notation and convention used in this thesis. The following derivations use the convention in which $\hbar = c = 1$. The following conversions are useful: $\hbar c = 197.3$ MeV fm and $(\hbar c)^2 = 0.3894\ (\mathrm{GeV})^2$ mb.

A.1 Lorentz Transformations

The energy E and 3-momentum $\mathbf{p}$ of a particle of mass m form the 4-vector $p = (E,\mathbf{p})$, whose square $p^2 \equiv E^2 - |\mathbf{p}|^2 = m^2$. The velocity of the particle is $\beta = \mathbf{p}/E$. The energy and momentum $(E^*,\mathbf{p}^*)$ viewed from a frame moving with a velocity β_f are given by

$$\begin{pmatrix} E^* \\ p^*_{||} \end{pmatrix} = \begin{pmatrix} \gamma_f & -\gamma_f\beta_f \\ -\gamma_f\beta_f & \gamma_f \end{pmatrix} \begin{pmatrix} E \\ p_{||} \end{pmatrix}, \; p^*_t = p_t \tag{A.1}$$

where $\gamma_f = 1/\sqrt{1-\beta_f^2}$ and $p_t(p_{||})$ are the components of $\mathbf{p}$ perpendicular (parallel) to β_f. Other 4-vectors, such as the space-time coordinates of events transform in the same manner. The scalar product of two 4-momenta $p_1 \cdot p_2 = E_1E_2 - \mathbf{p}_1 \cdot \mathbf{p}_2$ is invariant (frame independent).

A.2 Kinematic Variables

We consider collision systems with two bodies (particles or nuclei) in the initial state and define the z-axis to coincide with the axis of collision. For the purposes of presenting single-particle differential multiplicities (see Section B, it is convenient to describe particle trajectories using kinematic variables which are either Lorentz invariant or transform trivially under Lorentz boosts along this axis.

The momentum components p_x and p_y are unchanged by a boost along z so we define and use the transverse momentum of a particle,

$$p_t \equiv \sqrt{p_x^2 + p_y^2} \tag{A.2}$$

as one such variable. The transverse mass (or transverse energy) of a particle with mass m is defined as

$$m_t \equiv \sqrt{p_t^2 + m^2} \tag{A.3}$$

such that the transverse kinetic energy of the particle is $m_t - m$.

The longitudinal variable most commonly used is rapidity,

$$y \equiv \frac{1}{2} \ln \left(\frac{E + p_z}{E - p_z} \right) \tag{A.4}$$

which has the advantage of being additive under Lorentz transformations along z. This means that under Lorentz transformations along z, differences in rapidity, dy, are invariant and rapidity spectra, dN/dy, translate in y while their shapes are preserved. The expression for rapidity may also be written as

$$y = \ln \left(\frac{E + p_z}{m_t} \right). \tag{A.5}$$

From the above definitions, the relations

$$p_z = m_t \sinh y \tag{A.6}$$

$$E = m_t \cosh y \tag{A.7}$$

are obtained. Dividing these, we have

$$\beta_z = \tanh y \tag{A.8}$$

which is the longitudinal component of the velocity of a particle of rapidity y in the lab. Since rapidity is additive under Lorentz transformations, this suggests a form for the rapidity transformation corresponding to a boost along the z-axis. If a particle has a rapidity y in the lab and we want to know its rapidity y' in a system which has velocity β_z relative to the lab, then:

$$y' = y - \tanh^{-1} \beta_z. \tag{A.9}$$

A related quantity is the pseudo-rapidity, η. To obtain the expression for η, we first rewrite Equation A.4 as

$$y = \frac{1}{2} \ln \left(\frac{1+\beta \cos\theta}{1-\beta \cos\theta} \right) \tag{A.10}$$

and taking the limit of Equation A.10 as $\beta \to 1$:

$$\eta \equiv -\ln \tan \left(\frac{\theta}{2} \right). \tag{A.11}$$

For particles with $\beta \approx 1$, $\eta \approx y$, while for massless particles, $\eta = y$. Note that a particle's η only depends on its angle of emission relative to the beam axis.

APPENDIX B

Single Particle Phase Space and Invariant Yields

The purpose of this section is to come up with a form for differential cross sections and yields that are Lorentz invariant. When we speak of differential yields, we refer to the number of particles emitted into a particular region in momentum space per interaction. It is natural to assume at first that we refer to an object such as d^3N/dp^3. The total yield of a particular particle is the total number of such particles emitted into any point in momentum space per interaction,

$$N = \int \frac{d^3N}{dp^3} d^3p \tag{B.1}$$

which intuitively must be Lorentz invariant. The momentum-space volume element, d^3p, however, is not invariant since the differential momentum element along the direction of a boost between frames transforms as $dp' = \gamma dp$. If we choose to report differential yields in the form d^3N/dp^3, we have to be careful to state the frame in which they were measured. In order to compare the results from different experiments, we would have to explicitly transform the differential yields.

We can avoid such complexities if we find an expression for the differential yield which is manifestly invariant. Effectively this mean adopting a Lorentz invariant definition of a momentum-space bin. The momentum-space volume element d^4p is invariant ($dE' = dE/\gamma$), but the set d^4p includes momentum-space bins in which particles

are off-shell. Requiring particles to be on-shell, we obtain:

$$\int \delta(p \cdot p - m^2) d^4p = \int \delta(E^2 - \mathrm{p}^2 - m^2) d^3p \, dE = \frac{d^3p}{2E}. \tag{B.2}$$

The left hand side of this expression is invariant (the delta function is invariant since its argument is), and we have used $\delta(f(x)) = \sum_i \delta(x - x_i)/|f'(x)|$, where the x_i are the zeros of $f(x)$. We see that the momentum-space volume element d^3p/E is Lorentz invariant.

The quantum mechanical density of states is obtained by solving the particle-in-a-box problem in the non-relativistic formulation. The number of states in a momentum bin d^3p is:

$$d^3n = \frac{V}{(2\pi)^3} d^3p \tag{B.3}$$

where V is the volume of the box. This is not a Lorentz invariant quantity. In fact, in relativistic quantum mechanics, a state normalization of the sort $\int_V \psi^* \psi = 1$ can be problematic, since V is not Lorentz invariant either. In the end, the only thing that matters is that the observable quantities, as calculated by the Golden Rule

$$\text{transition rate} = 2\pi |M|^2 \times \text{ phase space} \tag{B.4}$$

evaluate correctly without reference to the conventions used to define phase space or the squared matrix element, $|M|^2$. If a covariant normalization for states such as $\int \psi^* \psi = 2E/V$ is adopted (to be interpreted as $2E$ particles in the normalization volume V), then the corresponding expression for single-particle phase space to be used with the Golden Rule is:

$$dF = \frac{V d^3p}{(2\pi)^3 (2E)} \tag{B.5}$$

which is very similar to Equation B.2 but the density of states in an absolute sense is

not given by this expression; it is given by Equation B.3.

In any event, the momentum-space volume element d^3p/E is invariant. Therefore, so are the differential yield, Ed^3N/dp^3, and the total yield

$$N = \int E \frac{d^3N}{dp^3} \frac{d^3p}{E}. \tag{B.6}$$

We can write the momentum-space volume element using any variables we like (Section A.2) using the Jacobian of the transformation between (p_x, p_y, p_z) and (ϕ, p_t, y). The result is:

$$\frac{dp_x dp_y dp_z}{E} = p_t \, dp_t \, dy \, d\phi. \tag{B.7}$$

The expression for total yield is then

$$N = \int \frac{d^3N}{p_t \, dp_t \, dy \, d\phi} p_t \, dp_t \, dy \, d\phi. \tag{B.8}$$

Finally, in many analyses in heavy ion physics, the reaction plane is not measured and the azimuthal distribution can be assumed to be isotropic. The integral in ϕ can thus be performed immediately. If, however, we want to use a form equivalent to Ed^3N/dp^3 for the presentation of different yields, we need to quote the average rather than the sum over ϕ. The expression for total yield becomes:

$$N = \int \frac{d^3N}{2\pi p_t \, dp_t \, dy} 2\pi p_t \, dp_t \, dy. \tag{B.9}$$

We further observe that $p_t \, dp_t = m_t \, dm_t$, so that Equation B.9, with m_t in place of p_t, is an equally valid form for the invariant yield.

The integrand of Equation B.9 is Lorentz invariant for boosts along the collision axis since N is dimensionless and p_t, dp_t, and dy are invariant for such boosts. With y and p_t defined relative to the boost axis, the expression is invariant for boosts in any

direction.

APPENDIX C

The STAR Collaboration

STAR Collaboration Author List

C. Adler[11], Z. Ahammed[23], C. Allgower[12], J. Amonett[14], B.D. Anderson[14], M. Anderson[5], G.S. Averichev[9], J. Balewski[12], O. Barannikova[9,23], L.S. Barnby[14], J. Baudot[13], S. Bekele[20], V.V. Belaga[9], R. Bellwied[30], J. Berger[11], H. Bichsel[29], L.C. Bland[12], C.O. Blyth[3], B.E. Bonner[24], R. Bossingham[15], A. Boucham[26], A. Brandin[18], R.V. Cadman[1], H. Caines[20], M. Calderón de la Barca Sánchez[31], A. Cardenas[23], J. Carroll[15], J. Castillo[26], M. Castro[30], D. Cebra[5], S. Chattopadhyay[30], M.L. Chen[2], Y. Chen[6], S.P. Chernenko[9], M. Cherney[8], A. Chikanian[31], B. Choi[27], W. Christie[2], J.P. Coffin[13], L. Conin[26], T.M. Cormier[30], J.G. Cramer[29], H.J. Crawford[4], M. DeMello[24], W.S. Deng[14], A.A. Derevschikov[22], L. Didenko[2], J.E. Draper[5], V.B. Dunin[9], J.C. Dunlop[31], V. Eckardt[16], L.G. Efimov[9], V. Emelianov[18], J. Engelage[4], G. Eppley[24], B. Erazmus[26], P. Fachini[25], V. Faine[2], E. Finch[31], Y. Fisyak[2], D. Flierl[11], K.J. Foley[2], J. Fu[15], N. Gagunashvili[9], J. Gans[31], L. Gaudichet[26], M. Germain[13], F. Geurts[24], V. Ghazikhanian[6], J. Grabski[28], O. Grachov[30], D. Greiner[15], V. Grigoriev[18], M. Guedon[13], E. Gushin[18], T.J. Hallman[2], D. Hardtke[15], J.W. Harris[31], M. Heffner[5], S. Heppelmann[21], T. Herston[23], B. Hippolyte[13], A. Hirsch[23], E. Hjort[15], G.W. Hoffmann[27], M. Horsley[31], H.Z. Huang[6], T.J. Humanic[20], H. Hümmler[16], G. Igo[6], A. Ishihara[27], Yu.I. Ivanshin[10], P. Jacobs[15], W.W. Jacobs[12], M. Janik[28], I. Johnson[15], P.G. Jones[3], E. Judd[4], M. Kaneta[15], M. Kaplan[7], D. Keane[14], A. Kisiel[28], J. Klay[5], S.R. Klein[15], A. Klyachko[12], A.S. Konstantinov[22], L. Kotchenda[18], A.D. Kovalenko[9], M. Kramer[19], P. Kravtsov[18], K. Krueger[1], C. Kuhn[13], A.I. Kulikov[9], G.J. Kunde[31], C.L. Kunz[7], R.Kh. Kutuev[10], A.A. Kuznetsov[9], L. Lakehal-Ayat[26], J. Lamas-Valverde[24], M.A.C. Lamont[3], J.M. Landgraf[2], S. Lange[11], C.P. Lansdell[27], B. Lasiuk[31], F. Laue[2], A. Lebedev[2], T. LeCompte[1], R. Lednický[9], V.M. Leontiev[22], M.J. LeVine[2], Q. Li[30], Q. Li[15], S.J. Lindenbaum[19], M.A. Lisa[20], T. Ljubicic[2], W.J. Llope[24], G. LoCurto[16], H. Long[6], R.S. Longacre[2], M. Lopez-Noriega[20], W.A. Love[2], D. Lynn[2], R. Majka[31], S. Margetis[14], L. Martin[26], J. Marx[15], H.S. Matis[15], Yu.A. Matulenko[22], T.S. McShane[8], F. Meissner[15], Yu. Melnick[22], A. Meschanin[22], M. Messer[2], M.L. Miller[31], Z. Milosevich[7], N.G. Minaev[22], J. Mitchell[24], V.A. Moiseenko[10], D. Moltz[15], C.F. Moore[27], V. Morozov[15], M.M. de Moura[30], M.G. Munhoz[25], G.S. Mutchler[24], J.M. Nelson[3], P. Nevski[2], V.A. Nikitin[10], L.V. Nogach[22], B. Norman[14], S.B. Nurushev[22], G. Odyniec[15], A. Ogawa[21], V. Okorokov[18], M. Oldenburg[16], D. Olson[15], G. Paic[20], S.U. Pandey[30], Y. Panebratsev[9], S.Y. Panitkin[2], A.I. Pavlinov[30],

T. Pawlak[28], V. Perevoztchikov[2], W. Peryt[28], V.A Petrov[10], W. Pinganaud[26], E. Platner[24], J. Pluta[28], N. Porile[23], J. Porter[2], A.M. Poskanzer[15], E. Potrebenikova[9], D. Prindle[29], C. Pruneau[30], S. Radomski[28], G. Rai[15], O. Ravel[26], R.L. Ray[27], S.V. Razin[9,12], D. Reichhold[8], J.G. Reid[29], F. Retiere[15], A. Ridiger[18], H.G. Ritter[15], J.B. Roberts[24], O.V. Rogachevski[9], J.L. Romero[5], C. Roy[26], D. Russ[7], V. Rykov[30], I. Sakrejda[15], J. Sandweiss[31], A.C. Saulys[2], I. Savin[10], J. Schambach[27], R.P. Scharenberg[23], K. Schweda[15], N. Schmitz[16], L.S. Schroeder[15], A. Schüttauf[16], J. Seger[8], D. Seliverstov[18], P. Seyboth[16], E. Shahaliev[9], K.E. Shestermanov[22], S.S. Shimanskii[9], V.S. Shvetcov[10], G. Skoro[9], N. Smirnov[31], R. Snellings[15], J. Sowinski[12], H.M. Spinka[1], B. Srivastava[23], E.J. Stephenson[12], R. Stock[11], A. Stolpovsky[30], M. Strikhanov[18], B. Stringfellow[23], H. Stroebele[11], C. Struck[11], A.A.P. Suaide[30], E. Sugarbaker[20], C. Suire[13], M. Šumbera[9], T.J.M. Symons[15], A. Szanto de Toledo[25], P. Szarwas[28], J. Takahashi[25], A.H. Tang[14], J.H. Thomas[15], V. Tikhomirov[18], T.A. Trainor[29], S. Trentalange[6], M. Tokarev[9], M.B. Tonjes[17], V. Trofimov[18], O. Tsai[6], K. Turner[2], T. Ullrich[2], D.G. Underwood[1], G. Van Buren[2], A.M. VanderMolen[17], A. Vanyashin[15], I.M. Vasilevski[10], A.N. Vasiliev[22], S.E. Vigdor[12], S.A. Voloshin[30], F. Wang[23], H. Ward[27], J.W. Watson[14], R. Wells[20], T. Wenaus[2], G.D. Westfall[17], C. Whitten Jr. [6], H. Wieman[15], R. Willson[20], S.W. Wissink[12], R. Witt[14], N. Xu[15], Z. Xu[31], A.E. Yakutin[22], E. Yamamoto[6], J. Yang[6], P. Yepes[24], A. Yokosawa[1], V.I. Yurevich[9], Y.V. Zanevski[9], I. Zborovský[9], W.M. Zhang[14], R. Zoulkarneev[10], A.N. Zubarev[9]

(STAR Collaboration)

[1]Argonne National Laboratory, Argonne, Illinois 60439
[2]Brookhaven National Laboratory, Upton, New York 11973
[3]University of Birmingham, Birmingham, United Kingdom
[4]University of California, Berkeley, California 94720
[5]University of California, Davis, California 95616
[6]University of California, Los Angeles, California 90095
[7]Carnegie Mellon University, Pittsburgh, Pennsylvania 15213
[8]Creighton University, Omaha, Nebraska 68178
[9]Laboratory for High Energy (JINR), Dubna, Russia
[10]Particle Physics Laboratory (JINR), Dubna, Russia
[11]University of Frankfurt, Frankfurt, Germany
[12]Indiana University, Bloomington, Indiana 47408
[13]Institut de Recherches Subatomiques, Strasbourg, France
[14]Kent State University, Kent, Ohio 44242
[15]Lawrence Berkeley National Laboratory, Berkeley, California 94720
[16]Max-Planck-Institut fuer Physik, Munich, Germany
[17]Michigan State University, East Lansing, Michigan 48824
[18]Moscow Engineering Physics Institute, Moscow, Russia
[19]City College of New York, New York City, New York 10031
[20]Ohio State University, Columbus, Ohio 43210
[21]Pennsylvania State University, University Park, Pennsylvania 16802
[22]Institute of High Energy Physics, Protvino, Russia

[23]Purdue University, West Lafayette, Indiana 47907
[24]Rice University, Houston, Texas 77251
[25]Universidade de Sao Paulo, Sao Paulo, Brazil
[26]SUBATECH, Nantes, France
[27]University of Texas, Austin, Texas 78712
[28]Warsaw University of Technology, Warsaw, Poland
[29]University of Washington, Seattle, Washington 98195
[30]Wayne State University, Detroit, Michigan 48201
[31]Yale University, New Haven, Connecticut 06520

REFERENCES

[Abb90] T. Abbot et al. *Phys. Rev. Lett.*, **64**:847, 1990.

[Ack99] K.H. Ackermann et al. "The STAR Time Projection Chamber." *Nucl. Phys.*, **A661**:681c – 685c, 1999.

[Ack01] K.H. Ackermann et al. *Phys. Rev. Lett.*, **86**:402, 2001.

[Adl01a] C. Adler et al. *Phys. Rev. Lett.*, **86**:4778, 2001.

[Adl01b] C. Adler et al. "Multiplicity distribution and spectra of negatively charged hadrons in Au+Au collisions at $\sqrt{s_{NN}} = 130$ GeV." *Submitted to Phys. Rev. Lett.*, 2001.

[Afa00] S.V. Afanasiev et al. *Phys. Lett.*, **B491**:59, 2000.

[Ahl98] L. Ahle et al. *Phys. Rev.*, **C58**:3523, 1998.

[Ahl99] L. Ahle et al. *Phys. Rev.*, **C60**, 1999.

[Ahm96] S. Ahmad et al. *Phys. Lett.*, **B382**:35, 1996.

[Alb94] T. Alber et al. *Z. Phys.*, **C64**:195, 1994.

[Ale93] T. Alexopoulos et al. *Phys. Rev.*, **D48**:984, 1993.

[Ale95] T. Alexopoulos et al. *Z. Phys.*, **C67**:411, 1995.

[And99] E. Andersen et al. *Phys. Lett.*, **B449**:401, 1999.

[Ant99] F. Antinori et al. *Phys. Lett.*, **B447**:178, 1999.

[Bac00] B. Back et al. "E917 results on strangeness production in Au+Au collisions at AGS." In *Proceedings of the Thirtieth International Conference on High Energy Physics*. World Scientific, 2000.

[BD96] A.J. Baltz and C. Dover. *Phys. Rev.*, **C53**:362, 1996.

[Bea97] I. Bearden et al. *Phys. Rev. Lett.*, **78**:2080, 1997.

[BGS98] S.A. Bass, M. Gyulassy, H. Stöcker, and W. Greiner. "Signatures of Quark-Gluon-Plasma formation in high energy heavy-ion collisions: A critical review." *hep-ph/9810281*, 1998.

[Bor97] C. Bormann et al. *J. Phys.*, **G23**:1817, 1997.

[BR94] W. Blum and L. Rolandi. *Particle Detection With Drift Chambers*. Springer Verlag, Berlin, second edition, 1994.

[BR97] Rene Brun and Fons Rademakers. "ROOT - An Object Oriented Data Analysis Framework." *Nucl. Inst. and Meth. in Phys. Res.*, **A389**:81–86, 1997.

[BSG94] M. Berenguer, H. Sorge, and W. Greiner. "ϕ meson production in ultra-relativistic heavy ion collisions." *Phys. Lett.*, **B332**:15–19, 1994.

[Cal00] M. Calderon. "Measurement of dE/dx resolution from the STAR TPC." *Private Communication*, 2000.

[Che00] I. Chemakin et al. *nucl-ex/0003010*, 2000.

[Col95] B. Cole et al. *Nucl. Phys.*, **A590**:179c, 1995.

[CX01a] M. Calderon and Z. Xu. "N_{ch} to h^- conversion." *Private Communication*, 2001.

[CX01b] Y. Chen and Z. Xu. "h^- to N_{part} conversion." *Private Communication*, 2001.

[DFN84] D. Drijard, H.G. Fischer, and T. Nakada. *Nucl. Instrum. Meth.*, **A225**:367, 1984.

[Die56] W. Diethorn. "A methane proportional counter system for natural radiocarbon measurements." *USAEC Report*, 1956.

[Div99] Information Technology Division. "PAW, Physics Analysis Workstation, User's guide." *CERN Program Library entry **Q121***, 1999. URL: http://wwwinfo.cern.ch/asdoc/psdir/paw.ps.gz.

[GG00] (Particle Data Group), D.E. Groom, et al. *Eur. Phys. Journal.*, **C15**:1, 2000.

[Gha98] V. Ghazikhanian. "Development of the STAR Gating Grid Driver System." *Private Communication*, 1998.

[Har01] J. Harris et al. "Results from the STAR Experiment." In *Quark Matter 2001: 15th International Conference on Ultra-Relativistic Nucleus-Nucleus Collisions*, 2001.

[Hei96] U. Heinz. *Nucl. Phys.*, **A610**:264c, 1996.

[HK94] T. Hatsuda and T. Kunihiro. *Phys. Rep.*, **247**:221, 1994.

[HSX98] H. van Hecke, H. Sorge, and N. Xu. *Phys. Rev. Lett.*, **81**:5674, 1998.

[Iiz66] J. Iizuka. *Prog. Theor. Phys.*, **35**:1061, 1966.

[JJD01] S. Johnson, B. Jacak, and A. Drees. *Eur. Phys. J.*, **C18**:645, 2001.

[KMR86] P. Koch, B. Müller, and J. Rafelski. *Phys. Rep.*, **142**:167, 1986.

[Kop74] G.I. Kopylov. *Phys. Lett.*, **B50**:472, 1974.

[KX01] M. Kaneta and N. Xu. "Hydrodynamical fits to RHIC data." *Private Communication*, 2001.

[LH94] D. L'Hote. *Nucl. Instrum. Meth.*, **A337**:544, 1994.

[Lie99] R. Lietava et al. *J. Phys.*, **G25**:181, 1999.

[LS91] D. Lissauer and E.V. Shuryak. *Phys. Lett.*, **B253**:15, 1991.

[LWT00] H. Long, H. Wieman, J.H. Thomas, and S. Trentalange. *Private Communication*, 2000.

[Mar99] S. Margetis et al. *J. Phys.*, **G25**:189, 1999.

[Mou01] M. Moulson. *Production of the ϕ meson in Si Au collisions at the BNL AGS*. Ph.D. Thesis, Columbia University, 2001.

[Oku63] S. Okubo. *Phys. Rev. Lett.*, **5**:165, 1963.

[Pan99] Sanjeev Pandey et al. "The STAR Silicon Drift Vertex Detector." *Nucl. Phys.*, **A661**:686c – 689c, 1999.

[Per86] D.H. Perkins. *Introduction to High Energy Physics*. Addison Wesley, Massachusetts, USA, third edition, 1986.

[Pro94] RHIC Project. "RHIC Design Manual." Technical report, Brookhaven National Laboratories, 1994. URL: http://www.agsrhichome.bnl.gov/NT-share/rhicdm/.

[PS95] M. Peskin and D. Schroeder. *Introduction to Quantum Field Theory*. Addision Wesley, Reading, Massachusets, fourth edition, 1995.

[Raf82] J. Rafelski. *Phys. Rep.*, **88**:331, 1982.

[Sch93] E. Schnedermann et al. *Phys. Rev.*, **C48**:2462, 1993.

[Sho85] A. Shor. *Phys. Rev. Lett.*, **54**:1122, 1985.

[Sof01] S. Soff et al. *J. Phys. G.: Nucl. Part.*, **27**:449c, 2001.

[Sor92] H. Sorge et al. “Color rope formation and strange baryon production in ultra-relativistic heavy ion collisions.” *Phys. Lett.*, **B289**:6, 1992.

[Tan01] A. Tang. “Measurement of dE/dx resolution from the STAR TPC.” *Private Communication*, 2001.

[Wan94] Y. Wang et al. *Nucl. Phys.*, **A566**:379c, 1994.

[Wie00] H. Wieman. *Private Communication*, 2000.

[Wil99] N. Willis et al. *Nucl. Phys.*, **A661**:534, 1999.

[Wil00a] F. Wilczek. *Physics Today*, **53**:22, August 2000.

[Wil00b] F. Wilczek. “QCD In Extreme Conditions.” *hep-ph/0003183*, 2000.

[Zaj84] W.A. Zajc et al. *Phys. Rev.*, **C29**:2173, 1984.

[Zaj01] W.A. Zajc et al. “Overview of PHENIX Results from the First RHIC Run.” In *Quark Matter 2001: 15th International Conference on Ultra-Relativistic Nucleus-Nucleus Collisions*, 2001.